Ultra-high vacuum fabrication of nanoscale systems for studying single-electron charging by room-temperature atomic force microscopy

Antoni A. Tekiel
Department of Physics
McGill University, Montreal
April 2013

A thesis submitted to McGill University in partial fulfillment
of the requirements of the degree of Doctor of Philosophy

Abstract

In this work we describe ultra-high vacuum fabrication of a nanoscale system that reveals Coulomb blockade at room temperature and its characterization by single-electron sensitive electrostatic force microscopy (*e*-EFM). The system consists of Au nanoparticles separated from an Fe(001) back electrode by a crystalline ultra-thin NaCl film. Due to the small size of the nanoparticles (3.5 nm high), the Coulomb blockade can be observed at room temperature. An atomic force microscopy (AFM) cantilever is used as a movable gate to charge individual nanoparticles via single-electron tunneling from the back electrode. At the same time the tunneling is detected by measuring frequency shift and damping of the oscillating cantilever. The *e*-EFM technique can overcome limitations of other characterization methods based on lithographic fabrication. So far, however, it has been successfully used only at low-temperatures. In this work, we extend the *e*-EFM technique to room temperature by carefully tuning the sample design and fabrication relative to the cantilever response to achieve maximum sensitivity.

To grow atomically defined tunnel barriers we investigate the morphology of MgO and NaCl ultra-thin films on Fe(001) surfaces by non-contact-AFM and low energy electron diffraction (LEED). First, we demonstrate that the quality of MgO films, typically grown in ultra-high vacuum (UHV) by electron-beam evaporation, can be improved by using reactive deposition method that gives full control over the gaseous species existing in the evaporated beam. Second, we investigate the effects of temperature and oxygen presence on the growth of NaCl on Fe(001). As a result, we develop a protocol to grow NaCl films on the Fe(001)-p(1×1)O surface in a layer-by-layer mode, yielding atomically flat films with 40-60 nm wide terraces (on a 12 ML thick film) and with far fewer defects than the MgO films.

Using the NaCl film as a tunnel barrier that can be easily adjusted by modifying the film thickness we characterize single-electron charging at room temperature of individual Au nanoparticles formed after thermal evaporation onto a 6

monolayer thick NaCl film. We demonstrate how a combination of *e*-EFM and finite element electrostatic simulation can be used for revealing electronic and morphological properties of individual Au nanoparticles. As a result, the electron addition energy, the capacitance, tunneling rates and an approximated shape of an individual nanoparticle have been determined. Numerical simulations point towards a total capacitance dominated by the mutual capacitance between the nanoparticle and the back electrode. A comparison with the experimental value, determined from measurement of the addition energy, indicates that the nanoparticles should be modeled as truncated spheres in order to reduce the mutual capacitance to the substrate. This observation has a fundamental impact on the design of nanoelectronic circuits, where the components have to meet desired requirements for capacitances that determine coupling and charging effects.

The fabrication flexibility and the fact that all measurements were performed *in-situ* on samples prepared under ultra-clean conditions make the presented system attractive for further studies. In particular, this approach can be used to study quantum mechanically coupled quantum dots and the catalytic activity of Au nanoclusters at room temperature.

Résumé

Dans ce travail, nous décrivons la fabrication sous ultra haut vide (UHV) d'un système à l'échelle nanométrique qui révèle le blocage de Coulomb à température de la pièce, ainsi que sa caractérisation par microscopie à force électrostatique sensible à un électron (single-electron sensitive electrostatic force microscopy, *e*-EFM). Le système est constitué de nanoparticules d'or séparées d'une électrode de Fe(001) par un film cristallin ultra mince de NaCl. Dû à la petite taille des nanoparticules (3.5 nm maximum), le blocage de Coulomb est observable à température ambiante. Un *cantilever* de microscope à force atomique (MFA) est utilisé comme une grille électrique déplaçable pour charger individuellement les nanoparticules par le passage de charge élémentaire par effet tunnel à partir de l'électrode. Ce passage d'électron est détecté en mesurant simultanément le changement de fréquence de résonance, ainsi que l'amortissement de l'oscillation du *cantilever*. La technique *e*-EFM permet de contourner certaines limitations inhérentes aux techniques de caractérisation basées sur la fabrication par lithographie. Toutefois, cette technique a été appliquée avec succès seulement à basses températures. Dans ce travail, nous étendons la technique *e*-EFM à température ambiante par un ajustement minutieux du design de l'échantillon et de sa fabrication en fonction de la réponse du *cantilever* de sorte à maximiser la sensibilité de la mesure.

Pour croître une jonction tunnel définie à l'échelle atomique, nous étudions la morphologie de couches minces de MgO et de NaCl sur une surface de Fe(001) par microscopie à force atomique non-contact et par diffraction d'électrons lents (Low Energy Electron Diffraction, LEED). Premièrement, nous démontrons que la qualité des couches minces de MgO, typiquement crûes sous UHV par évaporation sous faisceau d'électrons (electron-beam evaporation), peut être améliorée par l'utilisation d'une méthode de déposition réactive qui donne un contrôle total sur les espèces gazeuses présentes dans le faisceau d'évaporation. Deuxièmement, nous étudions l'effet de la température et de la présence d'oxygène sur la croissance du NaCl sur une surface de Fe(001). Conséquemment, un protocole pour la

croissance de films de NaCl sur une surface de Fe(001)-p(1×1)O déposés couche par couche. Ces films plats à l'échelle atomique présentent des terrasses de 40-60 nm de large et contiennent beaucoup moins de défauts cristallins que les films de MgO.

En utilisant ces couches minces de NaCl comme jonction tunnel facilement ajustables par une modification de leur épaisseur, nous caractérisons le chargement d'électron à température ambiante de nanoparticules individuelles formées par évaporation thermique sur un film de 6 monocouches de NaCl. Nous montrons comment la combinaison de la technique *e*-EFM et de simulations électrostatiques par éléments finis peut être utilisée pour révéler les propriétés électroniques et morphologiques de nanoparticules d'or individuelles. Ainsi, l'énergie de chargement, la capacitance, la fréquence de passage par effet tunnel et la forme approximative des nanoparticules ont été déterminées. Des simulations numériques montrent que la capacitance totale est dominée par la capacitance mutuelle entre la nanoparticule et l'électrode. En comparant avec les valeurs expérimentales, déterminées par une mesure de l'énergie de chargement, on montre que les nanoparticules devraient être modélisées par des sphères tronquées pour réduire la capacitance mutuelle avec le substrat. Cette observation a un impact fondamental pour le design de circuits nanoélectroniques dans lesquels les composantes doivent avoir des capacitances définies, étant donné que celles-ci déterminent les effets de couplage et de chargement.

La flexibilité de la technique de fabrication et le fait que toutes les mesures ont été effectuées *in situ* sur des échantillons dans des conditions ultra propres rendent le système attrayant pour de futures études. En particulier, cette approche peut être utilisée pour étudier le couplage entre des points quantiques et l'activité catalytique de nanoagrégats d'or à température ambiante.

Acknowledgements

I have had the great opportunity to work in the Nanoscience and Scanning Probe Microscopy Group led by Prof. Peter Grütter at McGill University. With his knowledge and experience, he created an excellent place to learn and push the limits of atomic force microscopy. I would like to thank all of the past and present members of the group for their kindness and helpfulness, which have made my time both productive and pleasant. I would like to thank my supervisor, Prof. Peter Grütter, who has allowed me great flexibility in reaching long-term research goals. With this freedom I had the chance to work on various research projects that often were not originally planned. It gave me the opportunity to enjoy Physics and explore many new things, which later led to the majority of results presented here.

I am genuinely grateful to Dr. Yoichi Miyahara, who supported me with his expert knowledge and kept me motivated with his positive outlook. I thank him also for his enormous help in keeping the JEOL microscope running so efficiently. I would like to thank Dr. Shawn Fostner and Dr. Jessica Topple, who introduced me to the JEOL lab several years ago and taught me how to use the microscope. They both provided advice and assistance to my research project, and the instrument even after they had moved on. I also want to thank all three of them for their help as the co-authors of my scientific papers based on the work presented herein.

I would like to thank Dr. David Oliver for his precious time reading my thesis and for his constructive comments. Once again I thank Dr. Jessica Topple who gave me this delightful LaTeX template.

I want to thank William Paul for great discussions on many subjects. Most importantly, I am extremely grateful for his help in finding me a new office space, where I could finally enjoy access to natural light. After so many years of work in a basement lab, it gave me a new source of information on weather conditions other than the underground tunnel connecting the Wong and Rutherford buildings.

Thanks to everybody that has served time in the JEOL lab with me. Discussions and time spent with Zeno Schumacher, Matthew Rigby, Monserratt Lopez,

Dr. Margaret Magdesian, Dr. Fernando Suarez, and Dr. Nela Durisic made my work easier and more enjoyable.

My research has also been supported by many others in the Physics Department at McGill. I would like to give my special thanks to Pascal Bourseguin and Francois Poirier for machining multiple components for the JEOL experimental setup. I would like to thank Robert Gagnon for his help in sample preparation lab and Leo Nikkinen for numerous suggestions and assistance with electronics. Also, I thank Dr. Sabrina Relaix and Julien Lhermitte for helping me with X-Ray diffraction of iron whiskers, and Prof. Mark Sutton for access to his lab equipment.

I thank Antoine Roy-Gobeil for discussion on single-electron charging experiments, sharing his samples with me, and translating my English abstract into French.

My PhD work was financially supported by Vanier Canada Graduate Scholarship. I thank the Government of Canada for this generous support. I also would like to acknowledge the help that I received from Prof. Kenneth Ragan and Ms. Janet Walker from the Graduate and Postdoctoral Studies Office while applying for this award.

Finally, I thank my family and friends. The experimental work and writing for this thesis took much of my leisure time, which we should have otherwise spent together.

Statement of Originality

The following aspects of the work contained herein constitute original scholarship and an advancement of knowledge. Results which have led to publications are noted with corresponding citations. Specific contributions include:

1. Reactive growth of MgO films on Fe(001) surfaces studied by low-energy electron diffraction and atomic force microscopy. In particular, a protocol was established to grow MgO films with terraces that have an average size of 10 nm, which is a significant improvement compared to other preparation methods.

   [Tekiel, A.; Fostner, S.; Topple, J.; Miyahara, Y.; Grütter, P. Reactive growth of MgO overlayers on Fe(001) surfaces studied by low-energy electron diffraction and atomic force microscopy. *Appl. Surf. Sci.* **2013**, *273*, 247-252]

2. The detailed characterization of epitaxy and growth of ultra-thin NaCl films on the Fe(001)-p(1×1)O surface. In particular, it was found that covering the Fe(001) surface with a monolayer of oxygen allows for growing the NaCl film in a near perfect layer-by-layer mode.

   [Tekiel, A.; Topple, J.; Miyahara, Y.; Grütter, P. Layer-by-layer growth of sodium chloride overlayers on an Fe(001)-p(1×1)O surface. *Nanotechnology* **2012**, *23*, 505602]

   This article was featured on the cover page of *Nanotechnology* (Issue 50).

3. Fabrication of a nanoscale system for studying single-electron charging of individual Au nanoparticles by room-temperature atomic force microscopy. The system consists of an ultra-thin NaCl film that acts as a tunnel barrier and metal nanoparticles used as electron-confining nanostructures, formed by thermally evaporating Au onto the NaCl surface.

4. Observation and characterization of single-electron charging of individual Au nanoparticles at room-temperature by atomic force microscopy. In this study electron addition energy, capacitance and tunneling rates of individual Au nanoparticles were measured.

5. Electrostatic simulations based on finite element method used to determine the contributions to the total nanoparticle capacitance and model the shape of the nanoparticles.

   3.-5. [Tekiel, A.; Miyahara, Y.; Topple, J.; Grütter, P. Room-temperature single-electron charging detected by electrostatic force microscopy. *ACS Nano* **2013**, *7*, 4683-4690]

Contributions of Co-authors

This thesis is based on three published papers and I am the lead author of all of them. I have conducted the data collection, analysis, and manuscript preparation for each article. I would like to thank Prof. Peter Grütter for access to his lab equipment. I gratefully acknowledge the support and assistance of my co-authors, whose contributions to publications are described below:

1. Tekiel, A.; Topple, J.; Miyahara, Y.; Grütter, P. Layer-by-layer growth of sodium chloride overlayers on an Fe(001)-p(1×1)O surface. *Nanotechnology* **2012**, *23*, 505602. *Appears in Chapter 7*.

   J. Topple and Y. Miyahara were involved in operation of the apparatus required for the experiments of this article. All co-authors were involved in discussions regarding the research concepts and presentation of data, as well as manuscript preparation.

2. Tekiel, A.; Fostner, S.; Topple, J.; Miyahara, Y.; Grütter, P. Reactive growth of MgO overlayers on Fe(001) surfaces studied by low-energy electron diffraction and atomic force microscopy. *Appl. Surf. Sci.* **2013**, *273*, 247-252. *Appears in Chapter 6*.

   S. Fostner, J. Topple and Y. Miyahara were involved in operation of the apparatus required for the experiments of this article. All co-authors were involved in discussions regarding the research concepts and presentation of data, as well as manuscript preparation.

3. Tekiel, A.; Miyahara, Y.; Topple, J.; Grütter, P. Room-temperature single-electron charging detected by electrostatic force microscopy. *ACS Nano* **2013**, *7*, 4683-4690. *Appears in Chapter 8*.

   Y. Miyahara was involved in data collection, analysis, and numerical simulations, and together with J. Topple were involved in operation of the apparatus required for the experiments of this article. All co-authors were involved in discussions regarding the research concepts and presentation of data, as well as manuscript preparation.

List of Abbreviations

2/3D	Two/three dimensional
AES	Auger electron spectroscopy
AFM	Atomic force microscopy/e
AM	Amplitude modulation
BE	Back electrode
e-EFM	Single-electron sensitive electrostatic force microscopy
DFT	Density functional theory
ENV	Environment
FEM	Finite element method
FIB	Focused ion beam
FM	Frequency modulation
GMR	Giant magnetoresistance
HOMO	Highest occupied atomic orbital
HV	High voltage
KPFM	Kelvin probe force microscopy
L	Langmuir, 1 L $= 10^{-6}$ Torr·s
(L)CPD	(Local) contact potential difference
LEED	Low-energy electron diffraction
LHe	Liquid helium
LN_2	Liquid nitrogen
LUMO	Lowest unoccupied atomic orbital
ML	Monolayer
MOSFET	Metal-oxide semiconductor field-effect transistor
MTJ	Magnetic tunnel junction
NC	Non-contact
NP	Nanoparticle
PLL	Phase-locked loop
RFA	Retarding field analyzer

RT	Room temperature
SEM	Scanning electron microscopy/e
SET	Single-electron transistor
SPM	Scanning probe microscopy/e
STM	Scanning tunneling microscopy/e
TEM	Transmission electron microscopy/e
TMR	Tunneling magnetoresistance
UHV	Ultra-high vacuum
VCO	Voltage controlled oscillator
VLS	Vapor-liquid-solid
XRD	X-Ray diffraction

Contents

1

Motivation

Low-dimensional systems (2D and less) and nanostructures have dominated much of modern electronics. There are several well-established technologies that have been used since decades, such as metal-oxide semiconductor field-effect transistors (MOSFETs) and semiconductor heterostructures. More recently, newer technologies based on fundamental discoveries related to the magnetism in ultra-thin magnetic layers, such as giant magnetoresistance (GMR) effect [1] and inter-layer exchange coupling [2, 3], have created a new field of spin-based electronics.

Technological progress in this area is typically related to improvements in fabrication. A good example is offered by magnetic tunnel junctions (MTJs), where using a crystalline MgO tunnel barrier instead of amorphous barrier layers made of AlO_x or TiO_x leads to a much larger room-temperature magnetoresistive effect [4]. Tunnel barriers are very sensitive to the presence of defects that can cause unwanted phenomena, such as scattering or trapping of charges. For this reason there has been growing interest for more than a decade in improving the quality of MgO films on the Fe(001) surface, in order to further increase the tunneling magnetoresistance ratio to much higher values theoretically predicted to be obtainable.

Ultra-thin insulating films, in particular oxide films, attract considerable attention due to their special properties differing from the corresponding bulk crystals. Insulating films find applications as tunnel barriers in electronic and magnetic devices [5] and as layers separating the gate in MOSFETs. They are also technologically important in catalytic systems, chemical sensors and functional coatings [6]. Although significant strides have been made in recent years in these fields, it is still difficult in many cases to grow high-quality tunnel barriers. The work described in this thesis attempts to advance the growth of epitaxial tunnel barriers on crystalline substrates. First, we improve the quality of

MgO films grown on Fe(001) by using a reactive deposition method, which will be discussed further in Chapter 6. The developed fabrication protocol produces an interface with well-ordered terraces and a much higher quality compared to the typically used growth method by electron beam evaporation. Second, Chapter 7 will demonstrate that covering the Fe(001) surface with a monolayer (ML) of oxygen promotes layer-by-layer growth of NaCl films with a quality that has not been observed on any metallic substrate.

Fabrication techniques also play a key role in the continuous trend of miniaturization. In many domains of technology related to electronics and optics the components are progressively reduced down to nanoscale dimensions, where very often new quantum phenomena occur. One of them is tunneling, where electrons manifest their wave nature. In conventional electronic devices, such as field-effect transistors, tunneling manifests as leakage between different device regions and is a fundamental limitation to miniaturization. In contrast, single-electron electronics takes advantage of these quantum effects to create new categories of devices that can mimic the behavior of conventional counterparts [7, 8]. In such systems, where the components are connected by tunnel barriers and coupled capacitively to external electrodes, the transport is dominated by single-electron effects. Among such phenomena, Coulomb charging plays a key role in many systems, including single-electron transistors and single-electron memory devices. Here again, the difficulty lies in creating high-quality and defect-free structures at the nanoscale [7]. However, in this size regime the challenge is not only to control the formation of structures, but also to understand the influence of structure on function, specifically optical and electronic properties. In particular, measurement of the capacitance between the components of nanoscale circuits and understanding its origin is crucial for improving such devices in order to work reliably at room temperature [7, 9].

Characterization of local electronic properties becomes increasingly challenging as structures are reduced to nanoscale dimensions. Methods based on transport measurements and conventional charge sensing are limited in flexibility since they require lithographic techniques to fabricate nanoscale electrodes. A large part of the motivation for this thesis is the development of atomic force microscopy, specifically electrostatic force microscopy with single-electron sensitivity

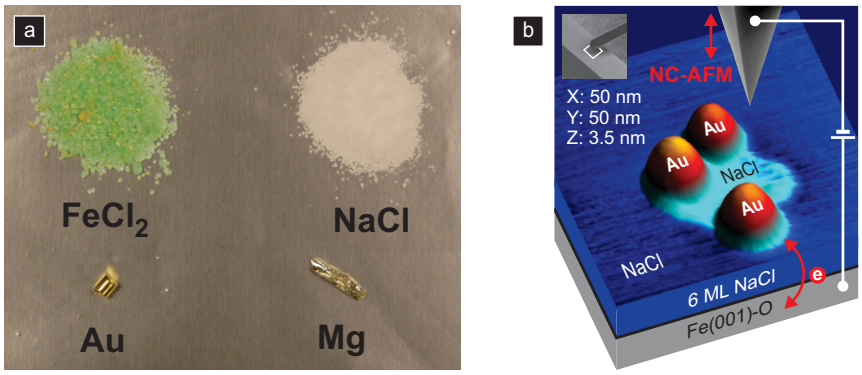

Figure 1.1: (a) Solid chemicals ($FeCl_2$, NaCl and Au) used together with molecular hydrogen and oxygen to fabricate a nanoscale system for studying single-electron charging shown in (b) that consists of a 6 monolayer thick NaCl film grown on the Fe(001)-p(1×1)O surface and 3.5 nm tall Au nanoparticles. In (a) Mg for reactive growth of MgO films is also shown.

(*e*-EFM), as a tool to probe local electronic properties of nanostructures. The details of this approach, which instead of prefabricated electrodes uses a cantilever as a movable gate to charge individual nanoparticles (NP) supported on an insulating ultra-thin film via single-electron tunneling from the back electrode, will be discussed further in Chapter 8. The amount of information that the *e*-EFM technique can provide is impressive. It can measure the electron addition energy, the capacitance, and tunneling rates, all in a non-invasive way. Most importantly, because it can not only measure electronic properties of individual nanoparticles but also image the topography of the studied system, it offers a powerful means of exploring structure-property relationships.

How is fabrication related to *e*-EFM? First, the *e*-EFM technique requires a special relation between tunneling rates and the cantilever resonance frequency to achieve maximum sensitivity. In this thesis this requirement is satisfied by using an NaCl film as a tunnel barrier and modifying its thickness relative to the cantilever response. Second, in order to observe single-electron charging at room-temperature, the electron-confining nanostructures have to be sufficiently small so that the characteristic energy related to manipulation of a single-electron, called the addition energy, exceeds the thermal energy at room temperature. In this work, we characterize single-electron charging at room temperature of individual

Au nanoparticles formed after thermally evaporating Au onto the NaCl. By controlling the amount of the deposited material, the size of the nanoparticles can be easily adjusted. Figure 1.1a shows solid chemicals used together with molecular hydrogen and oxygen to fabricate a nanoscale system for studying single-electron charging schematically presented in Figure 1.1b. It consists of a 6 monolayer thick NaCl film and 3.5 nm tall Au nanoparticles. Using reduction of a ferrous chloride powder in a hydrogen atmosphere, Fe whiskers with {001} orientation of side-surfaces are home-grown, which will be covered in Chapter 5. Starting from the Fe(001) surface, all subsequent preparation and characterization steps are performed in ultra-high vacuum, which guarantees that the system stays free of unknown contaminants. Using molecular oxygen the Fe(001) surface is transformed into Fe(001)-p(1×1)O which allows for growing NaCl on top of it layer by layer. In the final step Au is thermally evaporated onto the NaCl film to form metal nanoparticles.

The work described in Chapter 8 will present a proof-of-principle experiment, where single-electron charging is detected using the *e*-EFM method at room temperature. The size of Au nanoparticles used in this work is small enough to induce single-electron effects that have a classical electrostatic origin. This together with the simple design of the studied system allows for describing the system using finite element electrostatic modeling. It will be shown that such a combination of experimental and theoretical techniques provides a versatile means for characterizing Au nanoparticles that is beyond abilities of other experimental methods. As will be discussed further in Chapter 8, in our modeling the shape of an individual Au nanoparticle is determined to be a truncated sphere. Because of the complex 3D morphology of the nanoparticles, which is highly curved, this information cannot be provided by scanning probe microscopy (SPM) that can only access the surface of the sample exposed to the SPM probe. Among other characterization techniques, only transmission electron microscopy (TEM) is capable of measuring 3D shapes of individual nanoparticles, however TEM sample preparation methods can lead to modifications of the surface atomic structure of the sample [10]. In this aspect, the *e*-EFM method can operate entirely *in-situ* and guarantees more definite conditions under which the characterization is performed. Specifically, the *e*-EFM technique along with finite element electrostatic

simulations can be used to characterize chemical activity of Au nanoparticles, and smaller clusters, including the morphological information that is important for analyzing steric effects. Chapter 9 will discuss a hypothetical experiment whereby the *e*-EFM method could be used to probe changes in electronic quantum energy levels of individual Au clusters due to interaction with reactants.

Outline

This thesis is organized as follows: Chapter 2 gives a brief overview of growth and properties of ultra-thin insulating films, in addition to theoretical background on Coulomb blockade phenomena and single-electron charging. In Chapter 3 the experimental methods used are introduced. This is followed by description of instrumentation in Chapter 4. Chapter 5 addresses growth of Fe whiskers and preparation of the Fe(001) surface. In Chapter 6 the Fe whiskers are used as substrates for reactive growth of MgO films. We then describe the growth of NaCl films on the Fe(001)-p(1$\times$1)O surface in Chapter 7. In Chapter 8 the NaCl film is used to fabricate a system consisting of Au nanoparticles to study single-electron charging at room temperature, which is followed by finite element electrostatic simulations. Finally, conclusions and outlook are presented in Chapter 9.

2

Theoretical background

2.1 Growth of ultra-thin insulating films

Growth of well-ordered ultra-thin [1] insulating films on crystalline substrates is of key importance for electronics, and is crucial to numerous areas of fundamental research, such as friction and catalysis. On crystalline substrates, well-ordered ultra-thin films of high quality can be fabricated by epitaxial growth, where the structure of the substrate determines the orientation of the deposited film. This section describes the fundamental physical processes taking place during the epitaxial growth of ultra-thin films in ultra-high vacuum (UHV).

2.1.1 Nanoscale processes during growth

From the experimental point of view, in ultra-high vacuum materials are commonly deposited onto surfaces by thermal evaporation. Heating of materials in UHV increases their vapor pressure, creating a flux of particles that reach a surface. Usually special evaporators, so-called Knudsen effusion cells, are used to form a homogeneous flux of evaporated material over a sufficiently large area. The Knudsen design consists of a uniformly heated crucible acting as an isothermal enclosure with a small aperture opening. When the free path of particles is larger than the size of the aperture, the Knudsen cell generates a flux with cosine angular intensity distribution, which can be collimated to form a uniform beam. Depending on the deposited material, the particles arrive at the surface in a form of either

1. A precise definition of an *ultra-thin film* is not easy, because there is no simple way to distinguish this category from the large class of thin films. From a practical point of view, one tends to classify films of thickness below 100 nm as ultra-thin films, as in this range structures and properties of thin films start to differ from the corresponding bulk counterparts.

atoms or molecules. The latter case adds additional degrees of freedom, as molecules usually do not possess spherical symmetry [11]. For the sake of brevity, such effects are not discussed in this brief introduction.

Growth of materials takes place far from thermodynamic equilibrium and is determined both by thermodynamic and kinetic factors. The out-of-equilibrium character of growth means that the energy state of the system can depend on preparation conditions leading to different film morphologies. This dependence can be used to control the film structure by adjusting the preparation parameters, which include the deposition rate and the sample temperature. When a particle arrives at the sample surface, thermalization occurs almost instantaneously, as it is substantially faster than other subsequent processes, such as diffusion and nucleation. This means that thermally activated surface processes are determined by the temperature of the substrate onto which the material has been deposited [2]. In the initial stage of growth, a particle adsorbs on the surface with a positive adsorption energy, E_a. The rate at which adsorbed particles desorb from the surface is given by $\nu_\mathrm{a} \exp\left(-\frac{E_\mathrm{a}}{k_\mathrm{B}T}\right)$, where ν_a is a frequency parameterizing this process that can weakly depend on sample temperature T. The adsorption can be categorized into physisorption and chemisorption by the interaction strength and mechanism between the adsorbate and the substrate. In physisorption, the energy of interaction is largely due to the van der Waals force and amounts $\sim$50-500 meV/atom, while energies 1-10 eV/atom are typical of chemisorption [14].

The two primary parameters determining the growth are diffusion and deposition rates [15]. The first process is responsible for the transport of adsorbed particles, which on a flat terrace involves random hopping on the surface crystalline lattice and is thermally activated. The mean square distance traveled by an adsorbate per unit time is called the diffusivity, D, and is characterized by the Arrhenius law, similarly to the desorption process above. When the material is deposited at a constant rate F, the ratio D/F corresponds to the average distance the adsorbate has to travel in order to meet another adsorbate. If the deposition is slower than the diffusion (large D/F), adsorbates will have enough time to move on the surface and explore favorable adsorption sites. This corresponds to growth

2. We neglect here transient diffusion, i.e. the possibility that atoms condensing on a surface continue to move on it in an excited state, in which their mobility may exceed that under ordinary thermal conditions. For the importance of transient mobility see [12, 13].

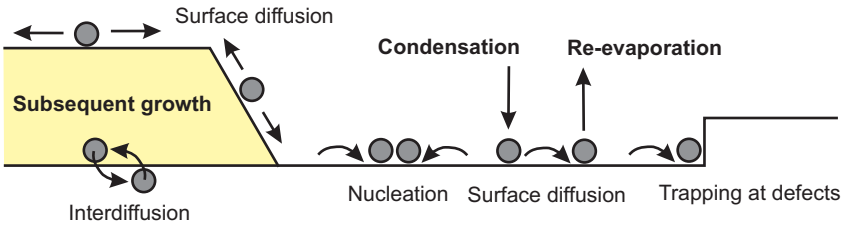

Figure 2.1: Kinetic processes during growth on a surface.

close to equilibrium. In contrast, if D/F is small, growth is dominated by kinetic effects leading to metastable structures. The value of D can be controlled by the sample temperature during growth. It should be also emphasized that there is a difference between evaporation onto a warm substrate, and evaporation onto a substrate kept at room temperature followed by post-annealing. In the former case, the distance between the adsorbates is determined by the deposition rate, while in the latter case it is related to the total amount of the deposited material.

At the atomic scale, the kinetic processes during growth on a surface can be summarized as in Figure 2.1. During growth close to equilibrium, there is both condensation and re-evaporation of the material. Adsorbates can diffuse on the surface and group together. Nucleation can start from trapping at defects like step edges, which are energetically favorable adsorption sites, as well as directly on flat atomic terraces. Among others the following factors decide the final morphology of the grown structure:

- thermodynamic factors, such as equilibrium shapes of the adsorbate structures, especially the critical size of a nucleus that can develop into a larger island,
- sticking coefficients,
- defects and their impact on nucleation,
- deposition rate,
- diffusivity and its anisotropy,
- Ehrlich-Schwöbl barrier [16, 17].

The thermodynamic phenomena manifest themselves during growth close to equilibrium and determine e.g. the equilibrium shape of crystal nuclei. In the formation of such nuclei the surface energy plays a dominant role, which in the

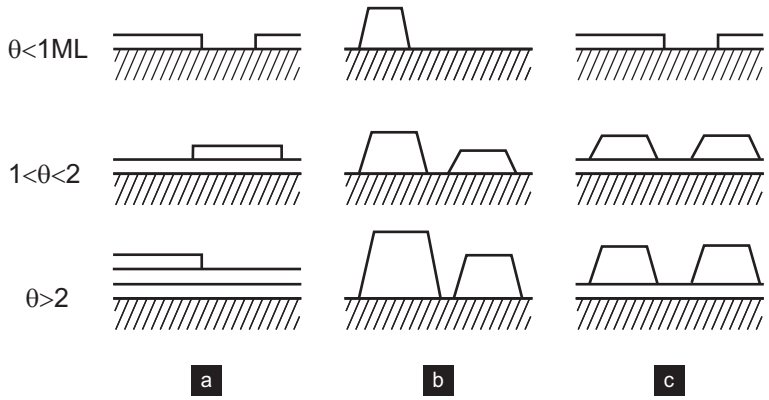

Figure 2.2: Three growth modes shown as a function of coverage θ. (a) Layer-by-layer/Frank-van der Merwe. (b) Island/Volmer-Webber. (c) Mixed/Stranski-Krastanov.

case of a crystal is defined as $E_\gamma = \frac{W}{2A}$, where W is the work needed to create the surface by cleaving the crystal, and A is the area of each of the two surfaces produced. At the atomic scale, E_γ is related to breaking of interatomic bonds, which means that E_γ is anisotropic and can depend on temperature.

Growth close to equilibrium can be realized experimentally by slow deposition of the material or deposition at elevated sample temperatures. Under such conditions, one distinguishes three growth modes:

1. **Layer-by-layer/Frank-van der Merwe**, shown in Figure 2.2a, where the deposited atoms/molecules interact more strongly with the substrate than with each other [18].
2. **Island/Volmer-Webber**, shown in Figure 2.2b, which is the opposite case, i.e. the deposited atoms/molecules interact more strongly with each other than with the substrate [19].
3. **Mixed/Stranski-Krastanov**, shown in Figure 2.2c, where after completion of several atomic layers, the material starts to grow in the island mode [20].

The above-mentioned growth modes were systemized by Bauer using the concept of surface energies [21]. During deposition of material A onto material B, the film grows layer by layer if $E_\gamma^{\mathrm{A}} < E_\gamma^{\mathrm{B}} + E_\gamma^*$, where E_γ^{A} and E_γ^{B} are the surface energies of material A and B, respectively, and E_γ^* is the interface energy between the two surfaces. If $E_\gamma^{\mathrm{A}} > E_\gamma^{\mathrm{B}} + E_\gamma^*$, then the island growth mode is preferred. The

mixed growth mode, also called Stranski-Krastanov mode, can be accounted for by the dependence of E_γ^* on the thickness of the deposited film, as a result of strain at the interface.

2.1.2 Oxide ultra-thin films on metals

The interest in crystalline oxide ultra-thin films has developed amongst other reasons because bulk metal oxides, due to their large band gap, are incompatible with many surface characterization methods that use electrons. In particular, surfaces of such poorly conducting crystals cannot be characterized by scanning tunneling microscopy (STM). Two materials have greatly contributed to the understanding of metal oxide surfaces, namely MgO and rutile TiO_2. The reason why TiO_2 has become so popular is that Ti is a transition metal and can exist in several stable valence states. When the substrate loses O atoms, which is common during annealing or sputtering, the excess electrons left on the surface by O atoms can be transfered to neighboring Ti atoms effectively leading to an n-type doping of the crystal [22]. In contrast, only one state (+2) dominates Mg chemistry, and a similar reduction of metal ions is impossible in the case of MgO. Consequently, making the substrate oxygen deficient does not improve its conductivity. The reason why MgO has become a model system among non-transition metal oxides is its simple *rock-salt* crystallographic structure. However, the progress in surface science of MgO has been much slower than of TiO_2, which is related to the following two factors. First, as mentioned above the number of methods suited to characterization of insulating surfaces is limited. Second, preparation of well-ordered and charge-neutral surfaces is very challenging. As reported by Barth *et al.* [23], the majority (95%) of MgO(001) samples prepared by cleavage result in surfaces that cannot be imaged.

The difficulty in surface preparation has led researchers to focus on ultra-thin insulating films grown on metallic substrates as substitutes for bulk oxide surfaces. MgO has a simple cubic *rock-salt* structure with a lattice parameter of 4.21 Å, which should allow for a commensurate growth on various *fcc* and *bcc* metallic substrates with a (001) surface orientation (see Table 2.1). The misfit was calculated from the relative difference between the lattice parameters of the substrate

Metal	Ag	Au	Cr	Fe	Mo
Structure	*fcc*	*fcc*	*bcc*	*bcc*	*bcc*
Lattice parameter	4.09 Å	4.08 Å	2.89 Å (4.09 Å)	2.87 Å (4.06 Å)	3.15 Å (4.45 Å)
Misfit	2.9%	3.2%	3.0%	3.7%	-5.5%

Table 2.1: MgO has a simple cubic *rock-salt* structure with a lattice parameter of 4.21 Å, which should allow for commensurate growth on various *fcc* and *bcc* metallic substrates with a (001) surface orientation. The lattice parameters in parentheses were calculated by multiplying the original values by $\sqrt{2}$, which corresponds to a rotation of the two lattices in respect to each other by 45°.

(a_{S}) and the (001)-oriented film (a_{F}):

$$\frac{a_{\mathrm{F}} - a_{\mathrm{S}}}{a_{\mathrm{S}}}. \tag{2.1}$$

Relatively low misfit values allow commensurate MgO films to be grown on several (001)-oriented metal surfaces. MgO films on Ag [24–26], Mo [27] and Fe [28, 29] are amongst the most studied systems, including SPM characterization in real space. However, even the best films contain a high quantity of defects, such as dense networks of misfit dislocations and very small terraces (understood as flat areas separated by atomic steps). The characteristic distance d between misfit dislocation can be defined as:

$$d = \frac{a_{\mathrm{F}} a_{\mathrm{S}}}{|a_{\mathrm{F}} - a_{\mathrm{S}}|}. \tag{2.2}$$

For MgO films on Ag, Mo and Fe, d takes values within 8-12 nm. In the case of Fe(001) the misfit leads to a network of defects that can be described by a glide of $\frac{1}{2}\langle 011\rangle$ dislocations on $\{011\}_{\mathrm{MgO}}$ planes of the MgO film [28]. This type of defect produces a monoatomic step at the surface, increasing the roughness of the film, which can be observed during SPM characterization (see Chapter 6).

Growth of MgO films is very challenging from the experimental point of view. In a UHV environment MgO films are usually deposited onto Fe(001) substrates by electron beam evaporation from a stoichiometric MgO target [29, 30] and the resulting beam is composed mainly of magnesium and oxygen, both in an

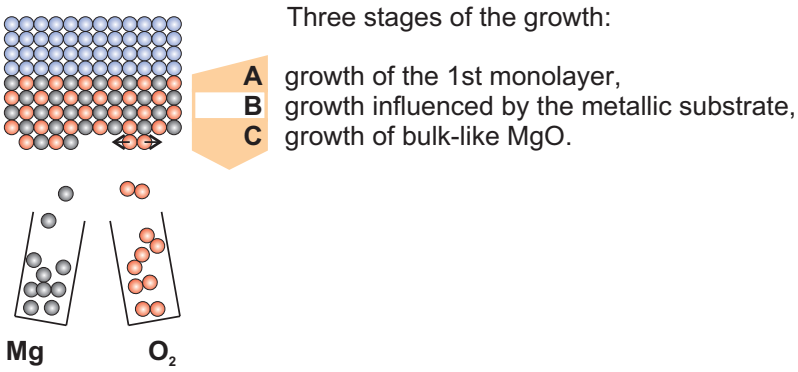

Figure 2.3: MgO is essentially grown from two separate sources of magnesium and oxygen, which must react on the substrate in order to nucleate MgO molecules. Next, MgO molecules diffuse and build MgO islands. There are three stages of such growth, each potentially requiring different growth parameters, as it is taking place on a dissimilar substrate.

atomic form [31]. Alternatively, MgO films can be grown by the reactive deposition of Mg in an O_2 atmosphere, which is a common method used to grow MgO films on Ag(001) and Mo(001) surfaces. In both cases, MgO is essentially grown from two separate sources of magnesium and oxygen, which must react on the substrate in order to nucleate MgO monomers (in the case of molecular oxygen, an O_2 molecule has first to dissociate). Next, MgO monomers diffuse and build MgO islands. Figure 2.3 shows that there are three stages of such growth, each potentially requiring different growth parameters, as it is taking place on a dissimilar substrate: (i) growth of the 1st monolayer, (ii) growth of several consecutive layers under conditions perturbed by the metallic substrate and (iii) growth of bulk-like MgO.

2.1.3 Alkali halide ultra-thin films

Alkali halide ultra-thin films can be grown on a variety of substrates covering metals, semiconductors and insulators [32]. The quality of such ultra-thin films can be much higher compared to MgO films, especially on closely lattice matched AIII-BV compound semiconductors [33]. This difference is explained by the fact that alkali halides such as NaCl and KBr evaporated thermally form predomin-

antly molecular monomers, and thus their growth is much better controlled due to the reduced complexity of on-surface nucleation [34–36].

When NaCl is deposited at low coverages on (111) and (001) surfaces of metals, such as Al(111) [37], Cu(111) [38–40], Au(111) [41] or Ag(001) [42, 43], it forms flat rectangular islands indicating a (001) termination of the NaCl film. The formation of the second and the third ML starts before the completion of the first ML, which corresponds to the Volmer-Weber growth mode (see Figure 2.2b). On (111)-oriented surfaces a (001)-oriented film with a *rock-salt* structure cannot be grown epitaxially at a micrometer scale due to the number of equivalent orientations between the substrate with a threefold symmetry and the film with a fourfold symmetry. This difference limits the application of alkali halide films on metal (111) surfaces as adjustable tunnel barriers. Nevertheless, such nanometer islands can be used in STM experiments, where the tunneling is restricted to the area defined by an STM tip [44].

Metal surfaces with a (001) orientation are better suited for growing epitaxial films of *rock-salt* alkali halides, but due to surface energies the films still grow in the Volmer-Weber or the Stranski-Krastanov mode. Experimental examples include KBr films on Cu(001) [45], and NaCl on Ag(001) [42, 43]. In the latter case, although the misfit between the *fcc* Ag(001) surface and the NaCl film is only $\approx$ 3% in the (4×4) structure, growth is incommensurate with a significant mosaic spread [46].

The problem of not wetting the metal surface by alkali halides lies in the weak adsorbate-substrate interaction. This situation can be improved when alkali halides are deposited onto surfaces of semiconductors. Three systems should be mentioned here, because they have been characterized by SPM techniques: (111) oriented films of CaF_2 on Si(111) [47, 48], NaCl films on Ge(001) [49], and KBr on InSb(001) [33]. The latter case represents a system where the substrate was selected from a wide family of AIII-BV compound semiconductors so as to match the lattice of the KBr film. Due to a stronger substrate-adsorbate interaction, the KBr film can be grown in a near perfect layer-by-layer mode on InSb(001).

2.1.4 Properties of ultra-thin insulating films

Ultra-thin films of insulating materials often exhibit unusual properties compared to the corresponding surfaces of bulk crystals. One of the best examples is adsorption of small Au clusters on ultra-thin MgO films. Sterrer *et al.* demonstrated that Au atoms when deposited on an ultra-thin MgO film on Ag(001) are negatively charged, in contrast to Au atoms on bulk MgO [50]. Charging of Au on MgO/Ag(001) is caused by a spontaneous flow of charge through MgO. There are several interesting consequences of this charge transfer, which attracted significant attention recently. The extra charge causes the shape of adsorbates to be different [50], but more importantly it has a direct consequence on the reactivity of supported Au clusters.

The different behavior of Au atoms and clusters on ultra-thin MgO films is related to the alignment of the highest occupied atomic orbital (HOMO) and the lowest unoccupied atomic orbital (LUMO) with respect to supporting metal Fermi level E_{F}. As a result, this potential difference can lead to spontaneous electron tunneling through the insulating film. When the HOMO of the adsorbate is above E_{F}, electrons can be transferred to the metal substrate. When LUMO is below E_{F}, i.e. the electron affinity of the adsorbate is larger than E_{F}, electrons can flow from the metal substrate to the adsorbate.

There is a substantial difference between bulk insulating crystals and ultra-thin films in the way that they react to charged adspecies. Considering defect-free insulating films, such a charge transfer is accompanied by an induced image charge. In addition, because an ultra-thin insulating film has an increased lattice flexibility, its ionic lattice undergoes a polaronic-like distortion that contributes to the stabilization process of charged adsorbates. However, the properties of the film lattice quickly approaches the properties of the bulk when the film thickness is increased, and consequently self-charging of clusters is not observed on thicker films. Indeed it was shown experimentally for a 20 ML thick film on Mo(100) that the Au clusters are neutral [51].

The charging phenomenon described above is independent of surface defects, but additional effects can occur in the presence of defects. It is known for example that MgO films, especially when grown on Mo(001) with a large misfit, are characterized by dislocations that can be loaded with electrons [6]. Upon adsorp-

tion of Au such electron-rich defects on MgO films act as very effective nucleation sites, and can be also responsible for charging of Au clusters [52].

Work function of ultra-thin dielectric films on metals

As already mentioned, the electron transfer between the metal substrate and adsorbate through the dielectric film depends on the position of HOMO and LUMO in respect of E_F. In metals, the direct measure of E_F is the work function, but the presence of an insulating film usually significantly modifies the work function of the substrate. There are two major contributions to the change in work function induced by an ultra-thin dielectric film. First, the film can be bound to the metal by chemical bonds that involve a charge transfer. This will cause the E_F to shift and create a dipole at the metal/insulator interface. For example, this corresponds to the $SiO_{2.5}$ films grown on Mo(112), where the charge is transferred from Mo to O atoms at the interface leading to an increase in work function from 4.2 to 4.9 eV [53]. However, in the case of an ionic film, such as MgO or NaCl, the charge transfer is negligible [54]. The change in work function, which can still be significant [53, 55], is caused by an electrostatic effect. This effect is called "compressive" and is caused by exchange or Pauli repulsion. The metal is polarized by the electrostatic field of the dielectric layer pushing the charge back into the metal and changing the surface dipole.

2.1.5 In search of adjustable tunnel barriers

The best known crystalline tunnel barrier whose thickness can be adjusted is an MgO film on Fe(001) [29]. Such MgO films are used in magnetoelectronics [5], where they have been identified as promising building blocks of MTJs. In the case of Fe(001)/MgO/Fe(001) MTJs, a crystalline MgO film leads to a high tunneling magnetoresistance ratio (TMR) [30, 56]. However, as mentioned above MgO films are still characterized by a large amount of defects, such as dense networks of misfit dislocations and very small terraces. The complex defect-dominated structure of the film makes it difficult to compare reliably with theoretical predictions.

Among other well-ordered crystalline tunnel barriers, one should mention ultra-thin Al_2O_3 films formed on NiAl(110) after annealing in oxygen, Cu_2N mono-

layers grown on the clean Cu(100) substrate by N_2 sputtering and subsequent annealing, as well as the already mentioned bilayer thick NaCl islands on Cu(111) [39, 40]. The thickness of all these films is fixed at 1 or 2 atomic layers. Nevertheless, due to their defect-free character such films have found applications in multiple studies focused on fundamental science, where they are used to decouple adsorbates from a metal substrate in SPM experiments. Al_2O_3/NiAl(110) films have been used in studying quantization of electronic states in individual Ag particles by Nilius *et al.* [57]. Using NaCl films on Cu(111) Gross *et al.* measured the charge state of an Au adatom with non-contact (NC) AFM [58], while Loth *et al.* [59] demonstrated control of magnetism of single atoms on a Cu_2N monolayer using STM.

2.2 Metal nanoparticles as quantum dots

When the size of a metal particle is reduced to nanoscale dimensions, the energy required to add an electron to it increases. This energy is called the addition energy, E_{add}, and there are two size regimes, which are characterized by different contributions to the total value of E_{add}. If the electron quantization energy is much smaller than the electrostatic charging energy, the nanoparticle has quasi-continuous electronic bands. The two contributions can be equal at a size of ≈ 1 nm [7], and for larger nanoparticles (> 3 nm) the cost of adding an electron consists only of an electrostatic contribution defined in the following way:

$$E_{\text{add}} = E_{\text{C}} = \frac{e^2}{C}, \tag{2.3}$$

where C is the total nanoparticle capacitance.

However, if the size is further reduced and is of the order of the de Broglie wavelength of conduction electrons, which for gold is approximately 0.6 nm [60], the particles lose their bulk-like electronic structure. Such particles exhibit discrete energy levels, E_N, that are separated by $\Delta E_{\text{level},N} = E_{N+1} - E_N$. Thus for very small particles, which we call here nanoclusters, the addition energy has two components:

$$E_{\text{add}} = E_{\text{C}} + \Delta E_{\text{level},N}. \tag{2.4}$$

If the particle size is sufficiently small, E_{add} can exceed the thermal energy, $k_{\text{B}}T$, which opens up a possibility for manipulation of single electrons. There are two regimes in which single-electron charging effects can occur:

– **classical limit**, when $E_{\text{C}} \gg k_{\text{B}}T \gg \Delta E_{\text{level}}$,

– **quantum limit**, when $E_{\text{C}} \sim \Delta E_{\text{level}} \gg k_{\text{B}}T$.

This thesis focuses on single-electron charging of Au nanoparticles at room temperature, which given the high value of $k_{\text{B}}T$ corresponds to the classical limit. For our analysis, we assume the constant interaction model, which in the classical limit states that the addition energy does not depend on the number of electrons on the nanoparticle, i.e. the nanoparticle capacitance is constant.

In the classical limit, it is also justified to use the orthodox theory developed by Kulik and Shekhter [61], which makes the following assumptions:

1. The energy quantization inside the conductor is ignored, i.e. $\Delta E_{\text{level}} = 0$, and the charging energy is the dominant contribution to the electron addition energy.
2. The time of electron tunneling through the barrier is negligibly small compared to other time scales, especially the time between tunneling events.
3. Simultaneous tunneling events are ignored.

The tunneling of a single electron through a tunnel barrier is a random event, with a certain rate Γ that corresponds to the probability of the tunneling event per unit time and effectively determines the average time between the tunneling events.

2.2.1 Coulomb blockade and single-electron box

A single-electron box is the conceptually simplest device utilizing single-electron effects. It consists of a nanoparticle (or a nanocluster in the quantum limit) that is separated from a source electrode by a tunnel barrier. Another electrode, called the gate, can be used to apply an external electric field. The gate is implemented such that tunneling between the nanoparticle and gate is not allowed, which means that the gate and the nanoparticle are only capacitively coupled. By controlling the gate bias voltage, electrons can be added or removed to/from the nanoparticle. E_{add} is the characteristic energy associated with this process and is

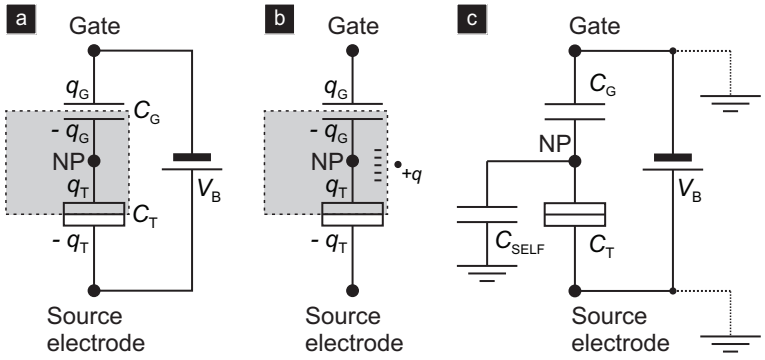

Figure 2.4: (a) A single-electron box that consists of a nanoparticle (NP) separated from a source electrode by a tunnel barrier. Another electrode that is is only capacitively coupled, called the gate, can be used to apply an external electric field and induce charging of the nanoparticle. The polarization charges on the tunnel junction, q_{T}, and the gate capacitor, q_{G}, can take continuous values. (b) If a charged defect happens to be close to the nanoparticle, it will polarize its surface by creating an image charge. (c) The self-capacitance C_{SELF}, understood as a capacitance with reference to an infinitely distant grounded plane, can be conceptually added to the capacitance of either the tunnel barrier or the gate by grounding the source electrode or the gate, respectively.

related to the size of the nanoparticle. If the size is sufficiently small, E_{add} can exceed the thermal energy, $k_{\mathrm{B}}T$, and cause the number of electrons on the nanoparticle to be fixed for a given gate bias voltage. Additional charging of the nanoparticle will then require a sufficiently high bias applied to the gate in order to attract an electron to the nanoparticle and increase the the number of electrons by one. This effect is known as the Coulomb blockade. Depending on the electric field applied by the gate, an electron can be also removed from the nanoparticle.

In order to observe such single-electron tunneling there is also an additional condition to be met. Observation of Coulomb blockade effects requires that the electron wave function is localized on the nanoparticle. Using the uncertainty principle one can obtain a requirement for the resistance of the tunnel barrier that has to be larger than the resistance quantum h/e^2 (h is the Planck's constant) [3]. This allows for the charge to be well localized on the nanoparticle.

For a two-terminal capacitor with capacitance C, the charging energy is $\frac{e^2}{2C}$.

3. From $\Delta E \Delta t > h$, where $\Delta E \sim e^2/C$ is the characteristic energy of adding one electron to the nanoparticle with capacitance C, and $\Delta t = RC$ is the characteristic time of this process, where R is the resistance of the tunnel barrier, then $e^2 R > h$.

However, in the single-electron box the nanoparticle is charged with electrons from a source kept at a certain potential. This configuration causes the characteristic energy related to loading the nanoparticle with an extra electron to be $\frac{e^2}{C}$. This can be seen by analyzing the free energy of the system, $G = U - W$, where U is the potential energy due to all charged capacitors in the system, and W is the work done by the voltage source. According to Figure 2.4a the polarization charges on the tunnel junction (q_{T}) and the gate capacitor (q_{G}) can take continuous values. They are related to the number of electrons on the nanoparticle, n, and the voltage source kept at V_{B}, in the following way:

$$q_{\mathrm{T}} - q_{\mathrm{G}} = -ne, \tag{2.5}$$

$$\frac{q_{\mathrm{T}}}{C_{\mathrm{T}}} + \frac{q_{\mathrm{G}}}{C_{\mathrm{G}}} = V_{\mathrm{B}}, \tag{2.6}$$

where C_{T} and C_{G} is the tunnel junction capacitance and the gate capacitance, respectively. The capacitive energy of the system is then expressed by:

$$U = \frac{q_{\mathrm{T}}^2}{2C_{\mathrm{T}}} + \frac{q_{\mathrm{G}}^2}{2C_{\mathrm{G}}} = \frac{e^2n^2}{2C_\Sigma} + \frac{1}{2}\frac{C_{\mathrm{T}}C_{\mathrm{G}}V_{\mathrm{B}}^2}{C_\Sigma}, \tag{2.7}$$

where C_Σ is the total nanoparticle capacitance. The work done by the voltage source during charging of the charge-neutral nanoparticle with n electrons is:

$$W = \int I(t)V_{\mathrm{B}}\mathrm{d}t = q_{\mathrm{G}}V_{\mathrm{B}} = ne\frac{C_{\mathrm{G}}}{C_\Sigma}V_{\mathrm{B}} + \frac{C_{\mathrm{T}}C_{\mathrm{G}}V_{\mathrm{B}}^2}{C_\Sigma}. \tag{2.8}$$

This gives the free energy G defined as a quadratic function of n and V_{B}:

$$G = \frac{e^2n^2}{2C_\Sigma} - ne\frac{C_{\mathrm{G}}}{C_\Sigma}V_{\mathrm{B}} - \frac{1}{2}\frac{C_{\mathrm{T}}C_{\mathrm{G}}V_{\mathrm{B}}^2}{C_\Sigma}. \tag{2.9}$$

The nanoparticle will be charged with a fixed number of n electrons, if this state is energetically the most favorable. Using the free energy, this means that $G(n) < G(n \pm 1)$, which gives the following conditions for n and V_{B}:

$$\left(n - \frac{1}{2}\right)\frac{e}{C_{\mathrm{G}}} < V_{\mathrm{B}} < \left(n + \frac{1}{2}\right)\frac{e}{C_{\mathrm{G}}}. \tag{2.10}$$

The charge on the nanoparticle stays fixed as long as the voltage V_B satisfies the conditions given by Inequalities 2.10. However, if the V_B is equal to one of the aforementioned limits, two states, e.g. n and $n+1$, are equally favorable. In this situation, the charge on the nanoparticle oscillates between the two values, which means that the Coulomb blockade has been lifted. Such charge oscillations will happen periodically with an increase in V_B and are separated by $\Delta = e/C_G$. The detection of Coulomb oscillations in a single-electron box as a function of V_B gives the separation Δ between the consecutive oscillations, providing a direct measure of the gate capacitance, C_G.

One can define a parameter α, commonly called the lever-arm, which expresses the ratio between the voltage across the tunnel barrier, $V_T = q_T/C_T$, and V_B:

$$\alpha = \frac{V_T}{V_B}. \tag{2.11}$$

From the circuit diagram shown in Figure 2.4a, in the charge neutral state $\alpha = C_G/C_\Sigma$. As will be discussed in Section 3.1.3 and Chapter 8, the *e*-EFM method, which in its simplest form is described by a single-electron box, can also measure the α parameter in addition to Δ. In this way one can relate Δ to the voltage across the tunnel barrier and characterize the separation of energy levels of the nanoparticle. Knowledge both of α and Δ gives the value E_{add}:

$$\Delta = \frac{E_{add}}{e\alpha} \tag{2.12}$$

with:

$$E_{add} = \frac{e^2}{C_\Sigma}. \tag{2.13}$$

2.2.2 Background charge and self-capacitance

Single-electron devices are sensitive to the quality of the tunnel barrier which can contain electron trapping centers and other two-level systems [7]. If such a charged defect happens to be close to the nanoparticle, it will polarize its surface by creating an image charge (see Figure 2.4b). This extra charge, which is very difficult to characterize, will have to be incorporated in the analysis of the free energy to determine new Coulomb blockade thresholds. The background charge, due to

its random character, makes this analysis almost impossible and has remained the major issue impeding single-electron electronics. A solution to this problem is fabrication of well-ordered, almost defect-free tunnel barriers, which this thesis focuses on. In addition, scaling down the nanoparticle size, which is in any case required for room-temperature operation, can reduce this problem by making it statistically less likely.

A related problem in single-electron devices is self-capacitance, which has an unambiguous definition for conductors in free space. In the case of a sphere of radius R_1, this is the smallest limit of the capacitance of a spherical capacitor, when the radius of the outer sphere, R_2, approaches infinity:

$$\lim_{R_2 \to \infty} \frac{4\pi\epsilon_0}{\frac{1}{R_1} - \frac{1}{R_2}} = 4\pi\epsilon_0 R_1, \tag{2.14}$$

where ϵ_0 is the vacuum permittivity. The self-capacitance of some other shapes can be calculated analytically, and in general it is proportional to a linear dimension of the object. When the object is coupled to other electrodes this definition becomes less clear, but it is still possible to distinguish a capacitance with reference to an infinitely distant grounded plane that, in a multi-terminal configuration, can be calculated using a capacitance matrix formalism [62].

One can ask what impact the self-capacitance has on single-electron devices. According to Figure 2.4c, in the case of a single-electron box it will lead to an additional polarization charge on the nanoparticle, whenever the nanoparticle is at a non-zero potential. Consequently, the α parameter will depend on the point from which the voltage is referenced, i.e. how the system is grounded. As shown in Figure 2.4c, the self-capacitance, C_{SELF}, can be conceptually added to the capacitance of either the tunnel barrier or the gate. In each case, the device will still exhibit Coulomb blockade behavior with similar thresholds as given by Inequalities 2.10, where C_{G} has to be replaced by αC_{Σ}. Here C_{Σ} is the total nanoparticle capacitance that includes also C_{SELF}, and α is still defined as the the ratio between the voltage across the tunnel barrier and V_{B} (see Appendix A).

2.2.3 Electrostatic simulation using finite element method

This thesis takes advantage of COMSOL Multiphysics software (ver. 4.3a) created to solve a variety of physics problems using the finite element method (FEM). In FEM, the system is represented by an assembly of subdivisions called finite elements. These discrete elements are considered to be interconnected only at joints called nodes. Because the actual variation of a field variable, e.g. electrical potential, inside an element is unknown, the variation over each element is approximated by a simple function, such as polynomials. These approximating functions are defined by the values (and/or their derivatives) of the field variable at the nodes. When the relevant physical equations for the entire system are written and modified to incorporate the given boundary conditions, the new unknowns will be the nodal values of the field variable. By solving these equations the nodal values can be determined, and thus the approximating functions defining the variable over each finite element will also be known. A comprehensive overview of the theoretical background of FEM and its implementation in COMSOL is beyond the scope of this thesis. A complete description of the approach can be found in the official COMSOL documentation [63, 64].

One convenient way to solve a physics problem is to set it up with the assistance of templates that COMSOL Multiphysics provides in the form of its physics modes. This thesis uses the *Electrostatics* mode that is a part of the *AC/DC module*. In general, the *Electrostatics* application mode provides the equations, boundary conditions, and space charges for modeling electrostatic fields and solving for the electric potential. For instance, under static conditions the electric potential is given by Poisson's equation:

$$-\nabla \cdot (\epsilon_0 \nabla V - \mathbf{P}) = \rho. \tag{2.15}$$

In this equation, ϵ_0 is the permittivity of vacuum, $\mathbf{P}$ is the electric polarization vector, and ρ is a space charge density. The relevant interface condition at interfaces between different media (1 and 2) for this mode is:

$$\mathbf{n} \cdot (\mathbf{D_1} - \mathbf{D_2}) = \rho_S, \tag{2.16}$$

where **D** the electric displacement, ρ_S is the surface charge, and **n** is the normal vector to the interface.

At the user level, for a given geometry and boundary conditions COMSOL creates the geometry, mesh, studies and solver settings, and also handles the visualization and presentation of results. COMSOL can run the finite element analysis together with adaptive meshing and error control using a variety of numerical solvers. The *Electrostatics* application mode is available for 3D, 2D in-plane, and 2D axisymmetric models.

3

Experimental methods

3.1 Atomic force microscopy in ultra-high vacuum

This thesis uses ultra-thin insulating films which due to low electrical conductivity even at a thickness of several atomic layers are only compatible with certain characterization methods. In the case of insulating surfaces, the most important technique suited for high resolution imaging in real space is atomic force microscopy (AFM). AFM relies on forces that act between a force sensor with a sharp tip and a sample. The strength of the force depends strongly on the tip-sample distance. Relevant forces in AFM include chemical forces, but also forces not necessarily originating from an interaction between individual atoms or forces, which cannot be resolved with atomic resolution, such as van der Waals and electrostatic forces. In an AFM experiment the force sensor consists of a sharp tip attached to a cantilever that bends due to the tip-sample interaction. This deflection can be measured by a beam of light reflecting off the back side of the cantilever towards a photodetector. If the spring constant of the cantilever beam is known, AFM can provide absolute measurement of forces. More details about the AFM instrumentation can be found in Section 4.1.3. AFM can operate in either contact or dynamic NC mode. In contact AFM the tip is approached to the surface until the cantilever is deflected by a repulsive tip-sample interaction. Because AFM measures the sum of all interactions: repulsive short range forces in the contact area, and long-range attractive forces from the rest of the tip and cantilever, the loading on the sample can often exceed shear strength and lead to plastic deformation of the sample. In contrast, the dynamic NC operation mode is significantly less invasive. In this method the cantilever oscillates at (or close to) the resonance frequency with an amplitude of typically a few nanometers, which increases the

sensitivity allowing for measurements of forces down to the pN range. In this way, the tip can be held by the feedback system at a certain short distance from the sample (i.e. at the interaction set-point) without contacting the substrate. The following section describes the frequency modulation (FM) NC-AFM technique in more detail.

3.1.1 Frequency modulation non-contact atomic force microscopy (FM NC-AFM)

In NC-AFM the force sensor can be modeled by a damped harmonic oscillator:

$$m\ddot{z} + m\gamma\dot{z} + k_{\mathrm{N}}z = F_{\mathrm{drive}}(t) + F_{\mathrm{ts}}(z,t), \tag{3.1}$$

where m is the effective mass of the cantilever, z is the vertical position of the tip with respect to the equilibrium position, γ is the damping coefficient (due to internal friction in the cantilever), k_{N} is the spring constant of the cantilever, F_{drive} is the driving force and F_{ts} is the tip-sample force that depends on distance and time. The tip-sample interaction will influence the dynamics of the cantilever, which depends on the mode of operation used. In FM NC-AFM the cantilever is self-oscillated at its current resonance frequency. If F_{ts} is a conservative force, F_{drive} has to compensate $m\gamma\dot{z}$ in order to keep the oscillation stable. In this situation:

$$m\ddot{z} + k_{\mathrm{N}}z = F_{\mathrm{ts}}. \tag{3.2}$$

We can now consider a simple case, when the gradient of the F_{ts} force is constant over the oscillation cycle. In this situation, the effective spring constant, k_{eff}, can be approximated by $k_{\mathrm{eff}} = k_{\mathrm{N}} - \frac{\partial F_{\mathrm{ts}}}{\partial z} = k_{\mathrm{N}} + k_{\mathrm{ts}}$ and can be used to calculate the resonance frequency of the cantilever, $f = \frac{1}{2\pi}\sqrt{\frac{k_{\mathrm{eff}}}{m}} \approx f_0\left(1 + \frac{k_{\mathrm{ts}}}{2k_{\mathrm{N}}}\right)$, where $f_0 = \frac{1}{2\pi}\sqrt{\frac{k_{\mathrm{N}}}{m}}$. The spring constant k_{ts} takes negative values leading to a negative frequency shift for larger tip-sample separations where the stiffnesses of the attractive (k_{ATTR}) and repulsive (k_{REP}) tip-sample interactions satisfy: $|k_{\mathrm{ATTR}}| > |k_{\mathrm{REP}}|$.

However, the simple situation described above is usually not observed in practice, because the force gradient does not remain constant during the motion of the oscillating cantilever. Assuming that the oscillation of the cantilever is har-

monic with amplitude A and using canonical perturbation theory, the spring constant of the tip-sample interaction can be averaged over the oscillation cycle in the following way [65]:

$$\langle k_{\text{ts}}(z)\rangle = \frac{1}{\frac{\pi}{2}A^2}\int_{-A}^{A} k_{\text{ts}}(z-q)\sqrt{A^2-q^2}\mathrm{d}q, \tag{3.3}$$

and the induced frequency shift can be calculated from $\Delta f = f_0 \frac{\langle k_{\text{ts}}(z)\rangle}{2k_{\text{N}}}$. The following subsection discusses different force-distant relations, which can be directly used to calculate Δf. In general, for small oscillation amplitudes, the frequency shift is independent of the amplitude and proportional to the tip-sample force gradient k_{ts}, as shown above. However, for amplitudes that are large compared to the range of the tip-sample interaction, the frequency shift is a power function of the amplitude, $\Delta f \propto A^{-\frac{3}{2}}$ [66]. This relationship is later used for experimental calibration of the oscillation amplitude (see Section 4.2).

Conservative forces

Forces between the tip and the sample can be divided into various classes. The primary distinction made here is based on energy conservation during the oscillation cycle. Forces that are not delayed in time, i.e. have only an in-phase component and do not depend on the velocity of the cantilever, are conservative. This is in contrast to the *e*-EFM method (see Section 3.1.3 and Chapter 8), where the electrostatic force is delayed with respect to the tip oscillation and leads to energy dissipation.

Van der Waals forces (vdW) arise from the interaction between fluctuating dipoles in the atoms in the tip and the sample. Considering just two atomic dipoles, the vdW interaction leads to a very weak and usually attractive force. However, if the contributions from all tip and sample atoms are summed up, it can result in forces of several nN, which under certain experimental conditions can dominate the total tip-sample interaction. Taking a sphere placed close to a flat surface as an approximation of the tip-sample geometry, the vdW force is described by:

$$F_{\text{vdW}} = -\frac{HR}{6z^2}, \tag{3.4}$$

where H is a material-specific Hamaker constant (typically approx. 10^{-19} J), R is the tip radius, and z ($z \ll R$) is the tip-sample distance.

Electrostatic forces act between charges that can be present on the tip or the sample. Such charges can be the result of sample preparation or be localized (e.g. in ionic crystals). More commonly, electrostatic forces arise due to the tip-sample capacitance and the different work functions of the tip and the surface materials, which leads to a contact potential difference (CPD). If the tip-sample system is considered as a capacitor with a tip-sample separation-dependent capacitance C, the electrostatic force is given by:

$$F_{\text{el}} = -\frac{1}{2}\frac{\partial C}{\partial z}(V_{\text{B}} - V_{\text{CPD}})^2, \tag{3.5}$$

where V_{B} is the bias voltage applied between the tip and the surface, and V_{CPD} is the voltage corresponding to the CPD.

Electrostatic forces depend on the capacitance gradient, which is known analytically for some simple systems. Assuming for example a spherically terminated tip next to an infinite plane the F_{el} is [67]:

$$F_{\text{el}} = -\pi\epsilon_0 \frac{R^2}{z(z+R)}(V_{\text{B}} - V_{\text{CPD}})^2 \approx -\pi\epsilon_0 \frac{R}{z}(V_{\text{B}} - V_{\text{CPD}})^2, \tag{3.6}$$

where the approximation holds for small tip-sample separations ($z \ll R$), and ϵ_0 is the vacuum permittivity.

Chemical forces play the key role in high-resolution topography imaging due to their very short interaction range that typically is below 1 nm. They arise both from an overlap of electron wave functions and repulsion by the ion cores. The chemical forces can be described using model potentials, for example the Morse potential [66] and the corresponding force can be calculated by taking a gradient of the potential. Reaching atomic resolution in NC-AFM measurements requires operation at small distances that are comparable to the interaction range of chemical forces. Ideally, also the oscillation amplitude of the cantilever should be reduced to the typical range of the interaction as this maximizes the measured signal (see Equation 3.3) [68].

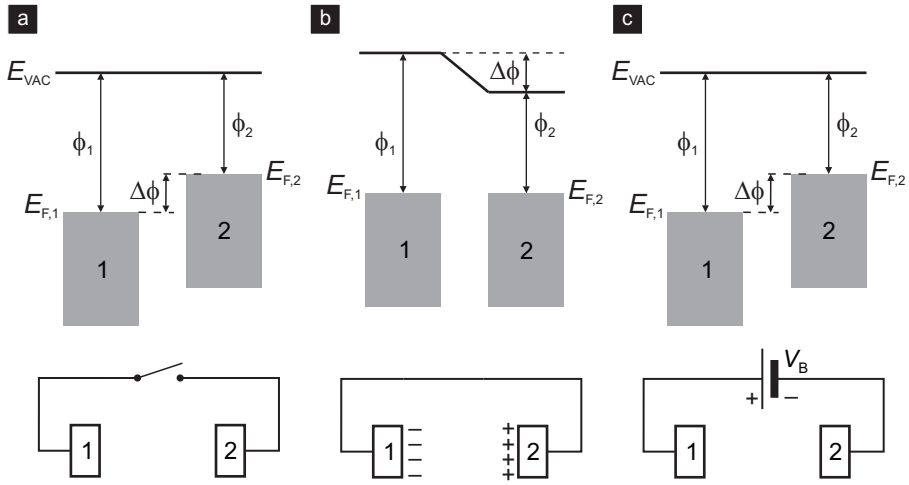

Figure 3.1: Energy diagrams of two metals with a different work function. (a) Both metal plates are electrically isolated. (b) An electrical connection leads to the equalization of the Fermi energies, $E_{\mathrm{F},1}$ and $E_{\mathrm{F},2}$. If the two plates are close to each other, they will attract each other. (c) An external potential can restore the initial positions of the Fermi energies and reverse the displacement of charges.

3.1.2 Kelvin probe force microscopy (KPFM)

A system of two different metals that are electrically isolated can be described by the energy diagram in Figure 3.1a, where each metal is characterized by its work function (ϕ_1 and ϕ_2). When the two metals are electrically connected by an external circuit, thermodynamical equilibrium among electrons is established once the chemical potential is equal across the system. This leads to the equalization of the Fermi energies, $E_{\mathrm{F},1}$ and $E_{\mathrm{F},2}$, and is realized by a displacement of charges, which in Figure 3.1b happens by a flow of electrons from plate 2 to plate 1. This displacement of charges causes two metals to be oppositely charged. If the two metallic plates are close to each other, they will attract each other, similarly to a parallel plate capacitor. However, an external potential can be applied to restore the initial positions of the Fermi energies, as shown in Figure 3.1c. This potential must be equal to the opposite value of the work function difference, $-\Delta\phi$. As a result, the charge distribution will resume the initial configuration, as in Figure 3.1a.

The original method proposed by Kelvin depends on the detection of a

charge flow between the plates of the capacitor. The most practical approach uses a technique based on a vibrating capacitor. In this method the plates of the capacitor vibrate with respect to each other effectively varying the capacitance. This modulation leads to a current $i(t)$:

$$i(t) = (V_{\mathrm{B}} - V_{\mathrm{CPD}})\frac{\partial C}{\partial t}. \tag{3.7}$$

If the external potential V_{B} is adjusted so that it is equal to V_{CPD}, then there is no charge on the plates and there is also no flow when the plates are vibrated.

In Kelvin probe force microscopy (KPFM), the modulating effect of V_{B} is observed not by measuring current, but by measuring electrostatic forces. To separate the electrostatic forces from other interactions and make the detection more sensitive, KPFM uses the lock-in technique whereby an additional AC voltage with amplitude V_{AC} and frequency ω is added to the DC potential across the tip and the sample. Now V_{B} has the following form:

$$V_{\mathrm{B}} = V_{\mathrm{DC}} + V_{\mathrm{AC}}\sin(\omega t). \tag{3.8}$$

In the absence of free charges, the electrostatic force can be calculated using Equation 3.5, which will result in three components:

$$F_{\mathrm{el}} = F_{\mathrm{DC}} + F_{\omega} + F_{2\omega}, \tag{3.9}$$

where

$$F_{\mathrm{DC}} = -\frac{1}{2}\frac{\partial C}{\partial z}\left((V_{\mathrm{DC}} - V_{\mathrm{CPD}})^2 + \frac{V_{\mathrm{AC}}^2}{2}\right), \tag{3.10}$$

$$F_{\omega} = -\frac{\partial C}{\partial z}(V_{\mathrm{DC}} - V_{\mathrm{CPD}})V_{\mathrm{AC}}\sin(\omega t), \tag{3.11}$$

$$F_{2\omega} = \frac{1}{2}\frac{\partial C}{\partial z}\frac{V_{\mathrm{AC}}^2}{4}\cos(2\omega t). \tag{3.12}$$

If the V_{DC} voltage compensates the CPD, the first harmonic at ω is nulled, and the DC component takes a constant value proportional to V_{AC}^2. Experimentally, there are two modes of operation of KPFM, namely the amplitude modulation (AC) mode and the FM mode. The latter technique was used in this work and is briefly

described below [69].

Frequency modulation mode of KPFM

The FM NC-AFM technique is sensitive to the gradient of the force. The corresponding frequency shift can be calculated from Equation 3.3. Consequently, the electrostatic force will result in a modulation of the fundamental mechanical resonance frequency of the cantilever at frequencies ω and 2ω. Typically, in FM KFPM the oscillation at ω is detected using a lock-in amplifier. There is an optimal region for the modulation frequency ω, which usually is around 1 kHz in typical AFM systems. The modulation frequency ω should not be too low, because if the microscope z-distance controller has enough time to react this can lead to a cross talk between the topography and the CPD signal. On the other hand, ω has to be within the bandwidth of the PLL frequency demodulator, which for one of the used models here (Nanosurf "easy PLL plus") was 1.3 kHz. During KPFM characterization, a feedback system adjusts the V_{DC} voltage to keep the amplitude of the modulation as small as possible. The filtered value of V_{DC} recorded above each surface point is used to create a CPD map (see Section 4.2 for more details).

3.1.3 Single-electron sensitive electrostatic force microscopy

The following brief review presents the basic principles of single-electron sensitive electrostatic force microscopy (*e*-EFM). This method will be discussed further in Chapter 8, although a full review of a detailed quantum mechanical treatment of the coupled cantilever-quantum dot system is beyond the scope of this thesis. Such a theoretical approach, which is needed to understand the experimentally observed frequency and dissipation line shapes, has been covered in detail elsewhere [70, 71]. When discussing specific concepts of the *e*-EFM method we will point the reader to those works for reference.

The *e*-EFM technique originates from scanning probe microscopy and can routinely access nanometer length scales. It allows for characterization of electronic properties of electron-confining nanoparticles that are supported on an ultrathin insulating film. Using *e*-EFM, electron addition energy, capacitance, and tunneling rates can be measured. The *e*-EFM technique offers an alternative approach

to characterize supported nanostructures and overcomes the difficulty of attaching the electrodes to nanoscale structures [70]. The essential part of the *e*-EFM method is an insulating film that separates the nanostructures under investigation from a back electrode and acts as a tunnel barrier, which is shown schematically using an example of an Au nanoparticle supported on an NaCl film in Figure 3.2a. To induce tunneling between the nanoparticle and the back electrode, the AFM tip is placed at a height within several nanometers above the nanoparticle. A DC bias voltage, V_{B}, is applied across the oscillating cantilever and the back electrode. Typically, the tip-sample separation (~ 5 nm) is large enough to make the tunneling between the tip and the nanoparticle negligible due to the large barrier height and width of the vacuum gap.

As shown in Figure 3.2b the potential drop between the nanoparticle and the back electrode, i.e. across the tunnel barrier, is a fraction of the applied bias voltage, αV_{B} ($\alpha < 1$). The $\alpha(x, y, z)$ parameter, which similarly to the case of a single-electron box described in Section 2.2.1 is called the lever-arm, depends on the lateral and vertical position of the tip. When the tip oscillates, α is modulated, giving rise to an effective modulation of the voltage across the barrier. Figure 3.2b shows that tunneling of an electron between the back electrode and the Au nanoparticle only takes place if the Coulomb blockade is lifted by selecting a proper value of V_{B} and tuning $e\alpha V_{\mathrm{B}}$ to one of the electrochemical potential levels of the nanoparticle. Under this condition, the oscillation of α leads to an oscillation of the number of electrons on the nanoparticle, N, between two neighboring ground states characterized by $N = n$ and $N = n + 1$ electrons. The oscillating charge on the nanoparticle causes both a resonance frequency shift, Δf, and damping of the cantilever, $\Delta\gamma$ [70, 71]. Although tunneling of electrons is a stochastic event, the average charge, $\langle N(t)\rangle$, follows the oscillating motion of the tip. As a result, the oscillating electrostatic force has not only an in-phase, but also a 90° out-of-phase component that leads to energy dissipation (which is a similar effect to the *Q*-factor degradation in the *Q*-control system used in amplitude modulation AFM [72]).

The rate of tunneling through the ultra-thin insulating film largely decides the sensitivity of the method by affecting the relative strength of the cantilever dissipation and frequency shift signals [73] which are measured in *e*-EFM. As will

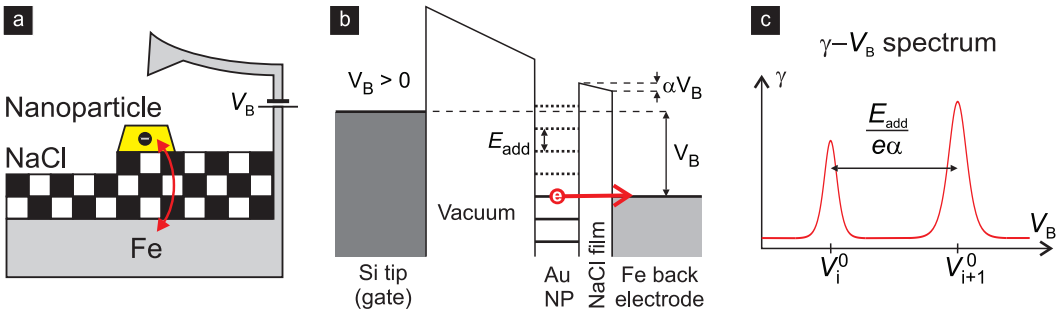

Figure 3.2: (a) The most essential part of the *e*-EFM method is an ultra-thin insulating film that separates studied nanostructures from a back electrode and acts as a tunnel barrier. An oscillating AFM tip is used as a local gate by applying an electric potential, V_B, between the back electrode and the tip. (b) Energy diagram of the system for positive sample bias allowing for sequential unloading of electrons. (c) In an electron addition spectrum an increase in γ (and Δf) appears near voltage values matching $e\alpha V_B$ with one of the electrochemical potential levels of the nanoparticle. The shape of the peaks are given by Equation 8.3, from which α can be extracted.

be discussed in Section 8.1, the dissipation of the cantilever per unit time, $\Delta\gamma$, is maximal when the tunneling rate is matched with the oscillation frequency of the cantilever, while the frequency shift, Δf, increases with increasing tunneling rate. This means that the signal could be optimized by a proper choice of the cantilever, however this is limited by the range of resonance frequencies (10-1,000 kHz) of commercially available AFM probes. Alternatively, the *e*-EFM technique can be made sensitive at room temperature by achieving full control over the tunnel barrier thickness and adjusting the tunneling rate to the cantilever resonance frequency.

The change in Δf and γ is maximal only during tunneling of an electron. This condition can be identified by placing the tip above a nanoparticle and sweeping V_B, simultaneously observing Δf and γ. Figure 3.2c schematically shows an electron addition spectrum, where an increase in γ appears near voltage values matching $e\alpha V_B$ exactly with one of the electrochemical potential levels of the nanoparticle, which lifts the Coulomb blockade. If the modulation of $e\alpha V_B$ caused by the cantilever oscillation is smaller than the thermal energy, a condition which is easily met at room temperature, the changes in Δf and $\Delta\gamma$ are described by a linear response [70, 74, 75]. In this case the shape of the Coulomb blockade peak is

known, and given by Equation 8.3, which can be used to extract the α parameter without any knowledge about the tip and sample. Once the α parameter is known, the addition energy, E_{add}, can be easily obtained from the separation of consecutive peaks in the γ-V_{B} spectrum being $E_{\text{add}} = \alpha e \left(V_{i+1}^0 - V_i^0\right)$. As will be further discussed in Chapter 8, a system investigated with *e*-EFM is equivalent to a single-electron box. In this situation E_{add} can be related to the total capacitance of the nanoparticle. Addition spectra recorded using both the frequency shift signal and the dissipation signal allow for extraction of tunneling rates (see Section 8.3.3).

3.2 Electron and X-Ray diffraction

Diffraction is one of the most important methods of investigating the structure of ordered systems, including bulk solids and solid surfaces. Diffraction techniques not only give information about the symmetry of the atomic or magnetic structure, but also provide insight into the type and distribution of defects. Given the small mean free path of electrons in solids, which is a few nanometers at electron energies of 10-1000 eV, a low-energy electron beam interacts only with the surface. This makes electron diffraction an excellent surface characterization tool, which is used in this work for investigation of clean conductive substrates, as well as substrates covered with insulating ultra-thin films. X-Rays have much higher penetration and consequently are sensitive to the structure of the entire sample. This type of diffraction is used to characterize the quality of grown iron whiskers.

3.2.1 Low-energy electron diffraction (LEED)

Low-energy electron diffraction (LEED) is a well-established surface characterization technique in UHV environments. Characterization of insulating surfaces is possible as long as no charging takes place. According to de Broglie's concept of matter waves, a particle with momentum p can be described by a wave of length $\lambda = \frac{h}{p}$, where h is Planck's constant. For electron energies of 15-150 eV, which are used in LEED, the wavelengths are ≈3-1 Å, respectively. Such lengths are comparable with lattice parameters of solids and low-energy electrons will therefore be diffracted by ordered surfaces provided that the electron beam is

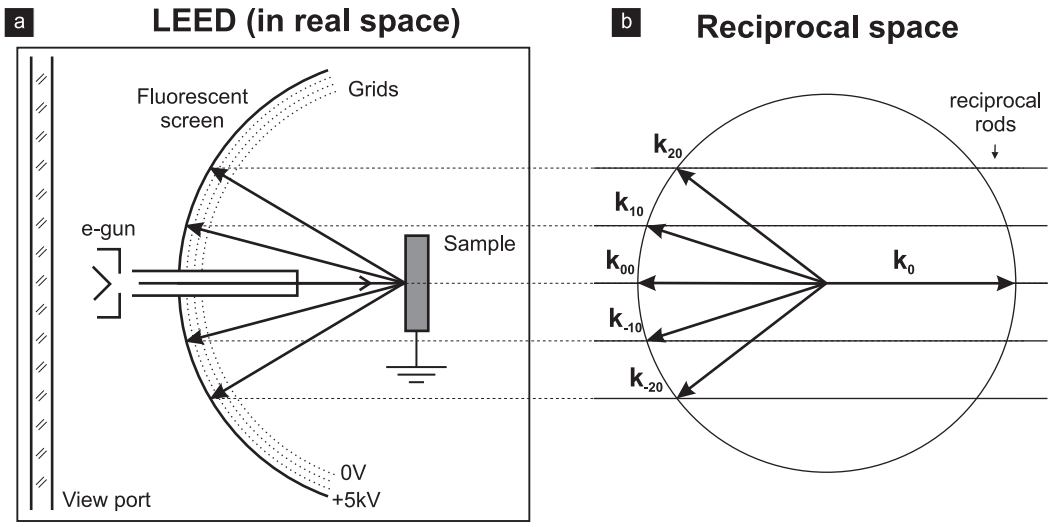

Figure 3.3: (a) Low-energy electron diffractometer. (b) The relationship between the LEED pattern and the 2D reciprocal space of the studied sample. The pattern formed on the fluorescent screen is an intersection of the reciprocal space with Ewald's sphere. Vector $\mathbf{k}_0$ is defined by the direction and the energy of the incident electron beam, and vectors $\mathbf{k}_{xy}$ indicate directions of elastically diffracted beams.

coherent[1]. Because the electron wavelength is comparable with the lattice parameter, the diffraction angles are large, which makes the observation possible with a simple fluorescent screen placed on the path of diffracted electrons.

When the incident electron beam is normal to the surface, as shown in Figure 3.3a, there is straightforward relation between the LEED pattern and the 2D reciprocal space of the crystal. The pattern formed on the fluorescent screen is an intersection of the reciprocal space with Ewald's sphere. Figure 3.3b shows a cross section of the 2D reciprocal space. Vector $\mathbf{k}_0$ is defined by the direction and energy of the incident electron beam, and vectors $\mathbf{k}_{xy}$ indicate directions of elastically diffracted beams. In the diffraction process, the intensity of the diffracted beam in direction $\mathbf{k}$ is related to the interference function that corresponds to the

1. The incident beam formed by an electron gun consists of electrons whose energy is characterized by thermal broadening due to the temperature of the cathode. Additionally, the beam is not perfectly collimated which leads to a distribution of electron velocities. In this way the electron gun is not a coherent source, but one can define a radius of coherence, i.e. a radius of a circle on the surface, inside which the incident beam is coherent [76]. For conventional LEED devices this radius is approximately 10 nm. Ultimately, the LEED pattern is created by a non-coherent superposition of diffracted coherent beams.

Fourier transform of the lattice causing the diffraction. For low-energy electrons this is the potential of the ion cores of surface atoms. This means that diffraction on ordered systems leads to well-ordered diffraction patterns. The LEED method is often used for a quick inspection of the sample quality, for both clean substrates and substrates covered by adsorbates. In the latter case the LEED pattern allows for determination of basic adsorption parameters, such as the size and the orientation of the unit cell of the adsorbed layer.

In the simplest approximation, the LEED pattern forms as a result of 2D electron diffraction on the surface. However, this model can be insufficient in the presence of defects, for example in the case of samples with multiple step edges. The Ewald construction for elastic scattering on such a quasi-2D surface lattice is conceptually presented in Figure 3.4a. In this situation, the reciprocal space cannot be modeled by a 2D approximation and qualitatively the reciprocal rods can have periodically varying intensity. This third Laue condition arises due to diffraction from a few underlying planes. Scattering from a quasi-2D surface has also another important consequence. If the energy of the primary beam is changed, the Ewald sphere will pass through regions of the reciprocal rods that are stronger or weaker, which effectively will lead to intensity dependence of Bragg spots on the beam energy. Figure 3.4 (panels b and c) shows also the correspondence between the real and reciprocal spaces in the case of other defects, such as mosaics and facets, which can be clearly identified by LEED.

To understand the essential features of the diffraction experiments used in this work, kinematic theory is sufficient. This approximation assumes that the scattering is elastic and that each particle undergoes only one scattering process. However, electron diffraction on systems including adsorbates and ordered defects can involve multiple scattering processes, and such simplified analysis should be used with caution.

3.2.2 High-resolution X-Ray diffraction (XRD)

Compared to low-energy electrons an X-Ray beam has a much larger absorption length, 4.2265 μm for Fe [78] (assuming a conventional source with a copper target). Consequently, the diffracted intensity provides information about

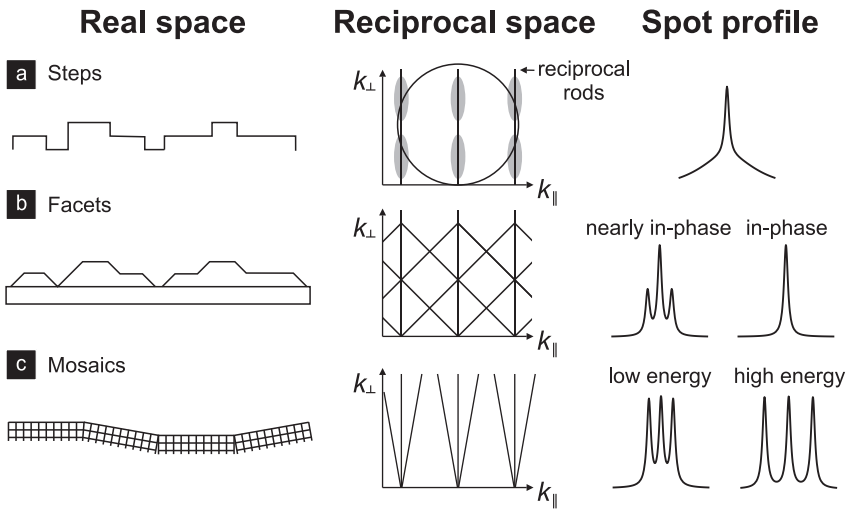

Figure 3.4: The Ewald construction for elastic scattering on imperfect lattices. (a) If the surface has multiple step edges, there is a third Laue condition arising due to diffraction from a few underlying planes. (b) A quasi-2D surface with facets. (c) A quasi-2D surface with mosaics. For Ewald construction on other defected surfaces see [77].

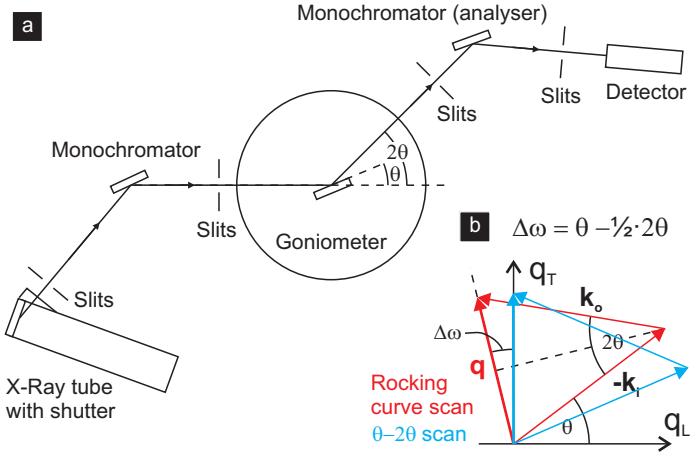

Figure 3.5: (a) A schematic diagram of a triple-crystal diffractometer. The detector position is denoted by 2θ, and θ refers to the sample orientation measured with respect to the incoming beam. (b) A θ-2θ scan and a rocking curve scan shown in the reciprocal space $(q_{\mathrm{L}}, q_{\mathrm{T}})$. The combination of the two scan types allows for recording 2D maps of diffraction reflections.

the bulk of the crystal. Similarly to LEED, XRD can be used to evaluate the perfection of a given crystal by studying the Bragg peaks. The diffraction pattern can be recorded with a high-resolution X-Ray diffractometer. Figure 3.5a shows a schematic diagram of a triple-crystal diffractometer that uses two crystals (e.g. made of Ge) as monochromators and a crystalline sample. The diffraction plane is determined by the position of the X-Ray source, the detector and the sample. The sample is aligned in such a way that the normal direction to the sample surface lies in the diffraction plane. In this configuration the orientation of the crystal can be described by only one Euler angle, ω. The detector position is usually denoted by 2θ, which is a symbolic name and should not be confused with θ referring to the sample orientation measured with respect to the incoming beam.

Conventional XRD devices use vacuum X-Ray tubes that contain a copper target (anode) bombarded by electrons from a tungsten filament (cathode). A high accelerating potential is applied between the anode and cathode which is sufficient to generate characteristic radiation from the copper target (K_α and K_β lines). A monochromator, which usually is a Si or Ge crystal with a (111)-oriented surface together with a set of slits, can be used to filter the X-Ray beam providing a source primarily characterized by the K_α line with 1.5406 Å wavelength (although the K_α line is a doublet, it used in the experiment to retain a high intensity of the beam).

A θ-2θ scan is used to determine the interplanar distance of the planes. In this type of a scan, the angle θ of the incoming beam with respect to the sample surface is varied, while simultaneously keeping the detector exactly at an angle of $2\theta = 2 \cdot \theta$ with respect to the incoming beam. As shown in Figure 3.5b, this corresponds to varying the magnitude of $\mathbf{q}$ while maintaining its orientation relative to sample normal. The angle 2θ at which a diffraction peak is observed, can be used to calculate the interplanar distance from the diffraction condition $\mathbf{q} = \mathbf{k_o} - \mathbf{k_i}$:

$$|\mathbf{q}| = 2|\mathbf{k_i}| \sin\frac{2\theta}{2} = \sqrt{h^2 + k^2 + l^2}\frac{2\pi}{a}, \tag{3.13}$$

where $\mathbf{k_o}$ and $\mathbf{k_i}$ are the wave vectors of the diffracted and the incident beam, respectively, hkl are the Miller indices and a is the lattice parameter of a cubic crystal system. In this scan the width of the Bragg peak can be measured, which allows for determination of the crystal quality.

Another type of scan used in XRD is a rocking curve scan. In such a measurement, the θ angle and the detector position 2θ are fixed at the Bragg angle of the corresponding reflection. A rocking curve scan is then recorded by changing the orientation of the sample by an angle $\Delta\omega = \omega - \omega_0$ around its equilibrium ω_0 with 2θ fixed (see Figure 3.5b). In a rocking curve scan the orientation of $\mathbf{q}$ is varied relative to sample normal while maintaining its magnitude allowing for measuring the detailed structure of diffraction peaks. The combination of the two scan types allows for recording 2D maps of diffraction reflections in the θ-2θ space. Given that the position of the $\mathbf{q}$ vector is fully defined by the θ and 2θ angles, the θ-2θ space can be simply transformed into the reciprocal space $(q_{\mathrm{L}}, q_{\mathrm{T}})$ using the relation:

$$\mathbf{q} = 2|\mathbf{k_i}| \sin\frac{2\theta}{2} \left(\sin(\omega - \omega_0), \cos(\omega - \omega_0)\right). \tag{3.14}$$

4

Description of instrumentation

This chapter describes in detail the UHV experimental setup used for fabrication of ultra-thin insulating films and metal nanostructures, as well as characterization of single-electron charging at room temperature.

4.1 Ultra-high vacuum apparatus

All experiments using the Fe(001) substrate are performed in two interconnected UHV chambers based on a commercial JEOL JSPM 4500a UHV AFM (see Figure 4.1). The UHV system consists of a preparation chamber, and a microscope chamber. Each chamber is pumped by a diode type sputter-ion pump (pumping speed 300 L/s for N_2, and 90 L/s for Ar, Satsuki SIP-300XH-T16) and a Ti sublimation pump (1,600 L/s for N_2, ULVAC PGT-3F). The sputter-ion pump includes a cathode made of a Ta board, which also allows for pumping noble gases. Given the high efficiency of the pumping system, the base pressure is in the low 10^{-11} mbar range in the preparation chamber, and 1×10^{-10} mbar in the microscope chamber. The system is equipped with a load-lock that is connected to the preparation chamber allowing for transfer of samples and AFM cantilevers between air and the UHV environment. The load-lock is pumped by a turbo-molecular pump (210 L/s for N_2, Pfeiffer TMU 261), backed by a sliding vane rotary vacuum pump (9.7 m^3/hr, Adixen 2010SD). During the Ar^+ sputtering that is a part of the preparation procedure of Fe(001) substrates (see Section 5.2), the ion pump in the preparation chamber is turned off, and the gate valve between the load-lock and the preparation chamber is opened. In this way the preparation chamber is pumped by the turbo-molecular pump, and achieves pressure $\approx 1 \times 10^{-9}$ mbar. Figure 4.2 provides detailed information about the components responsible for vacuum generation and control in the UHV system.

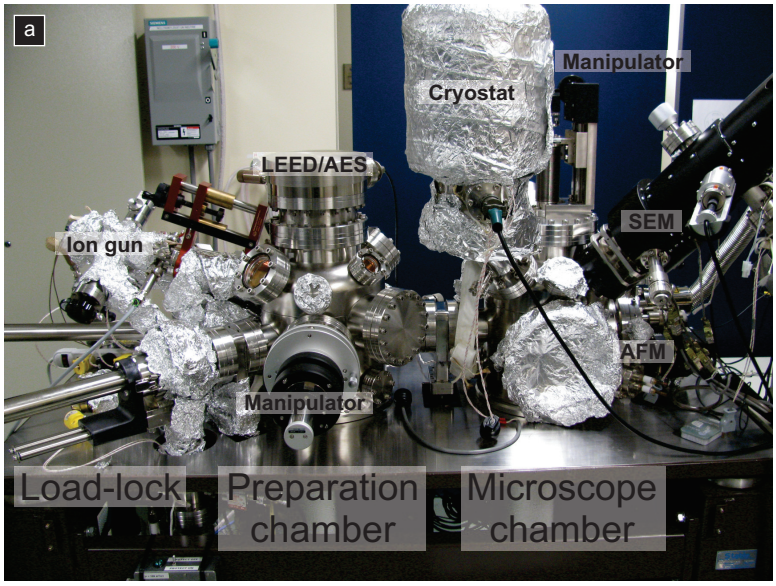

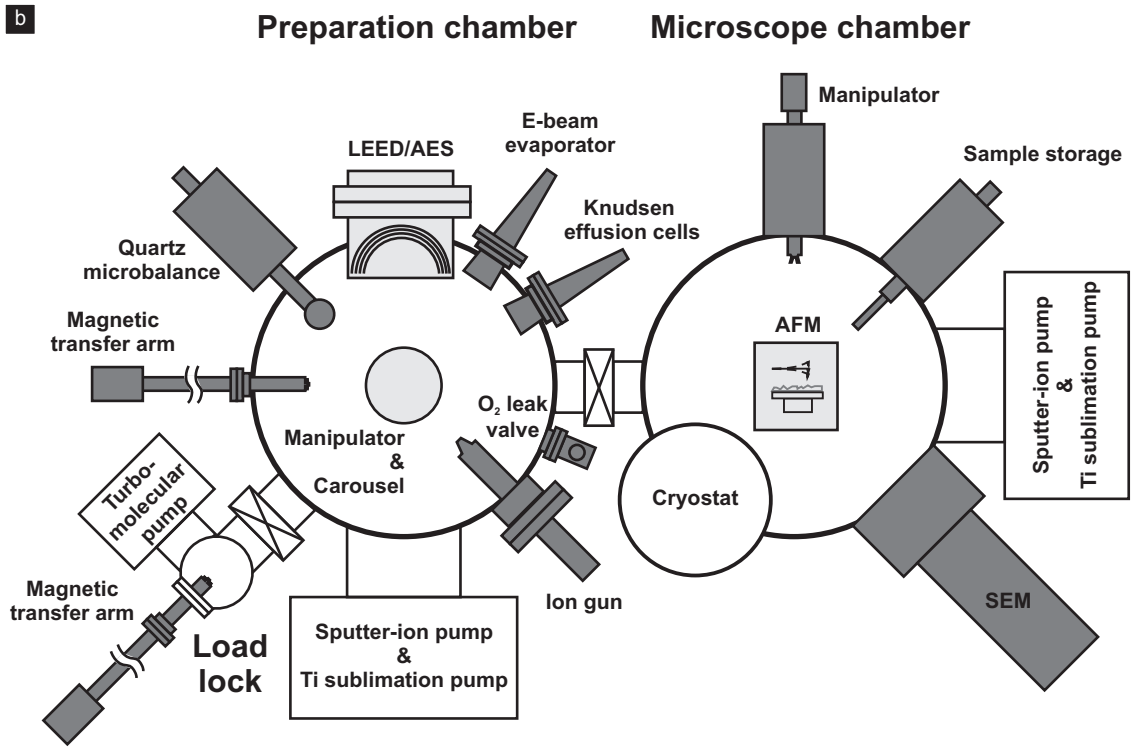

Figure 4.1: (a) The UHV system, which is based on a commercial JEOL JSPM 4500a UHV AFM, consists of a load-lock, a preparation chamber, and a microscope chamber. (b) Relevant surface preparation and characterization tools, as well as vacuum components.

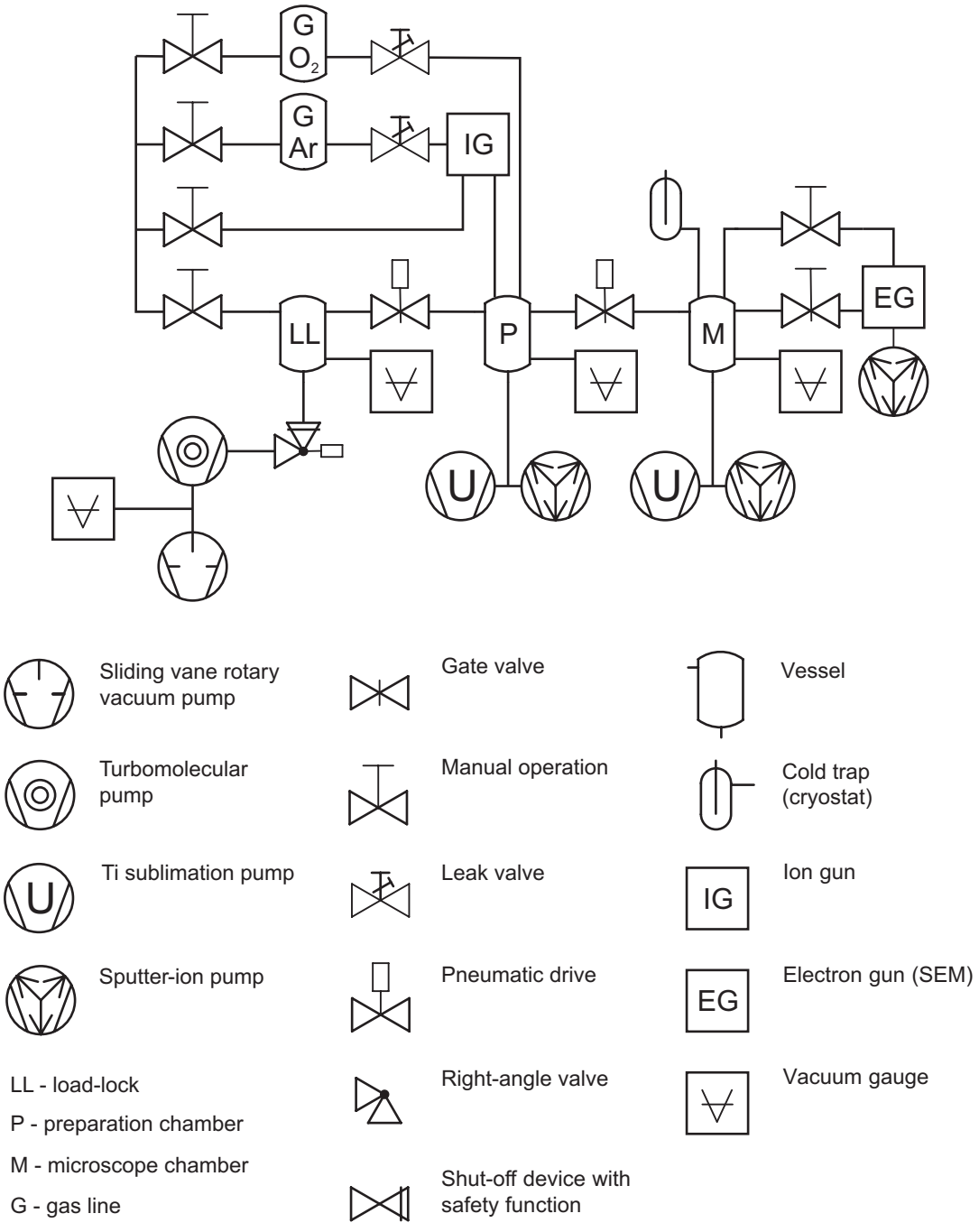

Figure 4.2: Components responsible for vacuum generation and control in the UHV system used.

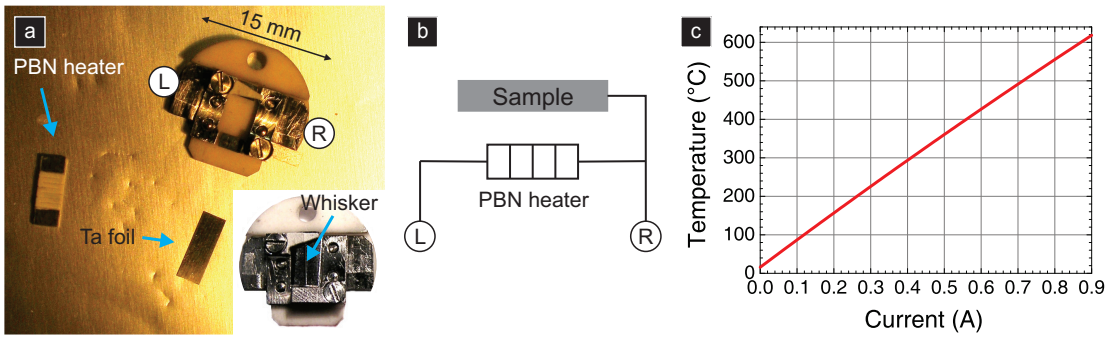

Figure 4.3: (a) The components of the sample holder; the inset picture shows the holder with an iron whisker installed. (b) The circuit diagram showing terminals connected to the heater and directly to the sample. (c) The temperature dependence on the heater current.

Two magnetically coupled rotating linear transfer arms provide the ability to transfer samples and tips within the vacuum system. The first transfer arm can move transferable elements from the load-lock to a carousel that acts also as positionable manipulator. The carousel has four positions in which carriers of tips or samples can be stored. A sample placed on the carousel can be accessed by various preparation tools, such as sputtering, annealing, Knudsen effusion cells, and e-beam metal evaporator. Three out of the four carousel positions provide electrical contact, which can be used for heating the sample or current collection during sputtering. The second transfer arm allows for moving samples and tips between the preparation and microscope chambers.

To provide sufficient vibrational stability, the UHV system is located in a special low vibration area in the basement of the Wong building. The UHV system is also mounted on a vibration damping air table. Inside the UHV system the microscope stage itself is supported on a set of springs that additionally hinder propagation of mechanical vibrations.

4.1.1 Sample holder

An iron whisker, which typically is 200 μm wide and 3-4 mm long, is mounted on a sample holder manufactured by JEOL (TM-51340) that has an integrated pyrolytic boron nitride (PBN) heater (see Figure 4.3). The main body of the holder is an insulating plate (Al_2O_3) that supports two metallic pads providing electrical

contact to the PBN heater. The core element of the heater is a piece of graphite that is covered with an insulating boron nitride layer. Next, a thin resistive pattern is deposited onto the PBN layer, and in the final step the entire structure is coated again with PBN, leaving only the two terminals of the resistive heater exposed. Such commercial PBN heaters have outstanding properties including high thermal conductivity and uniformity. The whisker is held by a soft Ta foil against a thin Ta plate that stays in direct contact with the PBN heater. One piece of the foil is sufficient to hold the whisker, which is beneficial for allowing free expansion during annealing. The JEOL sample holder is supplied with an approximate calibration that was later adjusted by means of an optical pyrometer (IRC IR-CA P2CS) focused on the Ta plate supporting the whisker. The temperature dependence on the heater current is shown in Figure 4.3c. The right electrode of the holder provides also a direct electrical contact to the sample, which can be used e.g. to apply a bias voltage during an AFM measurement (see Figure 4.3b).

4.1.2 Preparation chamber

The preparation chamber provides a number of tools, which are briefly described as follows:

Scannable ion gun (SPECS IQE 12/38) An extractor type, differentially pumped ion source produces a focused, scannable ion beam of high current density. It operates with a filament and ionizes the Ar gas by electron bombardment. The Ar gas is supplied to the ion gun by a high-precision leak valve. Although the manufacturer guarantees a spot size as small as 160 μm, the typical size used here is around 1,000 μm due to operation at a larger-than-optimal working distance.

Knudsen effusion cells (Kentax TCE-BSC) A UHV evaporator with 3 independent and separately controllable effusion cells suited to the evaporation of materials at temperatures as high as 700°C. This thermal evaporator is used to deposit Mg and NaCl onto Fe(001) surfaces at various rates, as well as coverages ranging from the submonolayer regime to continuous films.

E-beam evaporator (Oxford Applied Research EGN4 with retarding grids) A water-cooled electron-beam evaporator that can be equipped with four sources of various materials. Each evaporant can be either a rod or contained within a

metal crucible (Ta, Mo or W). During operation a rod or a crucible is held at a high voltage, which extracts electrons from a nearby hot filament. The e-beam evaporator is used to deposit Au from a Mo crucible, which acts as a thermal evaporator due to bombardment by electrons. The temperature of the crucible and the deposition rate can be controlled by the current flowing though one of four filaments assigned to each of the sources. Section 6.1.1 describes an attempt to use the e-beam evaporator to deposit MgO both from a rod and a crucible.

Quartz microbalance (Inficon BK-A0) A thin film quartz crystal deposition monitor is used to characterize deposition rates and coverages. In the case of reactive growth the MgO coverage is deduced from a rescaled value calculated from the density difference between the films of Mg and MgO.

Variable leak valves (DUNIWAY VLVE 1000 and MDC ULV) The admission of gases into the UHV system (Ar for sputtering, and O_2 for reactive growth) is controlled by precision UHV leak valves that allow for adjusting leak rates down to a minimum of 1×10^{-10} Torr·L/sec.

LEED/AES (SPECS ErLEED 150) A four-grid LEED optics with a hemispherical rear view glass screen coated with phosphorus is used to record LEED images. Although the spot size of the electron beam is less then 1 mm and is larger than the width of used whiskers, the LEED technique is still applicable for surface characterization of such small crystals. If the beam is centrally positioned, the LEED pattern and the information obtained about the surface originates from areas with a diameter smaller than the coherence radius of the electron beam, which for conventional LEED systems is about 10 nm (see Section 3.2.1). The limited size of the crystal can reduce the intensity of the LEED pattern, however LEED patterns recorded on clean Fe(001) surfaces in this work (see e.g. Figure 5.4) show excellent quality, demonstrating that this effect of the spot size can be neglected. The four-grid LEED optics can work as a retarding field analyzer (RFA) and perform Auger electron spectroscopy (AES) measurements. However, the small size of Fe whiskers makes them incompatible with the AES feature of the LEED optics, especially because the spot size increases at the higher electron energies used in AES (3 keV). In such a case, the chemical information about the surface will also originate from the Ta plate supporting the whisker that contributes to the AES signal. Although the LEED device is a characterization tool, it was installed in

the preparation chamber. Appendix B shows a major repair of the LEED optics carried out by the author as a consequence of extensive contamination with evaporated metals during previous research projects in the JEOL system, which is an example of how costly such compromises can be.

The pressure in the preparation and the microscope chamber is measured by hot-filament ionization gauges (Anelva NIG-2F head with JEOL AP-83030 controller). During research on samples consisting of NaCl films, the gauge is turned off at all times when the sample might be in direct view of the gauge, which could otherwise potentially cause electron induced desorption from the NaCl film. The preparation chamber also has a crystal cleaving station available, which was not used in the course of this work.

4.1.3 Microscope chamber

The microscope chamber is used for AFM characterization, and occasionally scanning electron microscopy (SEM) imaging *in-situ*. The AFM stage is shown in Figure 4.4a. Both sample (see Figure 4.3a) and cantilever (see Figure 4.4c) holders can be transferred between the magnetic transfer arm that extends from the preparation chamber and the stage by means of an internal manipulator. A special grabbing mechanism consists of an electromagnetically actuated pin that mates with the hole on the top of the tip or the sample holder. The manipulator can securely position both types of holders on their dedicated positions on the AFM stage. The JEOL microscope offers a rare possibility for simultaneous SEM and AFM measurements. Due to space restriction, the SEM column is installed at 45° off-normal angle with respect to the sample. As shown in Figure 4.4b the SEM looks down from the side at the sample and the tip. The microscope stage can be cooled by two flexible silver foils that are connected to a cryostat, which consists of two dewars: an outer liquid nitrogen (LN_2) dewar, and an inner dewar that can be filled either with LN_2 or liquid helium (LHe). This allows for reducing sample temperature down to $\sim$100K and $\sim$30K, when working with LN_2 and LHe respectively. Given the interaction between electrons and insulating films, such as MgO and NaCl, the SEM was used only sporadically in the course of this work. Similarly, the low-temperature feature of the AFM microscope was used occasionally

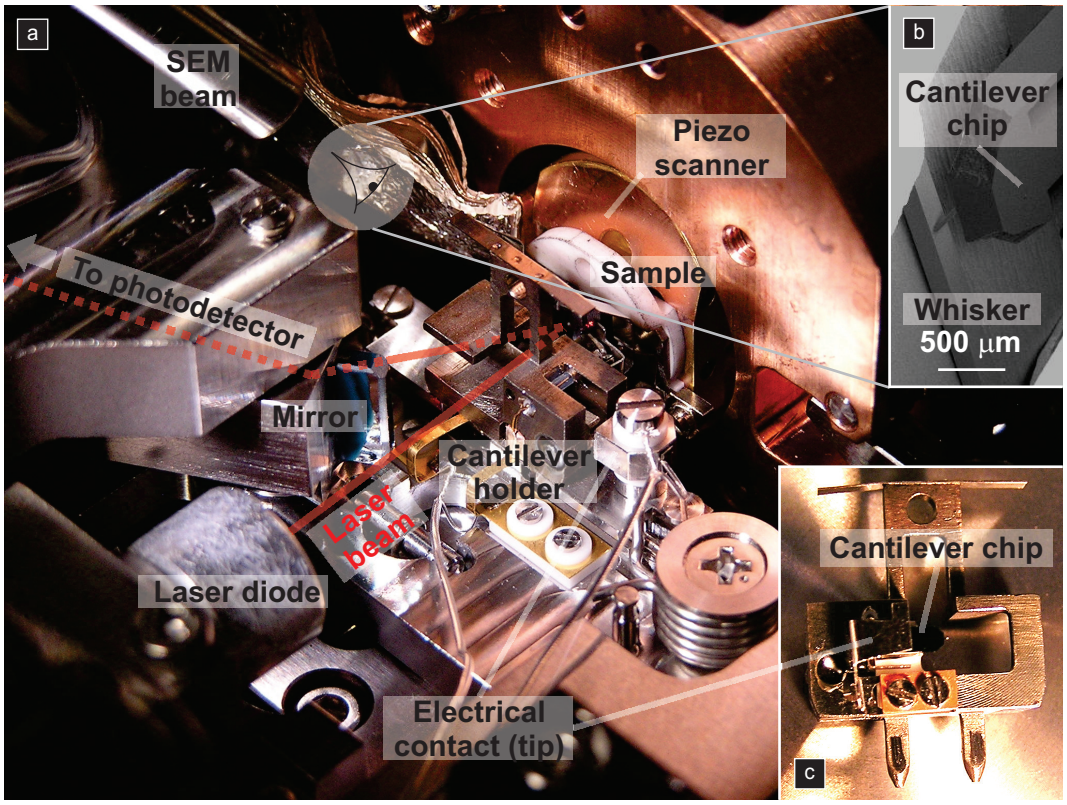

Figure 4.4: (a) The AFM stage of the JEOL microscope showing relevant components and the optical path of the laser beam. (b) An SEM image showing the sample (iron whisker) and the cantilever. (c) The AFM cantilever holder. A bias voltage can be applied to the tip through the electrical contact on the left side of the cantilever holder. The cantilever can be mechanically excited using a build-in piezo shaker by applying voltage through one of the ″legs″.

due to intrinsic limitations of such a cold-finger design. With the sample being one of the coldest elements in the system, the characterized surface remains clean only for a very short time because the sample acts as a cryogenic pump.

The AFM stage provides maximum three electrical connections to the sample holder, which are used to bias the sample during AFM measurements, but can be also used for on-stage annealing if the sample holder with an integrated heater is used (see Section 4.1.1). The sample holder is held by two side springs on top of a piezo tube that can extend 5μm in x and y directions, and 1.4 μm in the z direction at room temperature. The piezo tube is used for scanning, fine positioning and, together with coarse positioning, for approach. The coarse positioning involves a series of gears, fine-thread screws and lever arms inside the UHV system, which are magnetically coupled to external motors by rotary feedthroughs. The AFM stage provides also two electrical connections to the cantilever holder: one for applying bias voltage to the tip (see Figure 4.4, panels a and c), and a second through one of the "legs" that is used to apply voltage to a build-in piezo shaker that can mechanically excite the cantilever.

The JEOL AFM uses an optical beam deflection system. A red laser beam is generated inside the UHV chamber by a Hitachi HL6714G laser diode and focused onto the cantilever by a single lens. The diode is driven at constant current by an ultra-low noise controller (Thorlabs LDC 201C). In order to improve the stability and limit the interference inside the diode with any reflected light coming back to it, the DC laser bias is modulated using a radio frequency modulator. This approach, commonly used in CD, DVD or Blu-ray Disk players, reduces the coherence length of the laser beam and thus interference issues [79, 80]. Similarly to the coarse approach, the laser spot can be positioned by a set of gears and screws magnetically coupled to external knobs by rotary feedthroughs that move the laser diode. An analogue system is used to center the reflected laser spot onto the detector, which is a quadrant photodiode, by moving a mirror that deflects the laser beam in the horizontal direction and the detector itself in the vertical direction. The quadrant photodiode reads out four signals that are used to extract the cantilever deflection in the normal (called A$-$B) and the lateral (called C$-$D) directions.

In June 2012 the microscope chamber was upgraded with a sample storage system allowing for storing three sample holders. The JEOL system originally did

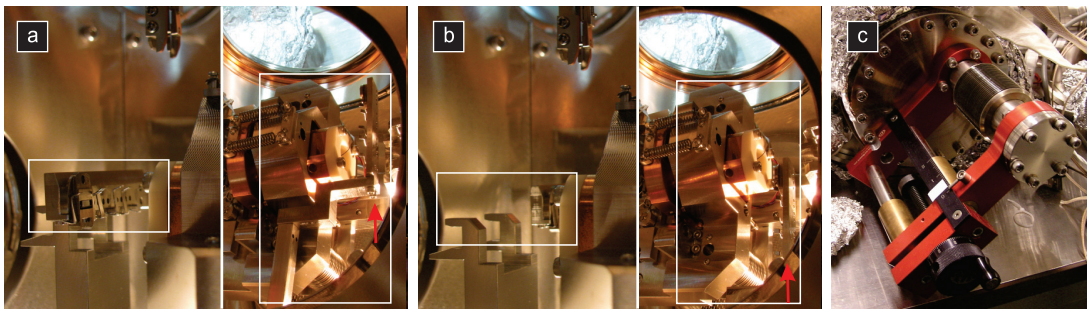

Figure 4.5: A retractable sample storage system allowing for storing three sample holders in the microscope chamber away from potentially contaminating processes. (a) The storage is in a position accessible for the internal manipulator. (b) Retracted position in which sample and tip holders can be transfered between the preparation chamber and the microscope stage. (c) The retraction mechanism (air side).

not have any designated storage system, except vacant positions in the preparation chamber. However, this solution was severely limiting due to potentially contaminating processes that take place in the preparation chamber. Figure 4.5 shows the retractable storage system, which extended the functionality of the JEOL system by allowing for parallel research projects and storing calibration samples.

4.2 NC-AFM operation

In the course of this work two control systems were used. The measurements presented in Chapters 6 and 7 were recorded using the original JEOL data acquisition system together with a Nanosurf easy PLL oscillation controller and frequency detector. A major change took place in June 2012, when the entire JEOL control system, except high-voltage (HV) amplifiers and the read-out of the optical beam deflection system, was upgraded with the Nanonis SPM control system [1]. The new Nanonis controller, compared to the old JEOL system, provides improved functionality that led to a successful characterization of single-electron charging, which is the topic of Chapter 8.

In general, the FM NC-AFM technique relies on the response of a high quality mechanical oscillator to a tip-sample interaction. The AFM cantilever can be

1. Modifications were made by Dr. Yoichi Miyahara.

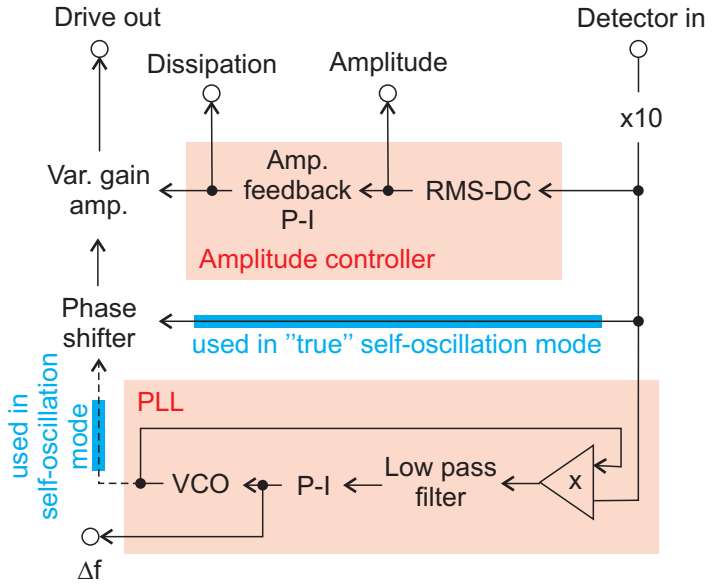

Figure 4.6: Diagram of the self-oscillation loop for FM NC-AFM exemplified by the Nanosurf system based on analog architecture. Both Nanonis and Nanosurf control systems can work in self-oscillation mode, where the self-excitation signal passes through the PLL, however only the Nanosurf controller can work in true self-oscillation mode.

regarded as a harmonic oscillator that is driven by a piezo shaker with its momentary displacement recorded using the A−B signal from the photodetector (see Figure 4.6). In the FM NC-AFM mode the cantilever is self-oscillated with a constant amplitude and the induced frequency shift is tracked using a phase-locked loop (PLL). The self-oscillation can be implemented in two ways. In the first case, the signal from the photodetector is phase shifted (which for a harmonic oscillator is typically $\pi/2$), amplified and used as the excitation signal. A feedback loop can be used to maintain the self-oscillation amplitude constant by adjusting the amplifier gain. Here, the PLL is demodulating the signal independently from the self-oscillation loop. In the second implementation, however, the PLL produces a reference signal whose phase is related to the input signal, which is used to excite the oscillator, by maintaining a constant phase delay of $\pi/2$ between the drive signal and the cantilever response. To distinguish between the two modes, the first mode that does not rely on the PLL is often called true self-oscillation mode. Both Nanonis and Nanosurf control systems can work in self-oscillation mode, where the self-excitation signal passes through the PLL, however only the Nanos-

urf controller can work in the true self-oscillation mode. The difference in the two modes can potentially have an effect on the stability of the cantilever oscillation under perturbing forces, such as voltage pulses used in Section 9.2.3 during field induced deposition from Au-coated AFM tips. The Nanosurf oscillation controller, in contrast to the Nanonis controller, is based on an analog architecture and uses a voltage controlled oscillator (VCO) to generate the reference signal in the PLL (see Figure 4.6). The Nanonis controller uses a digitized signal that is processed for demodulation by a digital PLL. Here, instead of a VCO, numerical oscillators generate sine and cosine signal pairs that are later mixed to generate a phase shifted signal used for both the demodulation and the generation of the output signal.

The frequency shift of the cantilever caused by the tip-sample interaction and measured by the PLL is maintained constant by a feedback loop controlling the z-piezo position. Scanning in x and y directions effectively generates maps of constant-Δf topography, which is called the "topography mode". Alternatively, the feedback loop of the SPM controller can be turned off or set to a very low value. In this case the SPM controller records a Δf map, which is called the "constant-height mode" and is useful for obtaining atomic resolution. More importantly, the *e*-EFM method relies on operation at constant height, which is required for proper qualitative and quantitative characterization of single-electron charging. The scan control platform of the JEOL control system did not allow for adjusting the tilt of the sample or compensating for the thermal drift, which left the *e*-EFM experiment outside the realm of possibility. The Nanonis SPM controller provides both sample slope and drift compensation that improves the stability of the tip height at room temperature, reducing its change to only a fraction of a nanometer over the time needed to scan one frame (approximately 15 mins).

The Nanonis controller is integrated with the LabVIEW programming interface, which can automate many measurements. In this way the experiment can be controlled in a practical and fast way. For instance, the oscillation amplitude is calibrated using an open-source script[2]. It uses the relationship between the Δf and the oscillation amplitude A, $\Delta f = bA^{-3/2}$, where b is some proportionality factor (see Section 3.1.1). During the calibration the controller changes the oscillation amplitude by a factor c to cA. In order to keep the tip-sample interaction constant,

2. Authors: S. Kawai, Ch. Held, Th. Glatzel, University of Basel, Switzerland.

the frequency shift set-point has to be readjusted to the new value derived for the changed amplitude cA, i.e. $\Delta f c^{-3/2}$. This is realized by the active feedback loop of the Nanonis controller that changes the z-position of the piezo scanner accordingly. By recording the required z-position change for various c parameters, it becomes possible to correlate the z-position to the expected amplitude value (cA) and obtain the calibration factor without knowing the value of the b parameter.

The FM KFPM characterization in Chapter 7 is performed with the use of an external lock-in (Princeton Applied Research, 5110 Lock-in Amplifier) and an additional feedback loop provided by the KFPM unit of the JEOL controller. The lock-in generates a modulation voltage typically with $f_{\text{mod}} = 800$ Hz frequency that is added to the tip or sample bias voltage by the JEOL controller. The bias voltage changes the tip-sample interaction, and in effect causes the frequency shift, Δf, to respond both at f_{mod} and $2f_{\text{mod}}$ (see Section 3.1.2). The modulation in Δf at f_{mod} is measured by the lock-in and used in the KFPM unit that adjusts the DC bias voltage to keep the amplitude of the modulation as small as possible. The filtered value of the DC bias voltage recorded above each surface point is read out by the JEOL controller to create a CPD map. To obtain higher sensitivity, the time constant of the lock-in is usually set to 3-10 ms and the time that the AFM tip spends per pixel while scanning is longer than this value.

For the experiments commercially available cantilevers manufactured by Nanosensors (Point Probe Plus (PPP) series) are used. The PPP cantilevers are made of doped Si and have the back side coated with Al to increase the reflectivity. For topography imaging usually PPP-NCLR cantilevers are used that have a typical resonance frequency of 160 kHz, and a nominal spring constant of 48 N/m (see Table 4.1 for nominal parameters specified by the manufacturer). The Q-factors of those cantilevers are typically 6-14,000 when measured in vacuum at room temperature. To obtain sufficiently high sensitivity, the *e*-EFM technique requires high Q-factors and operation at small oscillation amplitudes. For this reason, special QNCHR cantilevers are also used that are shorter and are characterized by higher Q-factors of approximately 30,000. The shortened beam has a direct effect on the minimal oscillation amplitude at which the self-oscillation is still stable, because in the optical beam deflection system the same angular deflection of a shorter cantilever corresponds to a smaller linear displacement of the tip.

PPP-NCLR

Shape	Length	Width	Thickness	Force const.	Res. freq.	Q-factor*
Beam	225 μm	38 μm	7 μm	48 N/m	190 kHz	6-14,000

PPP-QNCHR

Shape	Length	Width	Thickness	Force const.	Res. freq.	Q-factor*
Beam	125 μm	30 μm	4 μm	42 N/m	330 kHz	20,000-40,000

Table 4.1: Nominal parameters of the cantilevers used. The manufacturer (Nanosensors) estimates the resonance frequency based on the geometry of the beam, and the frequencies observed experimentally were approximately 15% lower. (*) The quoted Q-factor ranges correspond to typical values observed experimentally.

5

Preparation of Fe(001) substrates

The ultra-thin insulating films investigated in this thesis are grown on a (001)-oriented surface of a single crystal Fe. Below 911°C at ambient pressure pure Fe has a stable *bcc* structure [81], called αFe, with a lattice parameter of 2.870 Å. Consequently, the (001)-oriented surface exposes atoms arranged into a square lattice with the same distance between closest neighbors as the lattice parameter of αFe. The Fe(001) surface is known to be a very good support for growing crystalline ultra-thin MgO films in a near perfect layer-by-layer mode (see Section 2.1.2). However, preparation of clean Fe surfaces remains an experimental challenge, as commercially available crystals (usually with 99.99% purity) have a significant quantity of contaminants. These include carbon and nitrogen that are especially difficult to deplete [82]. Bulk Fe single crystals require tedious preparation methods to obtain clean and large atomic terraces. One example was reported by Parihar *et al.*, who were able to produce the Fe(001) surface with a width of some terraces approaching 500 nm after several weeks of preparation [83]. Other works similarly quote annealing times longer than 1,000 hours as necessary for sufficient decarburization of samples that are a few millimetres thick [84]. Given those difficulties, the majority of studies dealing with the Fe(001) surface use Fe thin films evaporated *in-situ* onto bulk MgO(001) [85] or GaAs(001) [86] single crystals. Such films can be easily prepared, but are characterized by a high amount of defects, especially screw dislocations.

The gold standard in research on Fe(001) surfaces are still whisker crystals, which attracted significant attention in 1950s due to their unusual strength. Whiskers are small filament crystals with widths ranging between a few to 500 μm, and lengths of up to a few millimeters. Because it becomes possible to obtain a defect-free sample at such small sizes, whiskers can reach a tensile strength greater

than 13 GPa [87]. For decades, whiskers had been considered the strongest materials in nature until the discovery of carbon nanotubes [88].

5.1 Growth of Fe whiskers

Iron whiskers can be grown by the hydrogen reduction of metal halides leading to very pure material, and thus avoids the necessity for tedious removal of contaminants. Among different salts ferrous chloride ($FeCl_2$) produces the best yield and quality [89, 90]:

$$FeCl_2 + H_2 \rightarrow Fe + 2HCl. \tag{5.1}$$

A schematic diagram of the apparatus used for the growth is shown in Figure 5.1a. An iron boat partially filled with $FeCl_2$ powder is placed in a quartz tube that in closed inside a three-zone horizontal Lindberg furnace (see Figure 5.1b). Both ends of the tube are terminated with flanges allowing for attachment of gas lines: an ultra-high purity (99.999%) H_2 or Ar gas inlet, and an exhaust that removes mostly HCl from the reaction chamber. Two thermocouples are placed outside the tube in close proximity to the front and the end of the boat in order to control the temperature of the boat. At temperatures around 680-720°C the reduction of $FeCl_2$ powder speeds up. Growth of Fe whiskers is a very inefficient process that is quite sensitive to the conditions under which the reduction takes place. Those include temperature, H_2 flow rate, size of the quartz tube and the boat, the amount of $FeCl_2$ powder, and any turbulences in the gas flow. More importantly, it was found in this work that the form and the quality of the $FeCl_2$ powder, and the preparation of the Fe boat are the major parameters controlling the growth of whiskers. $FeCl_2$ is commercially available in various forms, including an anhydrous form, as $FeCl_2$, and a hydrated form, as $FeCl_2 \cdot xH_2O$ (with $x = 2$, 4 or unspecified). The presence of water has a huge consequence on the phase transition of the powder at high temperatures. Anhydrous $FeCl_2$ melts at a temperature of 670-674°C, while hydrated $FeCl_2$ can directly sublimate into a gas phase [91]. There is a significant cost difference between commercially available anhydrous and hydrated $FeCl_2$ powders, in favour of the latter. However, there are two disadvantages of

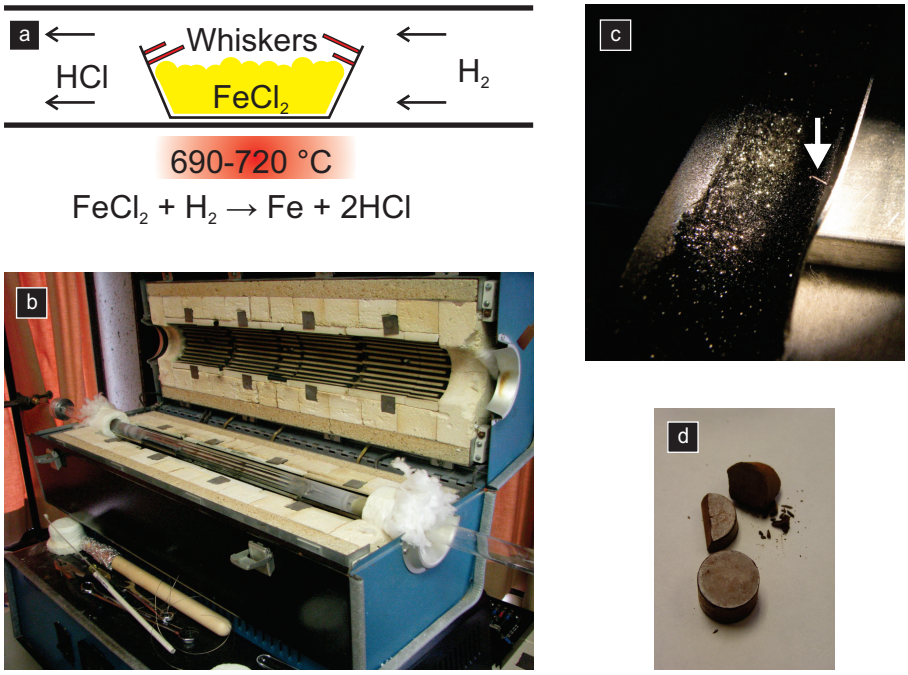

Figure 5.1: (a) A schematic diagram of the apparatus used to grow Fe whiskers. (b) The Fe boat with $FeCl_2$ powder is annealed in a H_2 gas inside a three-zone horizontal LINDBERG furnace. (c) Iron whiskers usually grow from the internal sides of the boat in a narrow band just above the sublimating $FeCl_2$ powder. (d) The surface area of the powder can be made smaller to slow down the reaction with H_2 by creating pellets using a pneumatic pellet press.

using the hydrated powder. First, when the temperature inside the furnace is increased, the powder is gradually dehydrated and water vapour is released that can oxidize the Fe boat. Second, the partially anhydrous $FeCl_2$ powder becomes very porous and reacts very quickly with H_2 when the temperature activating the reaction is reached. Consequently, during the reaction a significant part of the $FeCl_2$ powder is reduced to Fe in the form of small particles or a continuous layer on the bottom and sides of the boat, which does not contribute to whisker growth.

In general, if whiskers are formed during the reaction, they grow from the internal sides of the boat in a narrow band just above the sublimating $FeCl_2$ powder (see Figure 5.1c). This sets a requirement for the boat to be as large as possible, because there has to remain an exposed surface of the Fe boat, where the growth is initiated. Additionally, the boat should be large in order to accommodate a sufficient amount of the powder, as greater quantities produce larger whiskers, both in diameter and length.

The process of growing whiskers starts from cleaning a tempered Fe foil of 0.25 mm thickness, and 99.5% purity (GoodFellow) using sandpaper (grid No. 240) and acetone. The foil is annealed at 750°C in H_2 for several hours, which efficiently removes carbon and oxygen from the surface. A hydrate $FeCl_2$ powder (Alfa Aesar, Reagent Grade, 99%) is separately dehydrated in Ar gas for 1-2 days. It has to be emphasized that full dehydration of the powder is impossible using this technique. In order to slow down the later reaction with H_2 the surface area of the powder can be made smaller by creating pellets using a pneumatic pellet press. Such pellets, which are shown in Figure 5.1d, can be subsequently crumbled into small pieces of desired size of 2-3 mm. About 10 g of a dehydrated $FeCl_2$ material is placed inside the Fe boat and the boat is positioned between two furnace zones inside the quartz tube. In this way a gradient between the two ends of the boat can be created. This leads to slightly different temperature conditions that change along the boat, which maximizes the probability for efficient growth of whiskers. The system is carefully purged with H_2 before starting the furnace. The furnace temperature is raised by 100°C every 30 mins until the desired setpoint is reached.

The best results are obtained at temperatures of 690°C (front of the boat) and 720°C (back of the boat), and 40-50 ccm flow of H_2 (with 59 mm quartz tube diameter). The optimal parameters can be coarsely determined in the following

way. If the gas flow is too slow, the concentration of H_2 changes along the reaction zone and at some point is not sufficient to fully reduce the $FeCl_2$ powder. Consequently its vapor is transported with the HCl product away from the hot reaction zone and condenses in colder areas. In such a case there is a large build-up of condensed $FeCl_2$ inside the quartz tube. If the gas flow is too fast, the $FeCl_2$ vapor can be swept away from the primary reaction zone. Too low temperature will not vaporize $FeCl_2$ and the reduction will undergo with solid $FeCl_2$ in the boat. In contrast, too high temperature can increase the vapor pressure inside the quartz tube so much that the vapor can reach colder places inside the tube where it will condense and undergo the reaction to metallic Fe. The major difficulty in growing whiskers is that the results can be only observed after the reaction is finished, and the system is cooled down and opened. This limitation slows down any optimization process making growth very tedious.

Under optimal growth conditions, 10 g of $FeCl_2$ is fully reduced after several hours. Next, the furnace is turned off and allowed to cool down. Whiskers grown by the hydrogen reduction of $FeCl_2$ are often clustered and seem to grow from a common base. They also vary in shapes and crystallographic orientations. Most whiskers have a rectangular cross-section indicating that their axes is oriented along the $\langle 011 \rangle$ direction [89] (see Figure 5.2a). Such whiskers have $\{100\}$ and $\{011\}$-oriented side surfaces. The second most dominant group of whiskers have a square cross-section, which are used in this thesis. The regular shape and high reflectivity of side surfaces suggest that axes of such whiskers are oriented along the $\langle 100 \rangle$ direction and the side surfaces have $\{001\}$ orientation. The exact orientation and crystallographic quality of grown whiskers was evaluated by means of XRD that measures the angular position and the width of Bragg peaks.

A triple-crystal X-ray diffractometer built in the group of Prof. Mark Sutton in the Physics Department at McGill University, which is shown in Figure 5.2b, was used to verify the orientation of whiskers. It confirmed that four sided and square in cross-section whiskers are single crystals, their long axis is oriented along the $\langle 100 \rangle$ direction and the four sides have a $\{100\}$ termination. Two Fe whiskers of different sizes (50 μm and 200 μm) were characterized in detail by recording high-resolution scans of their (011) and (002) Bragg peaks. As an example, the (002) Bragg peak in the reciprocal space of the 200 μm wide whisker is shown in Fig-

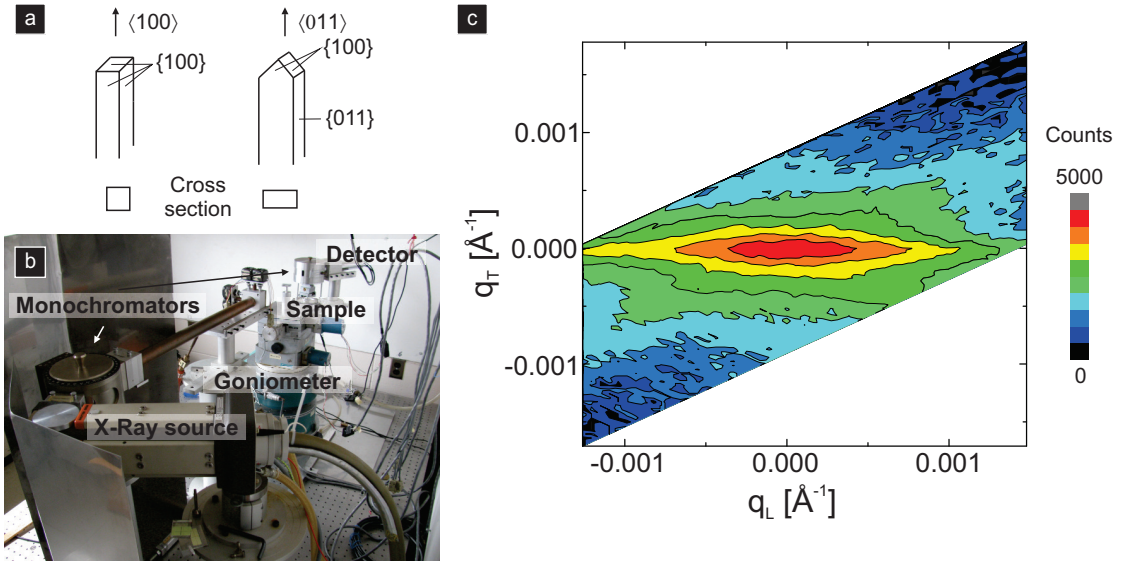

Figure 5.2: (a) Two most dominant types of whiskers produced during the growth. (b) A triple-crystal X-Ray diffractometer used to verify the orientation and quality of whiskers. (c) The (002) Bragg peak in the reciprocal space of a 200 μm wide whisker (as isointensity contours of logarithmic values).

ure 5.2c (as isointensity contours of logarithmic values). The shape of the Fe(002) peak represents a crystal of a very high quality. Indeed, the shape of the isointensity contours looks like a butterfly, which is typical for high-resolution diffraction experiments in a triple-crystal reflection geometry. The two additional streaks are due to weak diffuse scattering from monochromator and analyzer crystals, which means that Figure 5.2c illustrates almost the resolution of the diffractometer. Such a sharp Bragg peak corresponds to a very low density of crystallographic defects in the grown whiskers characterized by the average separation between lattice defects in the order of a few micrometers. The Bragg angle of the Fe(002) peak for this sample was measured to be 32.513°, which leads to a lattice constant of 2.8661 Å. This is close to values quoted in literature (2.8665 Å) and the small difference may be attributed to thermal expansion. The X-ray diffraction could not reveal any substantial differences in the quality of smaller and larger in width whiskers.

A brief comment should be made on the growth mechanisms of Fe whiskers. Iron whiskers grow from their tip, and vapor transport is most probable source of iron. The initial hypothesis [92] used screw dislocation theory and assumed that

$FeCl_2$ is already reduced when it condenses on the growing whisker. In this theory a crystal can grow by extending atomic terraces where new material nucleates. A screw dislocation guarantees that there is always an available site for nucleation, which lowers the requirement for supersaturation (much higher supersaturation is required for a direct two dimensional condensation of metal vapor). However, experimental results could not demonstrate the presence of screw dislocations in Fe whiskers [93]. Alternatively, growth could be occurring by the vapor-liquid-solid (VLS) mechanism [94]. In this scenario the $FeCl_2$ molecules are adsorbed on the growing whiskers and reduced at the tip where a liquid droplet is formed. The surface tension of the liquid droplet increases the pressure inside it and the liquid material becomes supersaturated with the crystal material. The growth results form the condensation of this material at the liquid-solid interface and does not require a screw dislocation. In the VLS growth mechanism the length of the whisker is extended by the growth at the tip of the whisker and the thickness of the whisker is slowly increased from base to tip. Webb et al. [95] proposed that $FeCl_2$ vapor can diffuse to the whisker side surface where it is reduced and next metallic Fe diffuses to a growth site. Based on thermodynamical considerations they have also concluded that hydrogen reduction in gas phase followed by the nucleation of metallic Fe cannot explain whisker growth rates observed experimentally making the VLS mechanism a more likely scenario.

5.2 The Fe(001) surface

Whiskers with a square cross-section that have $\{001\}$-oriented side surfaces were used as Fe(001) substrates. An as-grown whisker is loaded into vacuum chamber without additional cleaning and baked out overnight at 120°C to desorb water from the entire sample holder. The sample is next sputtered by 1 keV Ar^+ beam at an incident angle 60° off-normal. Initially the sample is kept at room temperature, and later the temperature is ramped up to about 600°C. The duration of sputtering varies from 30 mins to several hours, where more intensive sputtering is required in the early stages of the cleaning process and during removal of deposited insulating ultra-thin films. The preparation of the sample is finished by annealing at about 600°C for 15 mins.

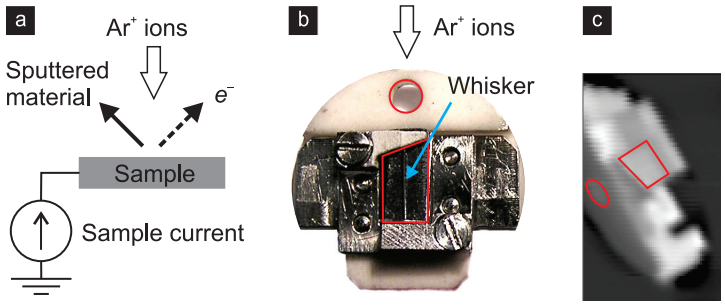

Figure 5.3: (a) During sputtering the current between the sample and ground provides information on the material and can be used for imaging that is similar to ion-excited secondary electron microscopy. (b) and (c) A photograph and an "ion" image of the sample holder formed during scanning the sample with a focused Ar^+ beam (the red marks are added to guide the eye).

In order to facilitate the cleaning process and shorten the sputtering time, the scanning capability of the ion gun (SPECS IQE 12/38) is used. The ion beam can be focused to a spot size smaller than 1 mm, which allows for imaging that is similar to ion-excited secondary electron microscopy. As the beam is rastered over the sample, it will not only sputter the material, which leaves the sample as neutral or positively charged, but also cause an ejection of electrons. The intensity of those processes depends on the material, and a simple measurement of the current between the sample and ground during sputtering (see Figure 5.3a) provides information about the material. The total current due to the incident Ar^+ beam, the sputtered material and secondary electrons is analyzed to produce images of the sample (see Figure 5.3, panels b and c). A LabView script can read out the signals monitoring the x and y deflections provided by the ion gun controller and create a 2D map of the current (typically in the range of 50 nA $-$ 3 μA). In Figure 5.3c one can clearly identify the position of the whisker, and limit the sputtered area to the relevant part of the sample holder. In this way, the average current density can be significantly increased, reducing the required sputtering time.

The sputtering-annealing cycles are repeated until a clean LEED pattern is observed, as shown in Figure 5.4a. NC-AFM imaging reveals that the surface is composed of atomically flat terraces of typical size exceeding 100 nm, and locally up to 500 nm (see Figure 5.4b).

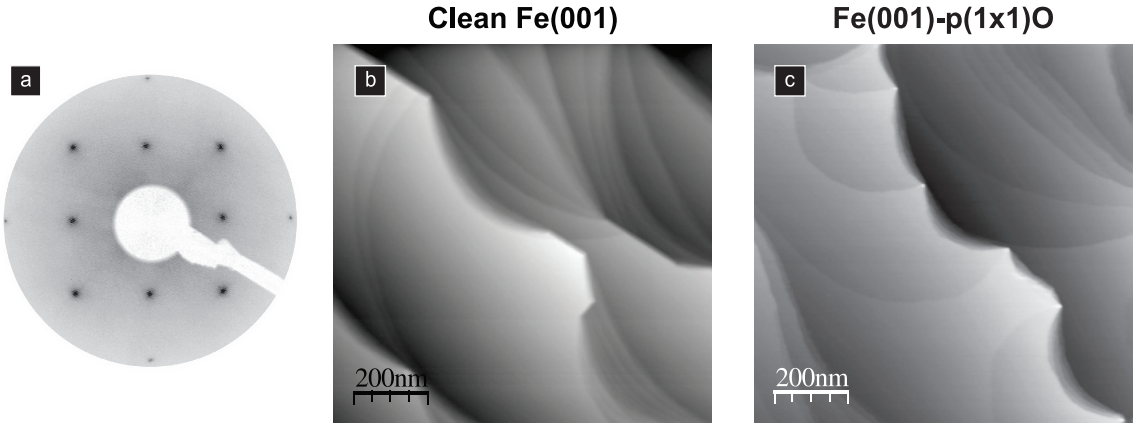

Figure 5.4: (a) A clean LEED pattern recorded on a Fe(001) surface. (b) NC-AFM image of the surface showing atomically flat terraces exceeding 100 nm width. (c) NC-AFM image of the Fe(001)-p(1×1)O surface. Panels (a) and (b) are part of Chapter 6 based on [Tekiel, A.; Fostner, S.; Topple, J.; Miyahara, Y.; Grütter, P. Reactive growth of MgO overlayers on Fe(001) surfaces studied by low-energy electron diffraction and atomic force microscopy. *Appl. Surf. Sci.* **2013**, *273*, 247-252 © 2013 by Elsevier B.V.]

5.3 The Fe(001)-p(1×1)O surface

The chemical and elastic properties of the Fe(001) surface can be easily modified by terminating the surface with chemisorbed oxygen atoms. Exposure to several Langmuir of molecular oxygen followed by flash annealing leads to the well-known Fe(001)-p(1×1)O surface, which has been thoroughly investigated by experimental and computational methods [83, 96]. The surface is characterized by one oxygen atom per unit cell chemisorbed in each hollow site of the Fe(001) surface. The new lattice parameter is the same as the parameter of the Fe(001) surface. As will be discussed in this thesis, the chemisorbed oxygen layer plays an important role in the growth of insulating films on the Fe(001) surface. The top layer of the Fe(001)-p(1×1)O surface resembles a planar *rock-salt* FeO monolayer. Compared to clean bulk Fe, *rock-salt* FeO has better elastic properties and the Fe(001)-p(1×1)O surface acts as a strain buffer in the epitaxy of ultra-thin films on top of it [97]. Moreover, the oxygen layer likely prevents the Fe(001) surface from the reaction with NaCl. Higher chemical stability allows for using elevated temperatures during sample preparation to enhance the diffusion of NaCl and improve the film quality.

5.4 Conclusions

Although growth of Fe whiskers is characterized by a limited yield, it produces small quantities of filament crystals that have very high quality. The cross-section of as-grown whiskers can reveal their orientation, where a square cross-section indicates that the side surfaces belong to the $\{001\}$ family, which can be confirmed either by XRD or LEED. Such crystals can be processed in ultra-high vacuum by sputtering and annealing cycles to produce a clean and well-ordered Fe(001) surface. By exposing the Fe(001) surface to molecular oxygen and post-annealing it a Fe(001)-p(1×1)O surface is formed that has the same lattice, but differs in chemical and elastic properties. The following three chapters will present results that use large atomic terraces of the Fe(001) or Fe(001)-p(1×1)O surfaces of a whisker to grow MgO or NaCl films. A single whisker can be easily reused by removing the deposited ultra-thin film by sputtering. To produce all results presented in this thesis only one whisker was used that was sputtered-annealed in total 166 times.

6

Reactive growth of MgO films on Fe(001) surfaces

THIS CHAPTER IS BASED ON:

Tekiel, A.; Fostner, S.; Topple, J.; Miyahara, Y.; Grütter, P.

Reactive growth of MgO overlayers on Fe(001) surfaces studied by low-energy electron diffraction and atomic force microscopy

Appl. Surf. Sci. **2013**, *273*, 247-252 © 2013 by Elsevier B.V.

This chapter describes preparation of ultra-thin MgO films grown reactively on the Fe(001) surface by evaporation of magnesium in an atmosphere of molecular oxygen. The insulating films have been investigated by LEED and NC-AFM. Preparation of structurally stable crystalline films requires a protocol that prevents an excessive interfacial reaction between oxygen and the Fe(001) surface, but at the same time provides a sufficient amount of oxygen in order to grow a stoichiometric MgO film. The proper ratio between the magnesium deposition rate and the oxygen pressure has been determined in this work, as well as measures to prevent initial interfacial oxidation of the substrate. The effect of both post-annealing and an increased substrate temperature during the growth has been studied. We demonstrate that the reactive deposition method, which gives full control over the gaseous species that reach the surface, can produce terraces that have an average size of 10 nm (on an 8 monolayer thick film), which is a significant improvement (factor of 2) compared to other preparation methods, such as thermal or electron beam evaporation of MgO.

6.1 Introduction

Crystalline magnesium oxide films grown on a variety of metal substrates, such as Ag(001), Mo(001) and Fe(001), play important roles in magnetoelectronics [5] and as model systems for studying catalysis [6]. Ultra-thin MgO films that serve as a tunneling barrier have been identified as a promising building block of MTJs. In the case of Fe(001)/MgO/Fe(001) MTJs, crystalline MgO leads to a high TMR ratio [30, 56]. The quality of the MgO interface is crucial for high TMR, and thus for more than a decade there has been growing interest in improving the quality of MgO films on the Fe(001) surface, in order to further increase the TMR to much higher values predicted theoretically [98, 99]. However, even the best films are still characterized by a high number of defects, such as dense networks of misfit dislocations, and by very small terraces (understood as flat areas separated by atomic steps). The terraces of MgO films deposited at room temperature are only a few nanometers in width [29, 100] and are smaller than the separation between dislocations. So far, limited high-resolution SPM characterization of MgO films on Fe(001) prepared at elevated temperatures has been carried out [100] and consequently, it is still an open question how such a preparation method can improve their quality. Evaporation at higher sample temperatures and post-annealing have been beneficial for the quality of MgO films on Ag(001) leading to larger terraces [26]. Also in the case of MgO films on Mo(001), annealing reduces the density of step-like features formed due to dislocations [27].

6.1.1 UHV deposition methods of MgO

The reduction in quality of MgO films on Fe(001) surfaces can be attributed to the conventionally used preparation method and the fact that iron is very prone to oxidation. In a UHV environment, MgO films are usually deposited onto the Fe(001) surface by electron beam evaporation of a stoichiometric MgO target [29, 30] and the resulting beam is composed mainly of magnesium and oxygen, both in an atomic form [31]. However, on Ag(001) and Mo(001) surfaces MgO ultra-thin films with the best morphology have been obtained by the reactive deposition of Mg in an O_2 atmosphere, the rate and pressure of which can be independently controlled [26, 27]. Both methods are quite challenging experimentally, as in

either case MgO is essentially grown from two separate sources of magnesium and oxygen. As it was schematically shown in Figure 2.3, in this situation magnesium and oxygen must react on the substrate in order to nucleate MgO molecules (in the case of molecular oxygen, an O_2 molecule has first to dissociate on the surface). Next, MgO molecules diffuse and build MgO islands. There are three stages of such growth, each potentially requiring different growth parameters, as it is taking place on a dissimilar substrate: (i) growth of the 1st monolayer, (ii) growth of several consecutive layers under conditions perturbed by the metallic substrate and (iii) growth of bulk-like MgO. The reactive deposition method provides direct control of the relative exposure of the sample to magnesium and oxygen. For instance, this is exploited on the Ag(001) surface, where an overexposure of the surface to oxygen can be used to prevent an unwanted reaction between silver and magnesium [101]. Similarly, during the reactive growth of MgO on the Fe(001) surface, the amount of oxygen to which the iron surface is exposed can be precisely controlled. Although the formation of an FeO_x interface may reduce the TMR in MTJs [102, 103], the oxygen at the Fe/MgO interface can facilitate epitaxy of MgO ultra-thin films on Fe(001) [97]. The exposure to a very small amount of molecular oxygen (below 1 ML) does not change the substrate morphology drastically, as it leads to an immediate dissociation of oxygen molecules that preferentially absorb in fourfold hollow sites of the Fe(001) surface [104]. Based on STM characterization, Bonell *et al.* [105] suggested that at this coverage range the oxygen remains mobile on the surface. When approaching a full monolayer, oxygen atoms reveal a high degree of ordering leading eventually to a p(1×1)-O structure with each hollow site of the Fe(001) surface occupied by one oxygen atom. However, if this exposure is exceeded, poorly defined iron oxide islands of 2-3 ML thickness are formed [83], which will significantly disturb subsequent MgO growth. This means that during reactive growth there should exist a particular composition of the flux reaching the sample that will form a well-ordered MgO monolayer, even if the iron substrate has been in contact with oxygen and might have been partially oxidized. During the growth of the consecutive MgO layers, the amount of oxygen should be increased, as the iron substrate has been already covered and a higher oxygen concentration is required to grow a stoichiometric MgO film.

During initial experiments we attempted to grow MgO films on Fe(001) by

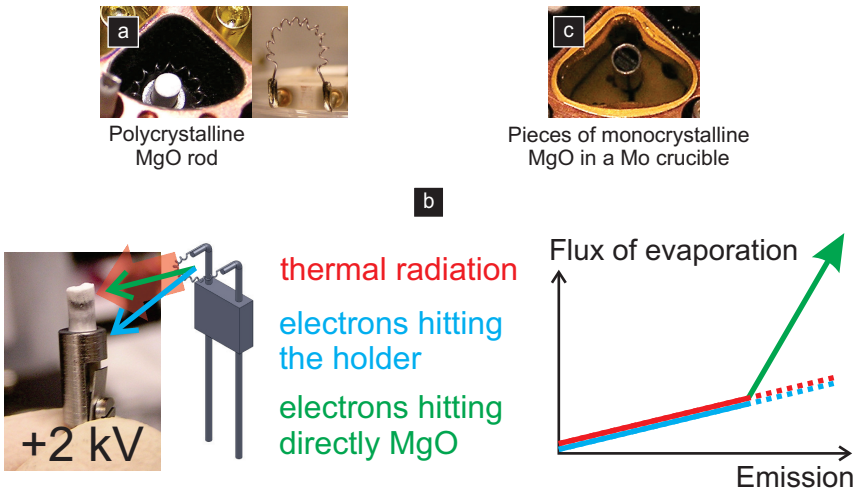

Figure 6.1: (a) Electron beam evaporation of MgO. A polycrystalline MgO rod supported by a Mo holder and a specially wound Ta filament. (b) When the emission of electrons is low, the electrons hit mostly the Mo holder and heat it up. In addition, the MgO rod is heated by the hot filament placed nearby. When the emission of electrons is high, the temperature of MgO increases, which reduces its resistivity and eliminates charging effects. (c) Thermal evaporation of monocrystalline MgO pieces placed inside a Mo crucible.

electron beam evaporation from a polycrystalline MgO rod, as this method led to the best quality of such films [29, 30]. Magnesium oxide is a good insulator, and the idea of the evaporation of an MgO rod using electrons [29] is explained in Figure 6.1, panels a and b. A polycrystalline MgO rod is supported by a holder made entirely of Mo, which is held at a high positive voltage. Next to the MgO rod, there is a specially wound filament that generates electrons. At low power, i.e. when the emission of electrons is low, the electrons hit mostly the Mo holder, where they dissipate their kinetic energy, heating up the holder and the MgO rod (marked by a blue arrow in Figure 6.1b). In addition, the hot filament itself contributes also to the temperature increase of the rod (marked by a red arrow in Figure 6.1b). When the emission of electrons is further increased, the high temperature of MgO reduces the resistivity of the rod [106] and eliminates charging effects. Starting at this point, the electrons directly hit the MgO rod, increasing significantly the flux of evaporation (marked by a green color in Figure 6.1b). In another attempt that is shown in Figure 6.1c, MgO was also thermally evaporated by placing pieces of monocrystalline MgO inside a Mo crucible. In this situation, the electrons hit

directly the metal crucible, heating it up to the evaporation temperature of MgO. Unfortunately, crystalline films could not be grown by either of these methods. This was partly caused by generation of oxygen during the evaporation, which poisons the hot filament. However, the major difficulty can be attributed to the issue discussed in Section 6.3.6, i.e. the construction of the e-beam evaporator can affect the composition of the evaporated fluxes. This difficulty is circumvented in the reactive deposition method, which provides direct control of the relative exposure of the sample to magnesium and oxygen.

To date, the reactive growth of MgO on Fe(001) has been studied only by high resolution electron energy loss spectroscopy [107], photoelectron spectroscopy [108, 109], and at 1 ML coverage by STM [110]. In this study we focus on the reactive growth method of 8-16 ML thick MgO films, which are characterized here both in real and reciprocal space. This thickness range is typically used in magnetic tunnel junctions [5] and in systems for studying model catalysis, where the MgO film supports metal nanoparticles [6]. In order for such a film to have high crystalline quality, the film must be successfully grown during all three steps mentioned above. The composition of the flux can be easily varied at the timescale needed to grow one MgO monolayer by controlling the gaseous species deposited, allowing for readjustment of parameters at each step of the growth process. We use LEED to determine the quality of MgO films grown from fluxes of different compositions and at various sample temperatures. Excessive oxidation of the Fe(001) substrate can be avoided by decreasing the oxygen pressure at the beginning of the growth or by the deposition of a submonolayer Mg prior to the reactive growth of MgO. Characterization by NC-AFM of an 8 ML thick film demonstrates that compared to deposition by electron beam evaporation of MgO, reactive growth can produce a better ordered surface with larger terraces.

6.2 Experimental details

All experiments reported here are performed in two interconnected UHV chambers (preparation and microscope) based on a commercial JEOL JSPM 4500a UHV AFM system. The base pressure is in the low 10^{-11} mbar range in the preparation, and 1×10^{-10} mbar in the microscope chamber. Iron whiskers home-grown

by reduction of $FeCl_2$ in an H_2 atmosphere with {001} side-surface orientations are used as the starting substrate [89] (see also Chapter 5). The whiskers are cleaned by several cycles of 1 keV Ar^+ sputtering and a subsequent annealing to about 600°C until a clean LEED pattern is observed. This procedure leads to a surface with terraces several hundred nanometers wide. A piece of magnesium (99.99% purity) is outgassed in vacuum and then evaporated from a Knudsen cell onto the Fe(001) sample kept at temperatures ranging from room temperature (RT) to 300°C in an atmosphere of molecular oxygen (99.997% purity), whose pressure is controlled by a high precision leak valve. The rate of magnesium deposition was monitored by quartz crystal microbalance and the MgO coverage was deduced from a rescaled value obtained from the density difference between the films of Mg and MgO. Long-range order of the evaporated layers is characterized by LEED performed at room temperature. Although electrons can cause desorption of oxygen from the MgO(001) surface, this effect is very small at low electron energies and has a threshold at 55 eV incident electron energy [111]. Also no time deterioration of LEED images recorded at 90-150 eV electron energy has been observed in this work. NC-AFM is also carried out at room temperature in the FM mode using JEOL AFM and Nanosurf "easyPLL"' frequency detector/oscillation controller in self-oscillation mode. Commercial Nanosensors PPP-NCLR silicon cantilevers with a typical resonance frequency of 150-160 kHz and spring constant of ≈42 N/m are used with a peak-to-peak oscillation amplitude of 10-14 nm. A constant bias voltage during NC-AFM imaging was applied to the sample to compensate long-range electrostatic forces.

6.3 Results and discussion

6.3.1 Effect of exposure of clean Fe(001) to O_2

After the sputter-cleaning procedure the Fe(001) surface was examined by LEED and NC-AFM (see Figure 6.2a). The LEED pattern reveals very clear (1×1) symmetry. The surface is composed of atomically flat terraces of typical size exceeding 100 nm, and locally up to 500 nm. If the clean Fe surface is exposed to 6 L (Langmuir, 1 L = 10^{-6} Torr·s) of O_2 at RT, there is almost no change in the quality of

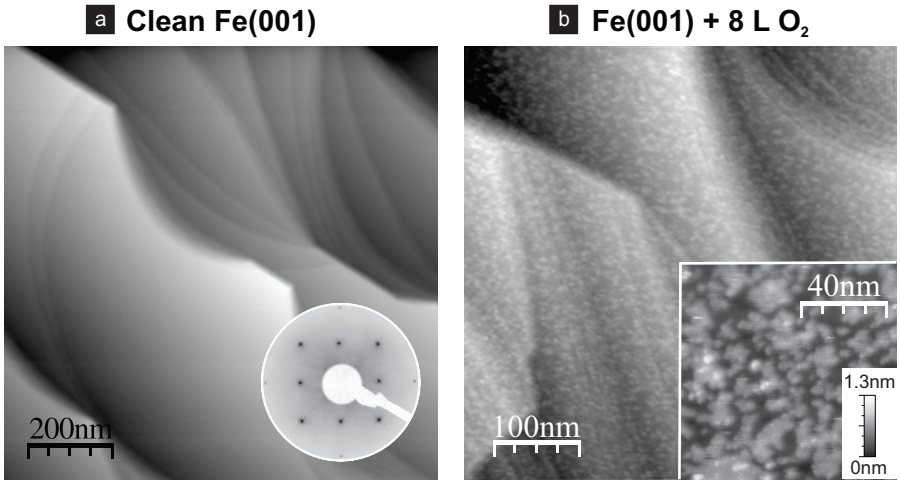

Figure 6.2: (a) A clean Fe(001) whisker surface: NC-AFM topographical image recorded at $\Delta f = -18$ Hz and sample bias 0 V, LEED pattern recorded at 141 eV electron energy. (b) The Fe(001) surface after the exposure to 8 L of O_2 showing formation of iron oxide islands (parameters of both frames: $\Delta f = -3$ Hz, sample bias 0.5 V).

the LEED pattern, and similarly the presence of oxygen is not directly evidenced by AFM, which can be related to mobile oxygen on the surface as suggested by Bonell *et al.* [105]. With an 8 L dose, the LEED pattern vanishes almost completely and the surface roughness increases due to formation of iron oxide islands. Such a morphology, which has been characterized by Parihar *et al.* using surface X-ray diffraction [83], is undesirable for subsequent growth of MgO. The fact that this unwanted morphology forms first at the dose of approximately 8 L can be used to estimate a lower limit for the deposition rate of Mg. For instance, at a pressure of 1.33×10^{-7} mbar (1×10^{-7} Torr), a dose of 8 L corresponds to an exposure duration of 60 s (at this pressure 1 ML of O_2 should form after about 4 s assuming sticking coefficient of 1 [14]). If during that time a sufficient amount of Mg atoms arrive at the surface to form the first MgO monolayer, the unwanted morphology shown in Figure 6.2b should not form. In other words, the time needed to form the first MgO monolayer should be shorter than the exposure time that is equivalent to 6-8 L at a given O_2 pressure. Usually magnesium is deposited at a rate of approximately 1 Å/min (0.38 ML/min) during the reactive growth on Ag(001) and Mo(001) surfaces. Assuming that $n_{\mathrm{Mg}}/n_{\mathrm{MgO}} \approx 1$, where n_{Mg} and n_{MgO} denote the number of Mg atoms per unit area in *hcp* Mg(0001) and *rock-salt* MgO(001) mono-

layers, respectively, formation of an MgO monolayer requires approximately 160 s, at shortest. This gives a rough estimation of 5×10^{-8} mbar for the maximum oxygen background pressure during the reactive growth at a Mg deposition rate of 1 Å/min.

6.3.2 Optimal Mg deposition rate and O_2 pressure

We next utilize LEED to investigate the effect of the Mg deposition rate and the background pressure of the oxygen atmosphere on the crystalline quality of MgO ultra-thin films on Fe(001). Figure 6.3 shows LEED patterns of 8 ML thick MgO samples grown at RT and prepared at O_2 pressures ranging from 1×10^{-8} to 6×10^{-7} mbar, and Mg deposition rates 1.0-3.6 Å/min, as suggested by the previous estimation. A series of samples grown at Mg deposition rates 1.3-1.5 Å/min indicates that the LEED patterns become sharper if the O_2 pressure is within a range of 5×10^{-8} and 5×10^{-7} mbar, confirming a well-ordered crystal structure and an epitaxial growth of the MgO film. Both for lower (1×10^{-8} mbar) and higher (5×10^{-7} mbar) O_2 pressures the LEED patterns start to fade away. For higher Mg deposition rates, this interval of optimal growth parameters is shifted towards higher O_2 pressures, and for lower Mg deposition rates, to lower O_2 pressures. Based on those observations, two regions of unfavorable growth parameters can be identified. The first region is related to the oxidation of the Fe(001) surface and occurs for higher pressures of O_2. The second region is characterized by a high rate of Mg deposition and an amount of oxygen that is insufficient to grow a stoichiometric MgO film. Thus, the crystal structure is optimized for a particular ratio $r/p = 0.15 \pm 0.05$ between the Mg deposition rate (r, expressed in Å/min) and the O_2 pressure (p, expressed in 10^{-8} mbar).

6.3.3 Effect of post-annealing observed by LEED

Although well-ordered films can be prepared by using constant Mg deposition rates and O_2 pressures, not all of such MgO films retain high quality after annealing. Such structural instability is most likely related to the balance between the oxidation of the substrate at the MgO/Fe interface and MgO film stoichiometry. This suggests that constant r and p parameters cannot fulfill simultaneously op-

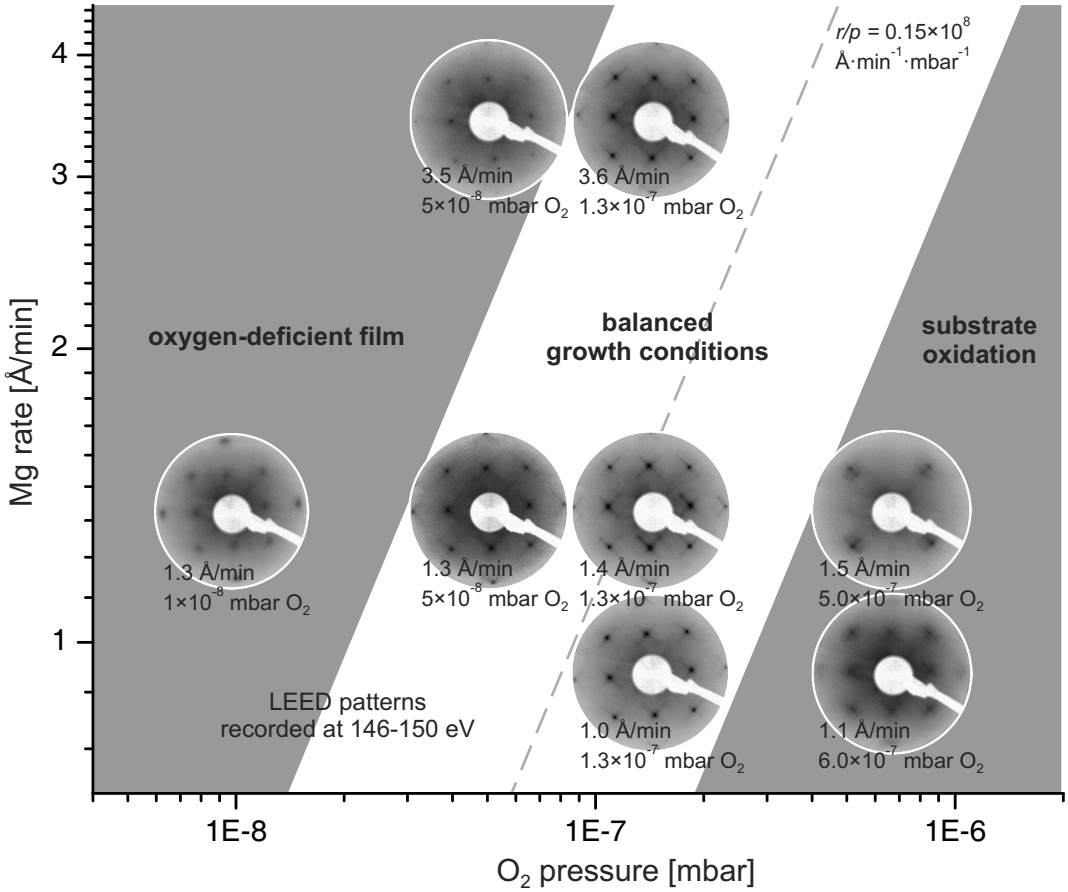

Figure 6.3: LEED patterns of 8 ML thick MgO samples grown at RT and prepared at various O_2 pressures and Mg deposition rates. MgO films reveal higher crystalline order for a particular ratio $r/p = (0.15 \pm 0.05) \times 10^8$ Å·min^{-1}·mbar^{-1} between the Mg deposition rate and the O_2 pressure. There are two regions of unfavorable growth parameters. The first region is related to the oxidation of the Fe(001) surface and occurs for higher pressures of O_2. The second region is characterized by a high rate of Mg deposition and an amount of oxygen that is insufficient to grow a stoichiometric MgO film.

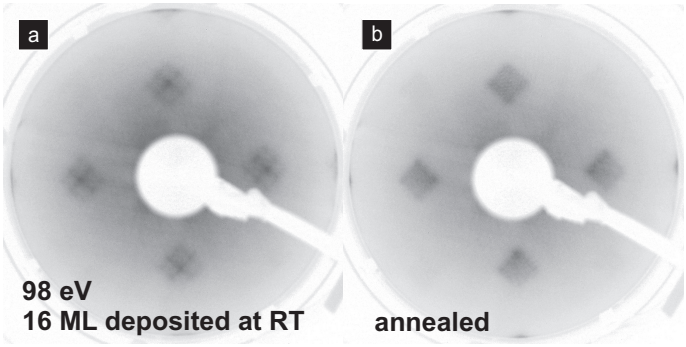

Figure 6.4: 16 ML thick MgO film deposited at RT onto 0.3 ML of Mg with the oxygen pressure during the formation of the first MgO ML 1.3×10^{-7} mbar, and increased to 5×10^{-7} mbar thereafter (at the Mg deposition rate of 2.2 Å/min). (a) LEED pattern of an as-deposited sample shows additional satellite spots around main MgO diffraction spots revealing 4 equivalent angles, characterizing the warped MgO surface above misfit dislocation lines. (b) LEED pattern after annealing at 400 °C for 20 mins showing instead a subatomic modulation of the height of the MgO film. The change in surface topography is further analyzed during the discussion of Figure 6.7, which features a real space image of the MgO film after annealing.

timal conditions for avoiding the overoxidation of the Fe substrate surface and maintaining the stoichiometry of MgO thereafter. Higher substrate temperatures applied during or after the growth usually lead to larger terraces, which is highly desirable in the case of the MgO/Fe system. In order to circumvent this limitation, two solutions were tested, both providing similar positive results. First, reducing the O_2 pressure at the beginning of the growth for a duration needed to grow the 1st MgO ML. Second, deposition of a submonolayer of Mg prior to the reactive growth of MgO. In an alternative third solution the r/p ratio could be controlled by varying the angle at which Mg is evaporated, and effectively changing its deposition rate. Figure 6.4a shows a 16 ML thick MgO film that was deposited at RT onto 0.3 ML of Mg with the oxygen pressure during the formation of the first MgO ML 1.3×10^{-7} mbar, and increased to 5×10^{-7} mbar thereafter (at the Mg deposition rate of 2.2 Å/min). Directly after growth, the sample is characterized by high crystalline order with misfit dislocations [24, 25, 28] revealed by additional satellite spots around the main MgO diffraction spots. After annealing at 400°C for 20 mins, the background in the LEED pattern is reduced, and there is a change in the appearance of the diffraction spots splitting (see Figure 6.4b). On as-deposited

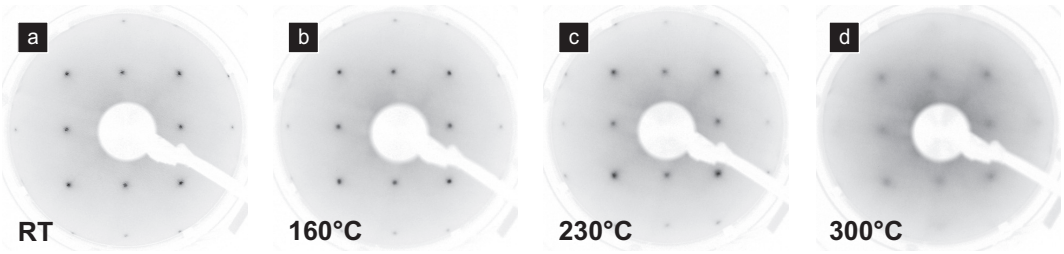

Figure 6.5: LEED patterns of 8 ML thick MgO films grown at temperatures from RT to 300°C (recorded at 141-145 eV electron energy). The O_2 pressure was 1.3×10^{-7} mbar during the formation of the 1st MgO ML, and increased to 5×10^{-7} mbar thereafter (at the Mg deposition rate of 2.0-2.5 Å/min). A higher crystalline order characterizes samples grown from RT up to 160°C. At 230°C the order is slightly reduced, with a significant decrease at 300°C.

samples, there are four equivalent angles characterizing the warped MgO surface above misfit dislocation lines, giving rise to distinct satellite spots connected with the main MgO spots by weak lines (see also Figure 6.7c). After the annealing there is instead a broad distribution of angles revealing a subatomic modulation of the height of the MgO film, which may originate from rearrangement at the MgO/Fe interface leading to local deformation of the crystalline lattice. The change in surface topography is further analyzed during the discussion of Figure 6.7, which features a real space image of the MgO film after annealing.

6.3.4 Effect of sample temperature during the growth

The temperature of the sample during the reactive growth is one of the important parameters determining the resulting film morphology. Usually an increased temperature helps in overcoming energy barriers for diffusion of adsorbates and leads to formation of larger islands. Figure 6.5 shows 8 ML thick MgO films grown at four different sample temperatures ranging from RT to 300°C (at the Mg deposition rate of 2.0-2.5 Å/min). A higher crystalline order characterizes samples from RT to 160°C. At 230°C the order is slightly reduced, with a significant decrease at 300°C. Such a change can be caused by the interfacial oxidation of the iron substrate, which is enhanced at higher temperatures, showing that the prevention measures based on changing the $^{r}/_{p}$ ratio require even further modi-

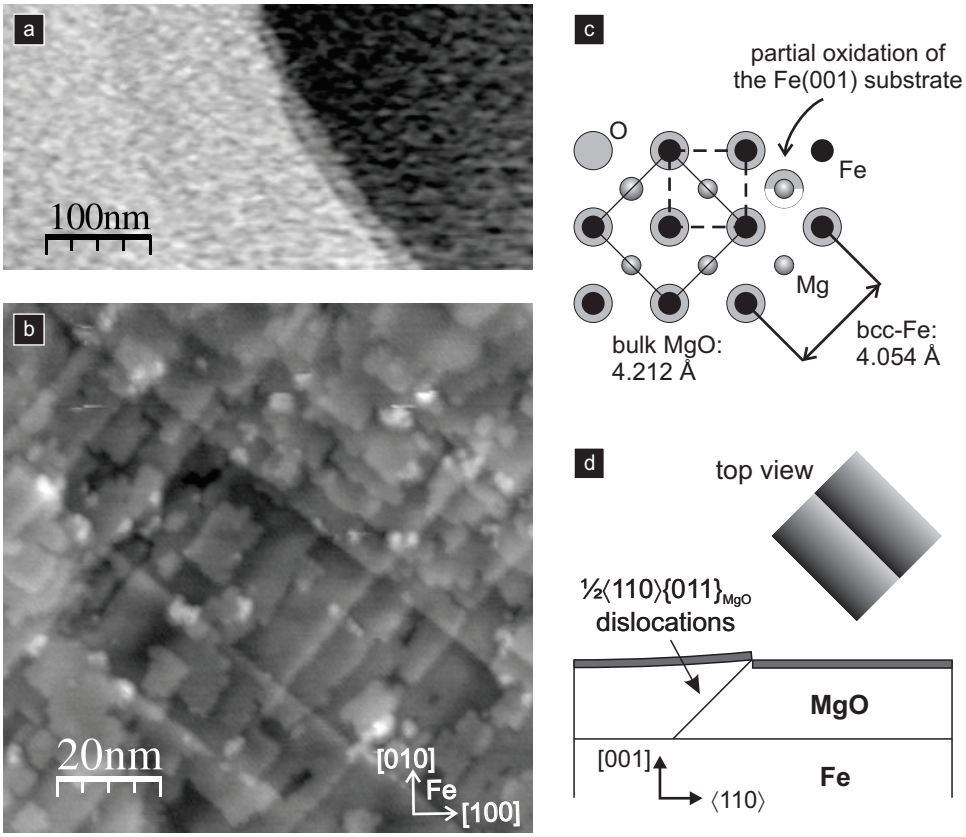

Figure 6.6: (a) A large-scale NC-AFM image of an 8 ML thick MgO film ($\Delta f = -2$ Hz, sample bias -2 V). (b) An enlarged NC-AFM frame showing an interface with directional step edges that are predominantly formed due to misfit dislocations ($\Delta f = -5$ Hz, sample bias -2 V). (c) A schematic diagram of the MgO/Fe registry. (d) The glide of $\frac{1}{2}\langle 011\rangle$ dislocations on $\{011\}_{\mathrm{MgO}}$ planes of the MgO film produces a monoatomic step at the surface.

fication during the initial stage of the growth. At elevated temperatures, other effects may also play an important role, such as (inter)diffusion of substrate and film atoms at the MgO/Fe interface and re-evaporation/desorption of Mg.

A large-scale NC-AFM image of an 8 ML thick MgO film deposited at 90°C is shown in Figure 6.6a. The surface is almost uniformly covered with the MgO film. An enlarged frame of the same film presented in Figure 6.6b shows an interface characterized by multiple dislocation lines and atomic step edges, running preferentially parallel to the $\langle 110\rangle$ directions of the iron substrate. In Figure 6.6c a schematic diagram of the MgO-Fe registry shows that such an orientation corresponds

to a charge neutral -Mg-O-Mg- termination, which confirms the orientation of the MgO film independently from the LEED measurements. Although the film appears to be rough, not all step edges lead to a real increase of the MgO film height and can instead be attributed to misfit dislocations. As revealed by the additional satellite spots in the LEED images (Figures 6.3 and 6.4), the MgO film contains a dense network of misfit dislocations that induce a warped MgO surface above them. This mechanism of strain relief has been discussed in detail by Dynna *et al.* [28] and is schematically presented in Figure 6.6d. Using MgO as a reference system, the glide of $\frac{1}{2}\langle 011\rangle$ dislocations on $\{011\}_{\mathrm{MgO}}$ planes of the MgO film produces a monoatomic step at the surface. The average dislocation periodicity is about 10 nm, which is close to the expected value of ~ 11 nm ($a_{\mathrm{MgO}} \cdot a_{\mathrm{Fe}}/|a_{\mathrm{MgO}} - a_{\mathrm{Fe}}|$, where $a_{\mathrm{MgO}} = 4.212$ Å, and $a_{\mathrm{Fe}} = 4.054$ Å – see Figure 6.6c). The surface is also characterized by atomic terraces of a similar size. Locally, the distance between dislocation lines can be as large as 20 nm allowing for the formation of larger terraces.

6.3.5 Effect of post-annealing observed by NC-AFM

The effect of post-annealing on the morphology of MgO films has been already demonstrated in Figure 6.4 using LEED measurements, which indicated an induced subatomic modulation of the MgO film height after annealing. To complement this, Figure 6.7a shows an NC-AFM image of an 8 ML thick MgO film annealed at 400°C. Compared to Figure 6.6b, annealing leads to an increase in the average distance between dislocation lines. Also, the MgO surface seems to be better ordered, as the number of atomic MgO islands is slightly reduced, and frequently the size of flat MgO areas is limited by the separation of dislocation lines. The subatomic modulation of the film height can be directly observed in Figure 6.7a in the area indicated by a square. Such warping of the surface most likely happens due to overgrowing of the dislocation planes, which were schematically shown in Figure 6.6d, however the buried interface itself cannot be probed directly by NC-AFM. Before the annealing, the surface of the MgO film is usually bent around four equivalent $\langle 011\rangle$ directions as shown in Figure 6.6b, which leads to a characteristic cross-like shape of the LEED spots (see Figures 6.4 and 6.7c). In contrast, after the annealing the MgO surface is also twisted around other direc-

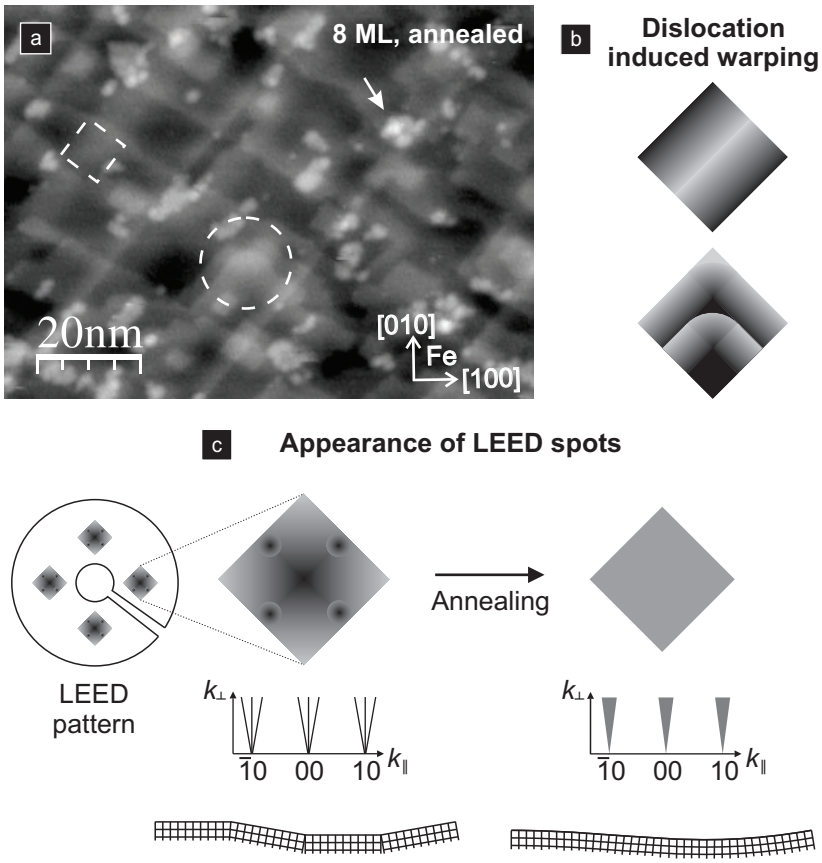

Figure 6.7: (a) NC-AFM image of an 8 ML thick MgO film after annealing at 400°C. The arrow indicates unidentified features, which can be attributed to an excess of magnesium that segregated on the surface after the annealing ($\Delta f = -2$ Hz, sample bias -2 V). (b) Additional warping of the surface formed after the annealing (exemplified by areas marked by the square and the circle in panel (a)). (c) Change in the appearance of LEED spots before and after the annealing (compare with Figure 6.4). After the annealing the well-defined satellite peaks in LEED spots in Figure 6.4 almost disappear leading only to a square-like shape that has a smaller size, which indicates a reduced maximum angle characterizing the distortion of the MgO film.

tions (see Figure 6.7a), which is caused by overgrowing of the dislocation planes and formation of surface features shown in Figure 6.7b. This additional distortion leads effectively to a less directional warping of the film height and consequently, the well-defined satellite peaks in the LEED image in Figure 6.4 almost disappear leading only to a square-like shape (see Figure 6.7c). The distinct shape of LEED spots indicates that there is a well-defined maximum angle characterizing the distortion of the MgO film. In particular, the square-like shape reveals that there is an anisotropy in the warping of the surface, which is related to the fourfold symmetry of the surface. After the annealing the square-like LEED spots become smaller, which confirms flattening of the film (see Figure 6.7c). One should also note that on samples fabricated under conditions leading to a slightly oxygen deficient film (see Figure 6.3), occasionally the quality of an initially sharp LEED pattern can deteriorate significantly after annealing. In this case annealing can force the excess of magnesium to diffuse and segregate on the surface in the form of clusters. Such metallic clusters, which can be electrically charged and repel the incoming beam of electrons, significantly disturb LEED measurements. In such a situation, the film can be well-ordered, but the LEED pattern will be very fuzzy. Although the sample in Figure 6.7a was grown under optimal conditions, there are some unidentified features (marked by an arrow), which can be attributed to an excess of magnesium that segregated on the surface after the annealing. However, such clusters were present in too small amounts to hinder the LEED measurements.

6.3.6 Advantages of the reactive deposition method

The presented protocol to grow epitaxial MgO films on the Fe(001) surface by reactive deposition produces an interface with well-defined terraces and a much higher quality compared to the growth by electron beam evaporation. In this way, by taking special precaution to avoid the interfacial reaction between the iron surface and the oxygen background atmosphere, films resembling the quality of MgO overlayers on Mo(001) and Ag(001) surfaces are formed [26, 27]. The reactive deposition method allows for full control over the gaseous species that reach the surface, making this protocol easily reproducible in various experimental settings. Conversely, the electron beam evaporation can be realized in two

configurations, where the evaporated target is either grounded or biased at a high positive voltage [29, 112]. Because such a beam is composed of two species [31], not necessarily in the same charge state, the exact design of the evaporator (which can be equipped e.g. with retarding grids) can decide the resulting beam composition. An interesting example is the growth of MgO by electron beam evaporation on Ge(001) studied independently by Han *et al.* [113] and Jeon *et al.* [114]. Although both groups used almost the same MgO deposition rate, the temperatures found to optimize the growth were significantly different, i.e. 250 °C vs. 125 °C. Such discrepancy in the temperature is significant and cannot be explained by the inaccuracy of *in-vacuo* temperature measurement. It suggests not only that each beam composition is unique and depends on the experimental setup, but also that the temperature of the substrate can effectively influence parameters, controlling such processes as: condensation of magnesium, condensation of oxygen, and nucleation of MgO. In effect, the rates of those processes can be controlled to some extent by the temperature of the sample, and optimal growth conditions can be potentially still reached.

The formation of the FeO_x layer has not been discussed here, as it is beyond the range of experimental methods used in this study. It was mentioned that an FeO_x layer can facilitate the epitaxial growth of MgO ultra-thin films on the Fe(001) surface [97]. Because of the direct exposure of the substrate to molecular oxygen, the interface must be partially oxidized. On the other hand, the high quality of MgO films indicates that the interfacial oxygen occupies only some fraction of a monolayer and does not lead to the formation of disordered iron oxide islands. From the thermodynamical point of view, the structure of the MgO/Fe interface is related to the interface contribution of an FeO_x layer to the surface energy, which decides the quality of layer-by-layer growth. The preferential quantity of FeO_x should be given by conditions that minimize the total energy of the system. Because the formation of FeO_x is governed by thermodynamics, it is expected to form to some extent regardless of the preparation method. Even a deposition of MgO by electron beam evaporation that is performed with special care to avoid the oxidation of the interface [115] leads to values of $x \approx 60\%$. In the reactive deposition method, this parameter must be significantly higher, but still does not exceed 100% as the Fe/MgO interface remains highly ordered.

6.4 Conclusions

The objective of this work was to use a reactive deposition method to improve the quality of MgO ultra-thin films grown on Fe(001) surfaces. We established a protocol that prevents an excessive interfacial reaction between oxygen and the Fe(001) surface, but at the same time provides sufficient amount of oxygen in order to grow a stoichiometric MgO film. We use the control over the gaseous species that reach the sample to either reduce the O_2 pressure at the beginning of the growth for a duration needed to grow the 1st MgO ML or to deposit a submonolayer coverage of Mg prior to the reactive growth of MgO. As revealed by LEED measurements, post-annealing of MgO films induces changes in the structure of misfit dislocations and flattening of the interface. Using NC-AFM we demonstrated that the reactive deposition method can produce terraces that have an average size of 10 nm, which is a significant improvement compared to other preparation methods.

7

Layer-by-layer growth of NaCl films on an Fe(001)-p(1x1)O surface

THIS CHAPTER IS BASED ON:
Tekiel, A.; Topple, J.; Miyahara, Y.; Grütter, P.
Layer-by-layer growth of sodium chloride overlayers on an Fe(001)-p(1×1)O surface
Nanotechnology **2013**, *23*, 505602 © 2012 by IOP Publishing.

This chapter discusses fabrication of adjustable tunnel barriers made of NaCl on the Fe(001)-p(1×1)O surface. Ultra-thin NaCl films epitaxially grown on the Fe(001)-p(1×1)O surface have been investigated in UHV by NC-AFM and LEED. It has been found that at temperatures below 145°C NaCl initially grows as islands of monoatomic-thickness on terraces, while at temperatures above 175°C islands of biatomic-thickness are also formed at substrate step edges. Both types of islands have the same Fe(001)-O[100]||NaCl(001)[110] orientation, leading to a (4×4) superstructure, where the NaCl unit cell is oriented at 45° with respect to the substrate. Interestingly, no c(2×2) superstructure with the NaCl unit cell oriented at 0° has been observed. The oxygen on the iron surface promotes layer-by-layer growth, resulting in atomically flat films with 40-60 nm wide terraces at coverages ranging from 0.75 to 12 ML. Such NaCl films have quality much higher than MgO films grown on Fe(001) and Fe(001)-p(1×1)O surfaces and represent a unique epitaxial system of an alkali halide on a pure metallic substrate. The reduced number of defects and the layer-by-layer mode of growth make this system very attractive for applications where an atomically-defined tunnel barrier is required to control properties of a device.

7.1 Introduction

Crystalline insulating ultra-thin films grown on a variety of metallic and semiconducting substrates attract considerable attention because of their importance in magnetoelectronics [5] and catalysis [6]. They are frequently used in systems where the film serves as a tunneling barrier directly controlling the properties of a device. For example, in magnetoelectronic applications and in model systems for heterogeneous catalysis the insulating film is often made of magnesium oxide that can be grown epitaxially layer by layer, usually on (001) surfaces of various metals, allowing for control of the tunneling barrier thickness. For this reason there has recently been increased interest in the growth and properties of crystalline oxide ultra-thin films [116], which includes oxides such as MgO, Al_2O_3, TiO_2 and V_2O_3. However, fully crystalline oxide ultra-thin layers are difficult to grow and are usually oxygen deficient. In the case of MgO films, these difficulties have been attributed to the MgO-metal lattice mismatch and the fact that in UHV, regardless of the preparation method, MgO is essentially grown from two separate sources of magnesium and oxygen, which have to react on the substrate to nucleate an MgO molecule [31, 117] (see Section 2.1.2). The quality of such oxide films is still much lower than that of insulating films based on alkali halides that, especially on closely lattice matched AIII-BV compound semiconductors, can form well-ordered films [33]. This quality difference can be explained by the fact that many alkali halides evaporated thermally form predominantly molecular monomers, and thus their growth is much better controlled due to reduced complexity of on-surface nucleation.

Alkali halide ultra-thin films can be grown on a variety of substrates, encompassing metals, semiconductors and insulators (see Section 2.1.3), however little is still known about the growth of such films on Fe(001) surfaces. Table 7.1 lists various alkali halide materials that crystallize in a *rock-salt* structure, which have a stable (001) surface. To identify possible lower-order commensurable relationships on the Fe(001) surface ($a = 2.870$ Å, a – lattice parameter) the original lattice parameters have been also multiplied by $1/2$ and $\sqrt{2}/2$, where the latter corresponds to a rotation of the two lattices in respect to each other by 45°. One can see that there are three potential candidates that could grow epitaxially on

Alkali halide	a - lattice parameter [Å]	$a/\sqrt{2}$ [Å]	$a/2$ [Å]
LiF	4.027	**2.848**	2.014
LiCl	5.140	3.634	2.570
LiBr	5.501	3.890	2.751
LiI	6.023	4.259	3.011
NaF	4.634	3.277	2.317
NaCl	5.640	3.988	**2.820**
NaBr	5.977	4.227	2.989
NaI	6.473	4.577	3.236
KF	5.347	3.781	2.674
KCl	6.293	4.450	3.147
KBr	6.600	4.667	3.300
KI	7.066	4.996	3.533
RbF	5.652	3.996	**2.826**
RbCl	6.581	4.653	3.291
RbBr	6.889	4.871	3.445
RbI	7.342	5.192	3.671
CsF	6.014	4.253	3.007

Table 7.1: Various alkali halide materials that crystallize in a *rock-salt* structure, which have a stable (001) surface. To identify possible lower-order commensurable relationships on the Fe(001) surface ($a = 2.870$ Å) the original lattice parameters have been also multiplied by $1/2$ and $\sqrt{2}/2$, where the latter corresponds to a rotation of the two lattices in respect to each other by 45°. Three potential candidates, LiF, NaCl and RbF are marked in bold.

the Fe(001) surface, namely LiF, NaCl, and RbF. During evaporation, LiF tends to form molecular dimers and trimers [118, 119], which are unfavorable for high-quality growth. In the case of NaCl and RbF, the composition of the evaporated beam is dominated by monomers, with a monomer/dimer ratio close to 10 [34, 35, 119] making them better candidates for growing ultra-thin insulating films on the Fe(001) surface. In this thesis, we focus on the growth of NaCl films, because there is a detailed literature of growth on NaCl on other surfaces.

Recent band structure calculations by Vlaic [120] predicted a high TMR ratio for Fe/NaCl/Fe(001) MTJs, but the experimental realization of such devices has been unsuccessful due to difficulty in sample preparation [121]. The growth of NaCl on iron is difficult to improve, likely due to corrosion of the substrate by NaCl during deposition or annealing of the system at elevated temperatures. Moreover, the closely matched lattices of NaCl and Fe in the c(2×2) structure do not necessarily guarantee good epitaxy. For example, on the *fcc* Ag(001) surface, where a 2.7%-compressed NaCl film could form a (4×4) structure, the growth is incommensurate with significant mosaic spread [46], and leads also to other orientations. More importantly the NaCl does not wet the silver surface, leading to a 3D growth starting even from the first layers.

As discussed in Section 5.3, the chemical and elastic properties of the Fe(001) surface, which strongly influence the growth of NaCl films, can be easily modified by terminating the surface with chemisorbed oxygen atoms. Exposure to several Langmuir of oxygen followed by flash annealing gives rise to the well-known Fe(001)-p(1×1)O surface, which has been thoroughly investigated by experimental and computational methods [83, 96]. The surface is characterized by one oxygen atom per unit cell chemisorbed in each hollow site of the Fe(001) and the same lattice parameter as the Fe(001) surface. As will be discussed in this work, the chemisorbed oxygen layer likely prevents the Fe(001) surface from the reaction with NaCl. Higher chemical stability allows for the use of elevated temperatures during sample preparation to enhance the diffusion of NaCl and improve the film quality. Moreover, the top layer of the Fe(001)-p(1×1)O surface resembles a planar *rock-salt* FeO monolayer. Compared to clean bulk iron, *rock-salt* FeO has better elastic properties, due to which the Fe(001)-p(1×1)O surface acts as a strain buffer in the epitaxy of ultra-thin films on top of it [97].

In this work, we report on layer-by-layer growth of well-ordered, ultrathin NaCl films on an oxygen covered Fe(001) surface. High-resolution NC-AFM measurements reveal that NaCl forms films of much higher quality than MgO on Fe(001), a prototype system among single-crystal MTJs. Although alkali halide films have been successfully grown on semiconductor surfaces with comparable high quality, there has been no report on a layer-by-layer growth of alkali halide films on a purely metallic substrate. The cubic lattice constant of *bcc* iron differs only by 1.8% from the nearest neighbor distance of the NaCl crystal, which should favor growth of a stretched NaCl film with a c(2×2) symmetry and its unit cell oriented at 0° with respect to that of the Fe(001), as shown in Figure 7.1f. We show, however, that this is not the case, and that the NaCl film is orientated at 45° with a (4×4) symmetry, which leads to a compression of the film by 4.2%. This unexpected film orientation is rationalized by the fact that an unsupported NaCl monolayer has a smaller lattice parameter than bulk NaCl, as the Madelung constant is reduced for a 2D ionic crystal. Consequently, with the NaCl unit cell orientated at 45°, the first NaCl monolayer is almost perfectly matched with the Fe(001)-p(1×1)O substrate in the (4×4) configuration.

7.2 Experimental details

All experiments reported here are performed in two interconnected UHV chambers (preparation and microscope) based on a commercial JEOL JSPM 4500a UHV AFM system. The base pressure is in the low 10^{-11} mbar range in the preparation chamber, and 1×10^{-10} mbar in the microscope chamber. Iron whiskers homegrown by reduction of $FeCl_2$ in an H_2 atmosphere with {001} side-surface orientations are used as the starting substrate [89]. The whiskers are cleaned by several cycles of 1 keV Ar^+ bombardment and subsequent annealing to about 600°C until a clean LEED pattern is observed, which leads to a surface with terraces several hundred nanometers wide. To produce the Fe(001)-p(1×1)O surface, the clean iron substrate is exposed to 8 L of molecular oxygen (99.997% purity) at room temperature and subsequently annealled to 400°C to remove the excess oxygen. A piece of NaCl single crystal (Korth Kristalle GmbH) is outgassed in vacuum and then evaporated from a Knudsen cell onto the Fe(001)-p(1×1)O sample kept at

temperatures in the 90-250°C range. NC-AFM is carried out at room temperature in the FM mode using JEOL AFM and Nanosurf "easyPLL" frequency detector. Commercial Nanosensors PPP-NCLR silicon cantilevers with a typical resonance frequency of 150-160 kHz and spring constant of ≈42 N/m are used with an oscillation amplitude of 5-7 nm. Two FM NC-AFM imaging modes are used. In the first one, used to record most of the images here, the frequency shift of the cantilever is maintained constant by a feedback loop controlling the z-piezo position, which is called the "topography mode". The second mode, called the "quasi-constant-height mode", used for obtaining atomic resolution, acquires the image with the feedback loop set to a very low value. In this case a frequency shift map is measured where brighter levels indicate larger negative frequency shifts. In the topography mode simultaneous FM KPFM (with 800 Hz modulation frequency, and $V_{\mathrm{RMS}} = 800$ mV modulation amplitude) is used to compensate for the local contact potential difference (LCPD) [122]. LEED images are taken with the use of four-grid LEED optics (Specs ErLEED).

7.3 Results and discussion

7.3.1 NaCl adsorption at submonolayer coverage

Submonolayer coverage of NaCl (approximately 0.75 ML; one monolayer is defined as one-atom-thick) is deposited at various sample temperatures and characterized by NC-AFM and KPFM (Figure 7.1). As shown in Figure 7.1(a) at temperatures 145°C and below, NaCl nucleates predominantly on the terraces and forms interconnected monolayer islands (measured height of 1.9 Å – see Figure 7.1b) that are roughly square-shaped showing preferential alignment of edges with $\langle 110 \rangle$ directions of the substrate. There is also some nucleation of NaCl bilayers (measured height 4.2Å) at the step edges of the Fe(001)-p(1×1)O surface. If the substrate temperature during the growth is increased to 175°C and above, the nucleation at the step edges becomes more pronounced and both types of islands are larger, as shown in Figure 7.1g. The same monolayer islands as described for the growth at lower temperatures form on the terraces, and bilayer islands nucleate at the step edges. Sporadically bilayer islands nucleated on a terrace can be found. The KPFM

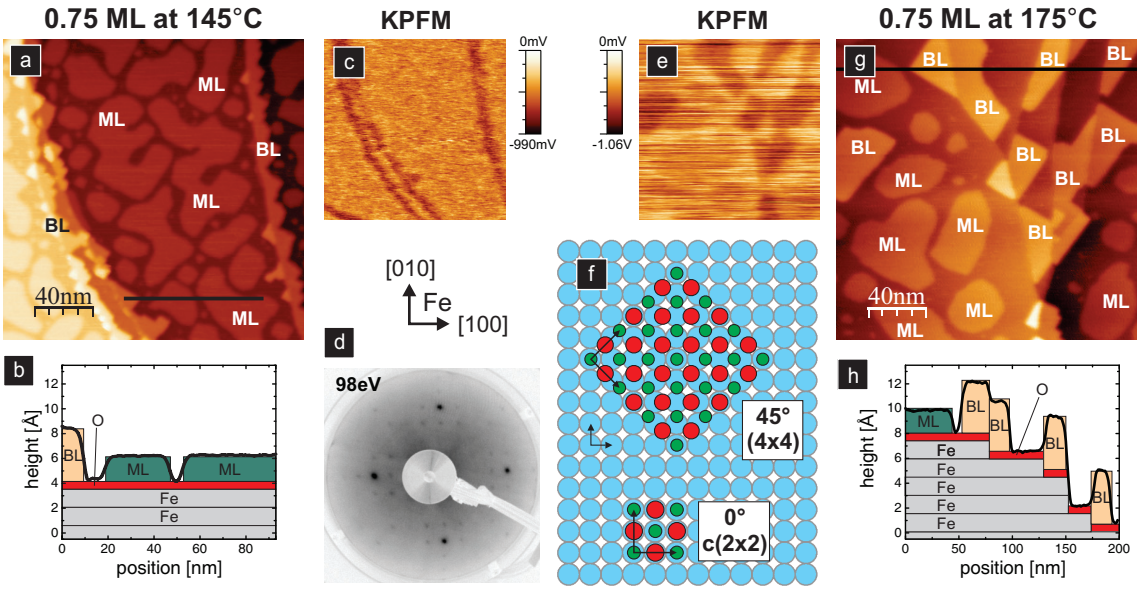

Figure 7.1: Structure of 0.75 ML NaCl film on Fe(001)-p(1×1)O grown at 145°C and 175°C. (a) and (g) NC-AFM topography images, (c) and (e) KPFM images, (b) and (h) typical cross sections and schematic coverage models for growth at 145°C and 175°C, respectively. (d) LEED image of 0.75 ML NaCl film grown on Fe(001)-p(1×1)O at 145°C taken at the electron energy of 98 eV. (f) Schematic representation of the NaCl film in both considered configurations.

images (presented in Figure 7.1, panels c and e) show weak contrast between uncovered Fe(001)-p(1×1)O surface and the first NaCl monolayer. However, there is significant LCPD observed for Fe(001)-p(1×1)O and NaCl bilayers, indicating a work function difference of ≈ 1eV. A similar trend in the LCPD dependence on the NaCl coverage has been described by Prada *et al.* for various insulating overlayers on metallic substrates [55].

The alignment of the edges of monolayer NaCl islands indicates that the unit cell of NaCl is rotated by 45° in respect to the substrate unit cell (see Figure 7.1f). In this orientation, the (4×4) structure can be identified as the most probable higher-order commensurable NaCl relationship with the film compressed by 4.2% and a square unit cell of 1.15 nm × 1.15 nm. This prediction is confirmed by an experimental LEED pattern shown in Figure 7.1d of 0.75 ML thick NaCl film grown on Fe(001)-p(1×1)O at 145°C, with not only first order diffraction spots visible for the Fe(001) surface and the NaCl film, but also clear (4×4) superstructure that is due to formation of a new, 4 times larger, unit cell at the NaCl/Fe(001)-p(1×1)O interface.

So far we have used the bulk lattice parameter for discussion of epitaxial relationship in the growth of NaCl films on the Fe(001)-p(1×1)O surface. However, even a simple approximation based on Madelung energy shows that an NaCl monolayer with a {001} orientation favors a smaller distance between closest Na^+ and Cl^- ions. Structure of ionic crystals can be characterized by a simple model that includes the repulsion energy between the closest neighbors and the Madelung energy of the crystal lattice [123]:

$$U_{\text{tot}} = N\left[z\lambda \exp\left(-\frac{R}{\rho}\right) - \alpha\frac{q^2}{R}\right]. \tag{7.1}$$

where N is the number of NaCl pairs, z the number of closest neighbors, R the distance between closest anions and cations, λ and ρ are empirical parameters describing the repulsion between closest anions and cations, and α is the Madelung constant. For NaCl bulk crystal: $z = 6$, $R = 2.82$ Å, $z\lambda = 1.05$ erg, $\rho = 0.321$ Å and $\alpha = 1.747565$. The lattice parameter of unsupported NaCl monolayer can be estimated by taking the 2D Madelung constant, which is 1.615542 [124] and by reducing z to 4. This leads to a lattice parameter of 5.36 Å ($R = 2.68$ Å), which compared

to 5.64 Å for bulk NaCl is reduced by 4.7%. More accurate calculations based on density functional theory (DFT) have provided similar values: 5.40 Å [125], 5.45 Å [42], and 5.55 Å [126]. The matched lattice parameters of the NaCl monolayer in the (4×4) and c(2×2) structures are 5.41 Å and 5.74 Å, respectively. Using the same approach based on Madelung energy, one can estimate the energy cost for stretching an unsupported monolayer to match the (4×4) and c(2×2) surface lattices of Fe(001), which gives only 0.0027 eV for the former, but 0.1114 eV for the latter (per one NaCl molecule). This difference in energy cost suggests that formation of the c(2×2) structure would require much larger site-dependent film-substrate interaction, while the lattice of an NaCl monolayer is almost perfectly matched in the (4×4) configuration.

The simple approximation of a monolayer based on Madelung energy shows that the bulk lattice constants listed in Table 7.1 are not directly relevant to the selection of suitable candidates for growth on a given substrate. A revised set of lattice parameters should be calculated with values expected to be smaller than the bulk lattice constants to get new and potentially different candidates.

7.3.2 Structure of 2 ML thick NaCl film

Figure 7.2 shows the influence of substrate temperature during deposition on the morphology of NaCl film that has nominal thickness of 2 ML. When deposited at 120°C the surface is mostly uniformly covered with NaCl film with a small number of holes in it and a few islands in the 3rd atomic layer (Figure 7.2a), revealing a layer-by-layer growth with a small amount of roughening. If the substrate temperature is higher during the growth (145°C and above – see Figures 7.2b and 7.2c), the growth at substrate step edges starts to disturb the nearby growth. The islands next to step edges are usually taller than the NaCl film on average, and there is a distinct, irregular network of dislocations, especially nearby such areas that locally are covered by a larger number of atomic NaCl layers. As clearly shown in Figure 7.2b, on the terraces, such dislocations appear as bright lines in the AFM image, and usually run along $\langle 100 \rangle$ directions of the substrate far from step edges (one should distinguish these bright dislocation lines from NaCl step edges also appearing as bright lines in Figure 7.2b, which is a common contrast in

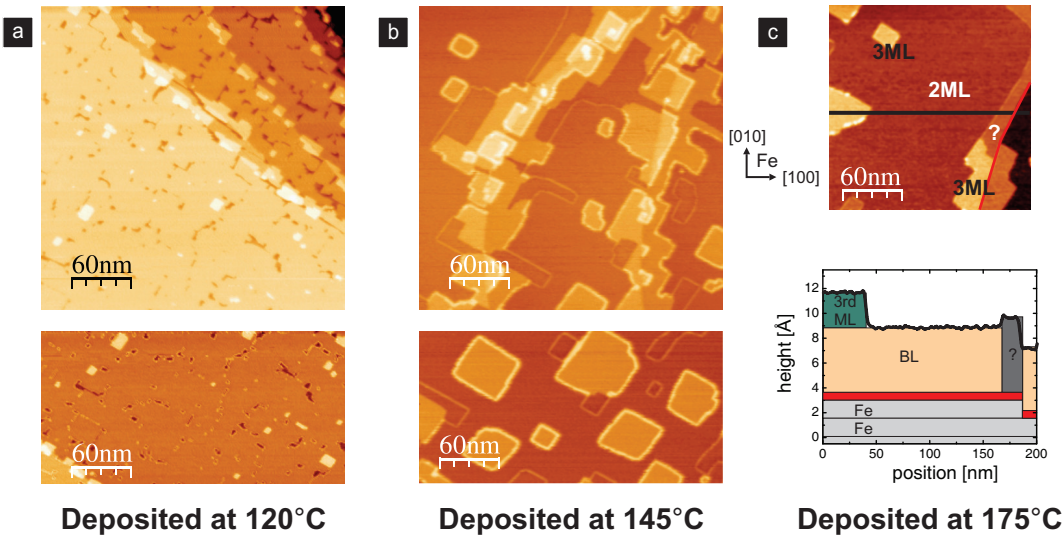

Figure 7.2: Structure of 2 ML NaCl film on Fe(001)-p(1×1)O grown at (a) 120°C, (b) 145°C and (c) 175°C. (a) and (b) show well-defined irregular networks of dislocations that appear as bright lines far from step edges and usually align along ⟨100⟩ directions of the substrate. (c) A typical cross section taken above an underlying Fe step edge and a schematic coverage model for growth at 175°C. The red line in the NC-AFM image shows the position of substrate step edge.

imaging alkali halides films by NC-AFM [127]). The cross section in 7.2c shows that close to the step edges, where the film morphology is irregular (which happens especially after the deposition at temperatures above 145°C) the height of the NaCl film in some regions cannot be assigned to any integral number of monolayers indicating that the local orientation of the film may differ. Based on the DFT calculations by Olsson *et al.* [126], although an unsupported NaCl monolayer is characterized by a much smaller lattice parameter, an NaCl bilayer already has a lattice parameter similar to the bulk value. This means that in the 2 ML coverage range the NaCl film experiences a significant change in energetically favorable distance between closest Na^+ and Cl^- ions. Therefore, the well-defined bright lines, which are observed on all 2 ML samples grown at temperatures 120-175°C, can be identified as a mechanism of strain relief due to overgrowing of the first by the second NaCl monolayer and related to structural instabilities of the film. It should be noted that considering only the almost bulk-like lattice parameter of a 2 ML thick unsupported film, the NaCl film could be better matched with the Fe(001)-p(1×1)O substrate in the c(2×2) orientation. However, this simple picture does not correspond to the real process of the film growth: the first monolayer determines the orientation of the film, regardless how many subsequent layers are deposited.

7.3.3 Structure of 4 ML thick NaCl film: effect of post-annealing

Figure 7.3a shows NaCl coverage of nominal 4 ML deposited at 120°C, where a completed 3rd ML, incomplete 4th ML and a very small number of islands in 5th ML are visible. The islands in the 4th ML have typical size of 30-50 nm across. One cannot observe dislocation lines that are characteristic for the structure of 2 ML thick film, which suggests that layers beyond the first 2 ML successfully overgrow the interface with such defects. Although the topography in Figure 7.3a reveals only very well-ordered incomplete 4 ML, the LCPD map recorded on the as-deposited sample (Figure 7.3b) shows a complex pattern with significant local variations (68% values are within an interval of 148 mV). Such local changes in LCPD indicate that the film is nonuniform. Because the top-most layer is near-perfect and the only defects can be attributed to step edges due to an incomplete 4th ML, this variation must originate from subsurface structural defects in the deeper

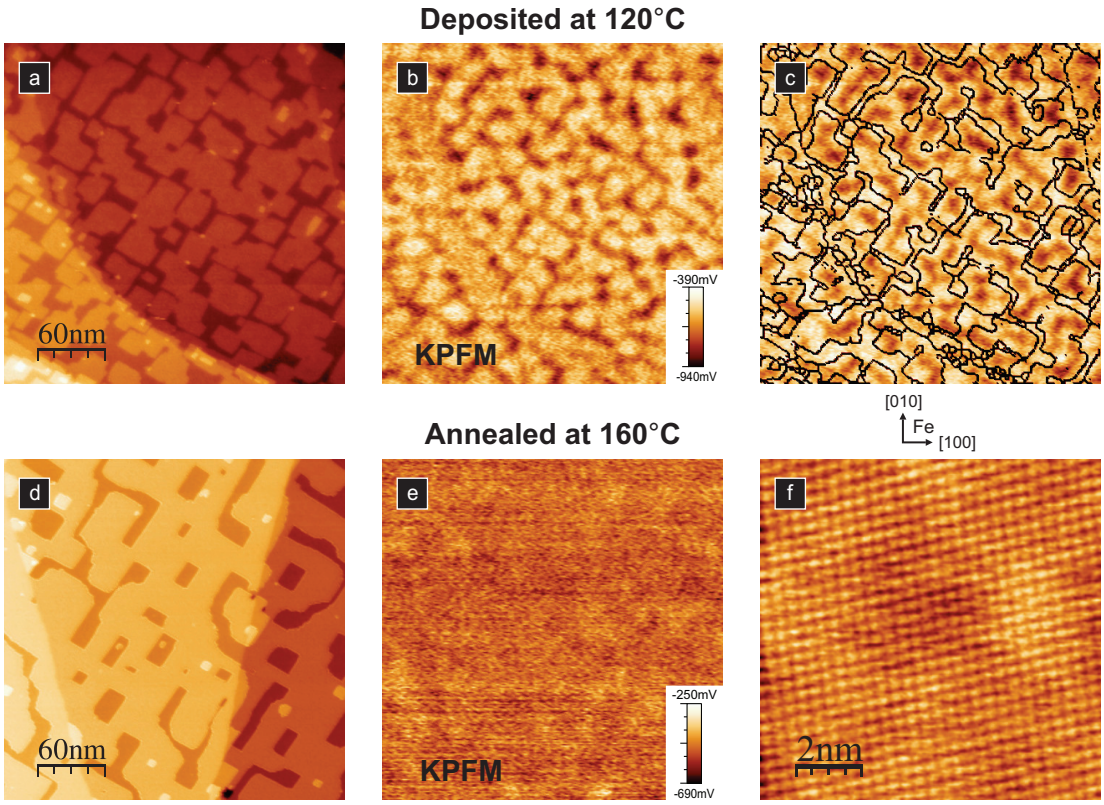

Figure 7.3: Structure of 4 ML NaCl film on Fe(001)-p(1×1)O grown at 120°C and after additional post-annealing at 160°C. (a) and (d) NC-AFM topography images, (b) and (e) KPFM images for as-grown samples and after post-annealing, respectively. (b) shows nonuniform LCPD map recorded on the as-deposited sample with significant local variations. (c) The positions of islands edges from (a) superimposed with the KPFM image (b) showing that dark spots in LCPD are usually located within central areas of the islands of the 4th ML. (e) KPFM image after post-annealing showing more uniform LCPD pattern without features correlated with positions of NaCl islands. (f) Molecularly resolved image (the lattice is slightly distorted due to thermal drift) confirming that the NaCl unit cell is oriented at 45°, as expected in the (4×4) structure.

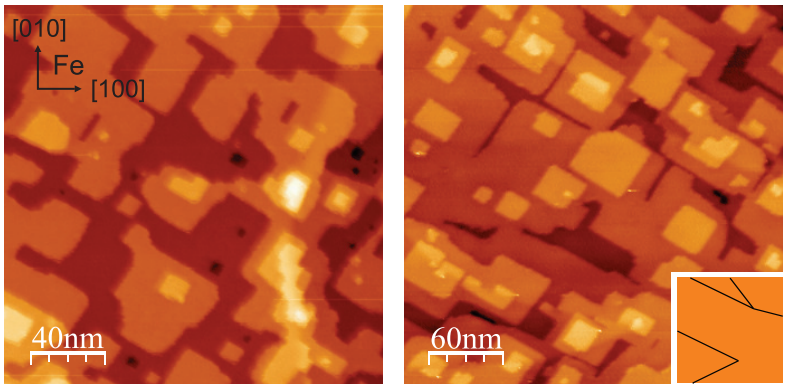

Figure 7.4: Structure of 12 ML NaCl film on Fe(001)-p(1×1)O grown at 120°C and annealed at 160°C for 2 hours showing almost layer-by-layer growth with a small number of defects. Usually only screw dislocations atop of the substrate step edges can be observed. The inset shows positions of substrate step edges of atomic height.

lying layers of the NaCl film. In Figure 7.3c the positions of islands edges from the 4th ML are superimposed with the KPFM image. The dark spots are usually located within central areas of the islands of the 4th ML, which means that the position of the defects and the distribution of those islands are mutually correlated.

Figure 7.3, panels d and e, shows the change after annealing at 160°C in the sample morphology and LCPD, respectively. As prior to annealing, the sample is characterized by a network of coalesced islands that have become larger on average. It is worth noting that the NaCl coverage remains similar and there is no noticeable reevaporation of NaCl from the surface. Interestingly, after annealing the LCPD contrast is more uniform (68% values are within an interval of 84 mV), but more importantly it does not have the same feature pattern observed prior to annealing. This suggests that the subsurface defects in the NaCl film have been party healed and now have less impact on the film morphology and strain. Figure 7.3f shows also a molecularly resolved image (i.e. either the Na or the Cl sublattice marked by green or red colour in Figure 7.1f) of the 4th ML confirming independently that the NaCl unit cell is oriented at 45° with respect the unit cell of the substrate, as expected for the (4×4) structure.

7.3.4 Layer-by-layer growth

Starting from the 2nd ML, the NaCl film successfully overgrows the Fe(001)-p(1×1)O step edges, which proves that this system can be used to fabricate continuous and uniform tunneling barriers over large sample areas that exceed the typical size of Fe(001)-p(1×1)O terraces. Based on the above observations, we propose a protocol to fabricate high quality NaCl films, where the film is first grown at a temperature hindering the extended growth at the step edges (120°C), and next it is annealed at higher temperature (160°C for 2 hours) to improve the crystallinity and increase the average island size. Figure 7.4 shows an example of almost layer-by-layer growth of 12 ML thick NaCl film. Although the height of a step edge on the Fe(001)-p(1×1)O surface is 1.44 Å, which does not match the distance between the atomic planes in the NaCl crystal, the NaCl still overgrows the substrate step edges. The inset in Figure 7.4 shows positions of substrate step edges of atomic height. In such cases only screw dislocations atop of the step edges form and the average coverage of the film is preserved. This proposed protocol is potentially useful for application in nanoscale systems requiring continuous and uniform crystalline tunneling barriers, including magnetoelectronic and catalytic applications, but also in fundamental science where ultra-thin films are frequently used to decouple electronically adsorbates from the metallic substrate [44]. NaCl films can be grown on the Fe(001)-p(1×1)O surface layer by layer with a remarkable quality up to the thickness of 12 ML, as demonstrated in this work.

7.3.5 The role of oxygen

Oxygen plays a significantly different role in the growth of NaCl than it does in the growth of easily oxidizable metals on Fe(001). During the deposition of metals such as Mn, Cr, and also the homoepitaxy of iron, oxygen acts as a surfactant and floats during the growth on top of the deposited film, improving layer-by-layer growth [128]. In contrast, the interaction between oxygen and NaCl is much weaker [129] than the interaction between oxygen atoms and the Fe(001) surface, which was calculated by Blonski [130] and is characterized by adsorption energy of 3.09 eV indicating strong chemisorption. Thus, oxygen is permanently bound to the iron surface and does not leave it, even with the NaCl film grown on

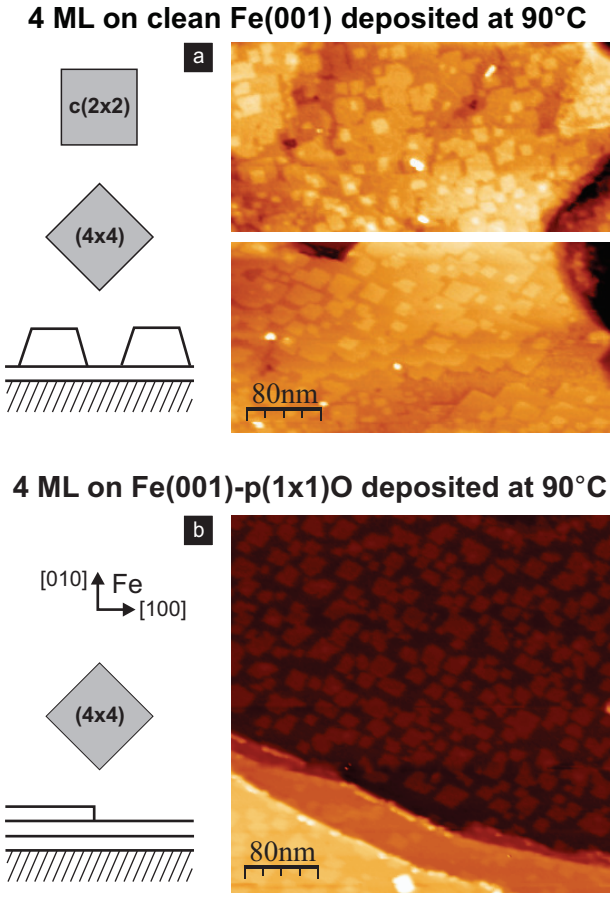

Figure 7.5: Comparison of the morphology of 4 ML NaCl film deposited at 90°C directly onto (a) the clean Fe(001) surface and (b) the Fe(001)-p(1×1)O surface. In (a) the growth resembles Stranski-Krastanov mode and one can observe areas on the sample with film orientations corresponding to the (4×4) and c(2×2) structures. In (b) NaCl grows layer by layer leading only to the (4×4) orientation.

top. Strong binding of oxygen to iron can additionally help in protecting it from unwanted reaction with NaCl and formation of surface iron chloride that could be triggered at higher sample temperatures [131]. Indeed, our preliminary tests indicated that evaporation of NaCl directly onto clean Fe(001) surface already at 160°C leads to its partial destruction. The effect of this reaction can be minimized by limiting sample temperature during preparation, which also reduces diffusion of NaCl and the average size of NaCl islands. Figure 7.5 compares the morphology of 4 ML NaCl deposited at 90°C directly onto a clean Fe(001) surface and the Fe(001)-p(1×1)O surface. There are two unwanted phenomena occurring on the Fe(001) surface. First, one can immediately notice that the growth on the clean Fe(001) substrate resembles Stranski-Krastanov mode (Figure 7.5a – see also Section 2.1.1). Second, instead of only one film orientation, there are two coexisting orientations on the sample, corresponding to the (4×4) and c(2×2) structures. Sodium chloride on the Fe(001)-p(1×1)O surface grows layer by layer (Figure 7.5b, also know as Frank-van der Merwe mode – see Section 2.1.1), which can only be observed if there is no substantial strain in the grown film. As mentioned before, the FeO-like top layer of the substrate is expected to have much better elastic properties suited for supporting ultra-thin films and act as a strain buffer, which is clearly demonstrated in Figure 7.5.

Calculations have shown that MTJs based on the Fe(001)/MgO(001)/Fe(001) structure should have a very high TMR ratio [98, 99], but there is large discrepancy between the theoretical and reported experimental TMR values [30, 56]. Therefore, specific studies have been focused on the role played by oxygen at the Fe/MgO interface, as this kind of contamination may easily originate from rest gases in the growth chamber or from the growth of MgO itself. It has been shown that the theoretical predictions of TMR are very sensitive to the quality of the Fe/MgO/Fe junctions. A small amount of oxygen has a drastic effect on the TMR amplitude [102, 103]. Also the oxygen-deficiency of the MgO film and formation of oxygen vacancies induces detrimental diffusive scattering [132]. Additionally, MgO films on Fe(001) are characterized by a dense network of misfit dislocations, which has not been included in theoretical calculations yet. From this point of view, new MTJs based on crystalline NaCl ultra-thin films of much higher quality constitute a promising alternative to MgO tunnel barriers. Moreover, such high order of the

NaCl tunneling barrier should resolve the discrepancy between theoretical modeling and experimental realization of a potential device.

Concerning magnetic applications of the NaCl/Fe(001)-p(1×1)O system, we demonstrated in this work that the formation of FeO-like interface is crucial for obtaining layer-by-layer growth. Such high quality of ultra-thin films has never been observed in the MgO/Fe(001) system [29, 133]. Although the presence of oxygen at the interface may reduce the TMR in an MTJ based on NaCl, the NaCl/Fe(001)-p(1×1)O system represents much higher structural quality than that of MgO films. Electronic band structure calculations [120] predicted a very high TMR ratio for the Fe/ NaCl/Fe(001) MTJ (without oxygen at the interface) where the NaCl film forms the c(2×2) structure. Theoretical modeling is needed here to calculate magnetic properties of (4×4) NaCl films on the Fe(001)-p(1×1)O surface and understand the impact of oxygen on the performance of a potential MTJ. Although the TMR may be reduced by the presence of oxygen, the fact that the system quality is very high can be very beneficial for obtaining a high TMR ratio, as the density of states in such device may be less affected by any structural defects at the NaCl/Fe(001)-p(1×1)O interface.

7.4 Conclusions

We report a protocol for the layer-by-layer growth of well-ordered, ultra-thin NaCl films on the Fe(001)-p(1×1)O surface at coverages ranging from 0.75 ML to 12 ML. Characterization of a submonolayer reveals two growth modes: on the terraces as monoatomic thick islands, and at the step edges as bilayer islands. In both cases the NaCl unit cell is oriented at 45° with respect to the substrate leading to a (4×4) superstructure. The effect of sample temperature during the growth and during post-annealing is identified: First, deposition at lower sample temperatures (120°C) can successfully reduce the extended growth of bilayer islands at substrate step edges. Second, subsequent post-annealing can improve the crystallinity of the film and increase the size of NaCl terraces. We explain the (4×4) structure of the NaCl film by the fact that at the initial stage of growth, during formation of the first monolayer, the lattice parameter of the 2D NaCl film is reduced compared to the bulk value and in that configuration matches perfectly the

Fe(001)-p(1×1)O lattice. The oxygen on the iron surface promotes layer-by-layer growth allowing the formation of atomically-flat films with 40-60 nm wide terraces at coverages up to 12 ML. Such high quality of NaCl films makes this system a better candidate than MgO films on metals for applications where an adjustable tunneling barrier is needed.

8

Single-electron charging of Au nanoparticles at room temperature detected by electrostatic force microscopy

THIS CHAPTER IS BASED ON:
Tekiel, A.; Miyahara, Y.; Topple, J.; Grütter, P.
Room-temperature single-electron charging detected by electrostatic force microscopy
ACS Nano **2013**, *7*, 4683-4690 © 2013 by American Chemical Society.

The previous two chapters discussed the growth of tunnel barriers of MgO and NaCl ultra-thin films. The reduced number of defects of NaCl overlayers makes this system a better candidate than MgO for applications requiring high quality tunnel barriers. In this chapter, we use the NaCl film as an adjustable tunnel barrier to characterize single-electron charging at room temperature of individual Au nanoparticles formed after thermally evaporating Au onto the NaCl film. Due to the small size of the nanoparticles (3.5 nm high), Coulomb blockade behavior can be observed at room temperature. We illustrate how a combination of single-electron sensitive electrostatic force microscopy (*e*-EFM) and finite element electrostatic simulation can be used to reveal electronic and morphological properties of individual Au nanoparticles. The electron addition energy, the capacitance, tunneling rates and an approximated shape of an individual Au nanoparticle have been determined. Numerical simulations point towards a total capacitance dominated by the mutual capacitance between the nanoparticle and the back electrode. Comparison with the experimental value, determined from measurement of the addition energy, indicates that the nanoparticles should be modeled as truncated spheres in order to reduce the mutual capacitance to the substrate.

8.1 Introduction

In nanoelectronic devices where components are connected by tunnel barriers and capacitively coupled to external electrodes, the transport can be dominated by single-electron effects. Among such phenomena, Coulomb charging plays a key role in many systems, including single-electron transistors and single-electron memory devices [8]. Measurement of the capacitance between the components of nanoscale circuits and understanding its origin is of great importance for improving such devices in order to work reliably at room temperature [7, 9]. However, characterization of local electronic properties becomes increasingly challenging as structures are reduced to nanoscale dimensions. Methods based on transport measurements and conventional charge sensing are limited in flexibility since they require lithographic techniques to fabricate nanoscale electrodes. In this work, we use *e*-EFM to characterize charging of individual Au nanoparticles, including measurement of electron addition spectra and tunneling rates. The nanoparticles are separated from an Fe(001) back electrode by an ultra-thin NaCl film and due to their small size exhibit Coulomb blockade at room temperature. Because the *e*-EFM technique can both image the topography of the studied device and measure electronic properties of individual nanoparticles, it allows for exploring structure-property relationships. Given the simple design of the studied system, we use finite element electrostatic simulation to examine the relevant contributions to the total nanoparticle capacitance, which is determined experimentally from the measurement of electron addition energy.

The *e*-EFM technique is a new and extremely versatile method that is based on NC-AFM and suited for characterization of nanostructures supported on ultra-thin insulating films. In *e*-EFM an oscillating AFM tip is used both as a gate to charge individual nanoparticles with single electrons from a conducting back electrode, and a charge-sensitive probe to detect the tunneling through a change in cantilever energy dissipation. As a scanning probe technique, *e*-EFM can routinely access nanometer length scales and offers an alternative approach that overcomes the difficulty of attaching the electrodes to nanoscale structures. The *e*-EFM technique has been successfully used at cryogenic temperatures [70, 71, 73, 134–137] to measure energy spectra (ground [70] and excited states [137]), electron tunneling

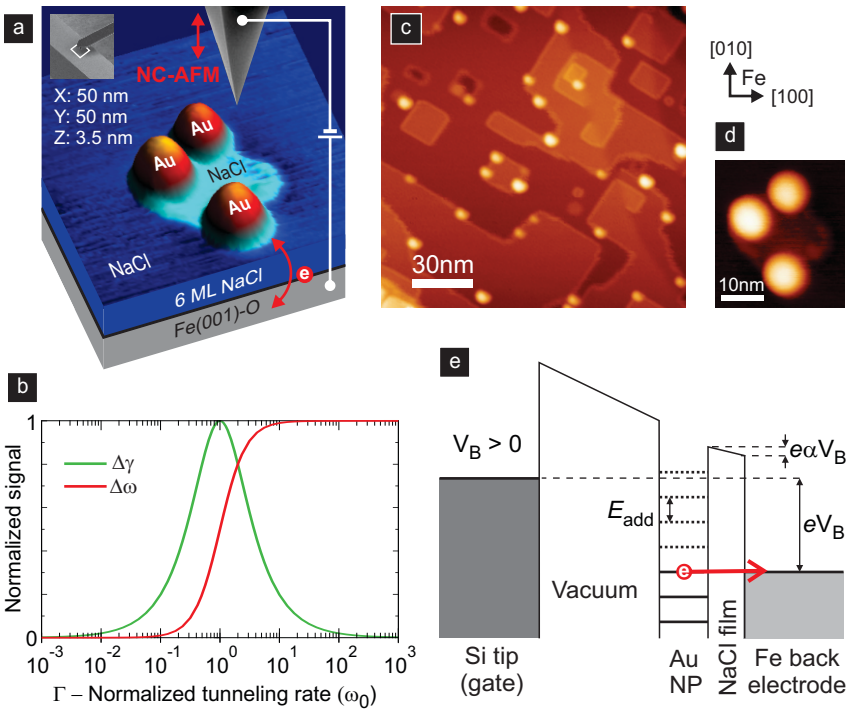

Figure 8.1: (a) Schematic of the studied system. The AFM tip is used as a local gate to charge individual nanoparticles with electrons from the back electrode. (b) Plot of the dissipation and resonance frequency shift response (in normalized units) versus the normalized tunneling rate (in units of the cantilever resonance frequency, $\omega_0 = 2\pi f_0$). (c) Topography of an NaCl ultra-thin film with a submonolayer coverage of Au that self-assembled into homogeneous nanoparticles. (d) Topography of studied Au nanoparticles (the width of the nanoparticles derived from AFM measurements is overestimated). (e) Energy diagram of the system for positive sample bias allowing for sequential unloading of electrons.

rates, as well as shell structures [70] of various nanoscale structures and entities. It is clear that in principle this technique, which has been used at temperatures as high as 95 K [70], could also work at room temperature and lead to wide-ranging applications [73]. So far, however, the only *e*-EFM experiment conducted at room temperature reported a relatively weak signal [138], making characterization of individual nanostructures difficult. In this work, we extend the *e*-EFM technique to room temperature by carefully tuning the sample design and fabrication relative to the cantilever response to achieve maximum sensitivity.

The essential part of the *e*-EFM method is an insulating film that separates

the nanostructures under investigation from a back electrode, which is shown schematically in Figure 8.1a. The rate of tunneling through the ultra-thin insulating film largely decides the sensitivity of the method by affecting the relative strength of the cantilever dissipation and frequency shift signals [73] which are measured in *e*-EFM. One can obtain the cantilever resonance frequency shift and dissipation induced by the periodic tunneling process [73]:

$$\Delta\omega \propto \frac{\omega\Gamma^2}{\omega^2+\Gamma^2}, \tag{8.1}$$

$$\Delta\gamma = \Delta\left(\frac{1}{Q}\right)\omega \propto \frac{\omega^2\Gamma}{\omega^2+\Gamma^2}, \tag{8.2}$$

where $\omega = 2\pi f$. $\Delta\left(\frac{1}{Q}\right)$ denotes the energy dissipation per one oscillation cycle, while $\Delta\gamma$ is the energy dissipation per unit time. Figure 8.1b shows that the dissipation of the cantilever, $\Delta\gamma$, is maximal when the tunneling rate is matched with the oscillation frequency of the cantilever, while the frequency shift, $\Delta\omega = 2\pi\Delta f$, increases with increasing tunneling rate. Although the signal could be optimized by a proper choice of the cantilever, this imposes a potential limitation due to the range of resonance frequencies (10-1,000 kHz) of commercially available AFM probes. Alternatively, the *e*-EFM technique can be made sensitive at room temperature by achieving full control over the tunnel barrier thickness and adjusting the tunneling rate to the cantilever resonance frequency. We utilize an ultra-thin epitaxial NaCl film as the tunnel barrier, grown in UHV on the Fe(001)-p(1×1)O surface of the Fe back electrode. As shown in Chapter 7, our group has developed a method to grow such films layer by layer with a small number of defects [139]. Metal nanoparticles, formed by thermally evaporating Au onto the NaCl surface, are used as electron-confining nanostructures. Figure 8.2 demonstrates that on NaCl films, Au exhibits a strong affinity for substrate steps, similarly to alkali halide bulk surfaces [140–143], and the size of the nanoparticles can be controlled by the amount of the deposited material.

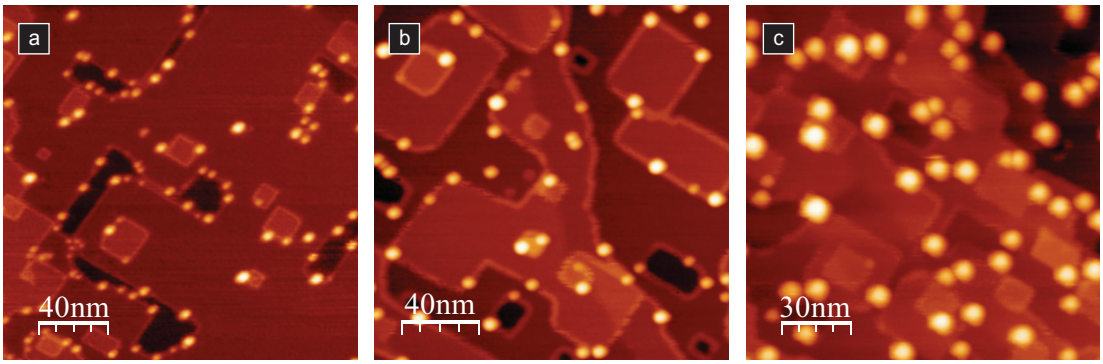

Figure 8.2: (a) $\approx$ 0.01 ML of Au on 6 ML thick NaCl film, 200 nm $\times$ 200 nm, density of nanoparticles 1.9×10^{11} NP/cm^2. (b) $\approx$ 0.01 ML of Au on 10 ML thick NaCl film, 200 nm $\times$ 200 nm, density of nanoparticles 1.2×10^{11} NP/cm^2. (c) 0.05 ML of Au on 12 ML thick NaCl film, 150 nm $\times$ 150 nm, density of nanoparticles 2.4×10^{11} NP/cm^2.

8.2 Experimental details

The experiment, including sample preparation and characterization, was performed in a modified commercial JEOL JSPM 4500a UHV AFM system. The detailed preparation procedure of the NaCl film, which was grown on an Fe(001)-p(1$\times$1)O surface, is described in Chapter 7 (see also [139]). A submonolayer of Au was deposited by an electron-beam evaporator (Oxford Applied Research EGN4, fitted with a charge-retarding grid) onto the sample, which was kept at room temperature. For data acquisition and cantilever oscillation, an SPM control system from SPECS-Nanonis was used. A highly doped Si cantilever (Nanosensors PPP-QNCHR) with a resonance frequency of approximately 286 kHz, Q-factor of 33,000 and nominal spring constant of 42 N/m was oscillated with a phase-locked loop oscillation controller (OC4 from Nanonis). The amplitude controller was used to regulate the driving signal amplitude in order to keep the oscillation amplitude constant while tracking the resonance frequency of the cantilever with a phase-locked loop. The topography images were taken in constant frequency shift mode, where the frequency shift of the cantilever was maintained constant by the SPM feedback loop controlling the z-piezo position. The dissipation of the cantilever can be extracted by measuring the Q-factor degradation, which corresponds to the amplitude of the cantilever drive signal needed to keep the amplitude of the os-

cillation constant [70]. The dissipation images were recorded in constant-height mode with linear z-drift compensation [144]. The correction for the vertical drift improved the stability of the tip height at room temperature by reducing its change to only a fraction of a nanometer over the time needed to scan one frame, which typically was 15 minutes. During the experiment, the vacuum pressure was maintained in the low 10^{-10} mbar range.

8.3 Results and discussion

Figure 8.1c shows an NaCl film at a nominal thickness of 7 atomic monolayers with a submonolayer coverage of Au. The epitaxial NaCl film has a (001) orientation and a (4×4) symmetry with charge-neutral step edges oriented along the $\langle 110 \rangle$ directions of the Fe(001) substrate. It grows in a near perfect layer-by-layer mode, allowing for precise control of the tunnel barrier thickness [139]. Although the underlying step edges of Fe slightly disturb the nearby growth of NaCl, on flat substrate areas the film is characterized by an almost complete 6th ML, and a far from complete 7th ML. To meet the requirement for the electron addition energy, E_{add}, to be larger than $k_{\text{B}}T$ at room temperature, a small amount of Au (approximately 0.02 ML) was deposited that resulted in the formation of isolated nanoparticles (with an average number density of 1.3×10^{11} NP/cm^2, see Figure 8.1c). The nanoparticles are anchored symmetrically above NaCl step edges and are homogeneous in size. In Figure 8.1d the size of the studied nanoparticles is characterized by a height of 3.5 nm when measured from the lower NaCl terrace and a diameter of approximately 10 nm. In topography characterization, the AFM tip usually leads to increased lateral dimensions due to tip convolution effects [140, 141, 143]. For this reason, the width of the nanoparticles derived from the AFM topography measurement is certainly overestimated.

To induce tunneling between a supported Au nanoparticle and the back electrode, the AFM tip is placed at a height within several nanometers above the nanoparticle (see Figure 8.1a). A DC bias voltage, V_{B}, is applied to the back electrode, while the oscillating cantilever is electrically grounded. Tunneling between the tip and the nanoparticle is negligible because of the large barrier height and width (~ 5 nm) of the vacuum gap. The potential drop between the Au nanopar-

ticle and the back electrode, i.e. across the NaCl tunnel barrier, is a fraction of the applied bias voltage, αV_B ($\alpha < 1$). The $\alpha(x, y, z)$ parameter (commonly called the lever-arm) depends on the lateral and vertical position of the tip. Consequently, even small tip oscillations modulate α, leading to an effective modulation of the voltage across the barrier. Tunneling of an electron between the back electrode and the Au nanoparticle only takes place if the Coulomb blockade is lifted by selecting a proper value of V_B and tuning $e\alpha V_B$ to one of the electrochemical potential levels of the nanoparticle (Figure 8.1e). Under this condition, the oscillation of α leads to an oscillation of the number of electrons on the nanoparticle, N, between two neighboring ground states characterized by $N = n$ and $N = n + 1$ electrons. The oscillating charge on the nanoparticle causes both a resonance frequency shift, Δf, and damping of the cantilever, $\Delta\gamma$ [70, 71]. Although tunneling of electrons is a stochastic event, the average charge, $\langle N(t)\rangle$, follows the oscillating motion of the tip. As a result, the oscillating electrostatic force has not only an in-phase, but also a 90° out-of-phase component that leads to energy dissipation (which is a similar effect to the Q-factor degradation in the Q-control system used in amplitude modulation AFM [72]). A detailed quantum mechanical treatment of the coupled cantilever-quantum dot system is needed to understand the experimentally observed frequency and dissipation line shapes, which has been explored in detail elsewhere [70, 71].

8.3.1 Coulomb blockade AFM images

We first focus on qualitative observation of the tunneling process by scanning the tip in the area with the three nanoparticles shown in Figure 8.1d in constant height mode with fixed V_B. Figure 8.3 shows a set of dissipation (γ) images recorded at a tip height of ≈8.3 nm (measured from the level of NaCl surface topography characterization) with a fixed bias voltage in the range of 11-13 V. In this situation, although the tip height remains constant (it is only slightly modulated due to the cantilever oscillation amplitude), the lever arm α depends on the relative position with respect to the nanoparticle and decreases monotonically as a function of the tip-nanoparticle distance. If the bias voltage is high enough to induce Coulomb oscillations, dissipation features are visible in the γ images as

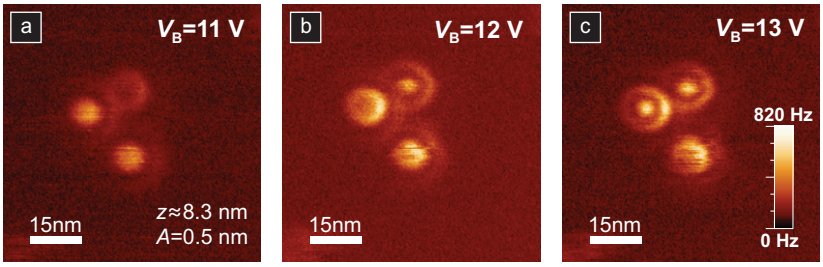

Figure 8.3: Dissipation (γ) images taken at room temperature showing the same three Au nanoparticles as Figure 8.1d, tip height $z \approx 8.3$ nm and cantilever oscillation amplitude $A = 0.5$ nm. The bias voltage across the tunnel barrier, equal to $\alpha(x, y, z)V_B$, was gradually increased by changing V_B from 11 to 13 V, allowing for tunneling of a larger number of electrons.

concentric rings centered above nanoparticles. The circular shape is a consequence of the fact that α, to a good approximation, does not depend on the radial direction with respect to a nanoparticle. Considering a single nanoparticle, during the tip scan $e\alpha V_B$ takes its maximal value at closest approach directly above the nanoparticle. If this maximal value matches exactly one of the electrochemical potential levels, which lifts the Coulomb blockade, a disk-like feature will form in the γ image. When the V_B is further increased, the disk transforms into a ring. The width of this disk (and rings) is well understood and depends amongst other parameters on the oscillation amplitude of the cantilever [70, 71]. Each ring originates from a single peak and indicates the spatial positions of the tip where $e\alpha V_B$ is equal to a particular value that lifts the blockade (the largest ring corresponds to the smallest value of $e\alpha V_B$). As distinctly resolved in Figure 8.3, the size of the nanoparticles is small enough to make the electron addition energy exceed the thermal energy, $k_B T$, since the rings are clearly resolved at room temperature.

The potential drop across the tunnel barrier can also be controlled by changing the tip height while the bias voltage is kept constant. Decreasing the tip height increases all $\alpha(x, y)$ values and leads to a higher potential drop across the tunnel barrier at all lateral tip positions (x, y). If this change is sufficiently large to access further electrochemical potential levels of the nanoparticle, which are separated by E_{add}, more rings are observed in the γ images. This is demonstrated in Figure 8.4a-d, where the tip is brought progressively closer to the sample, starting

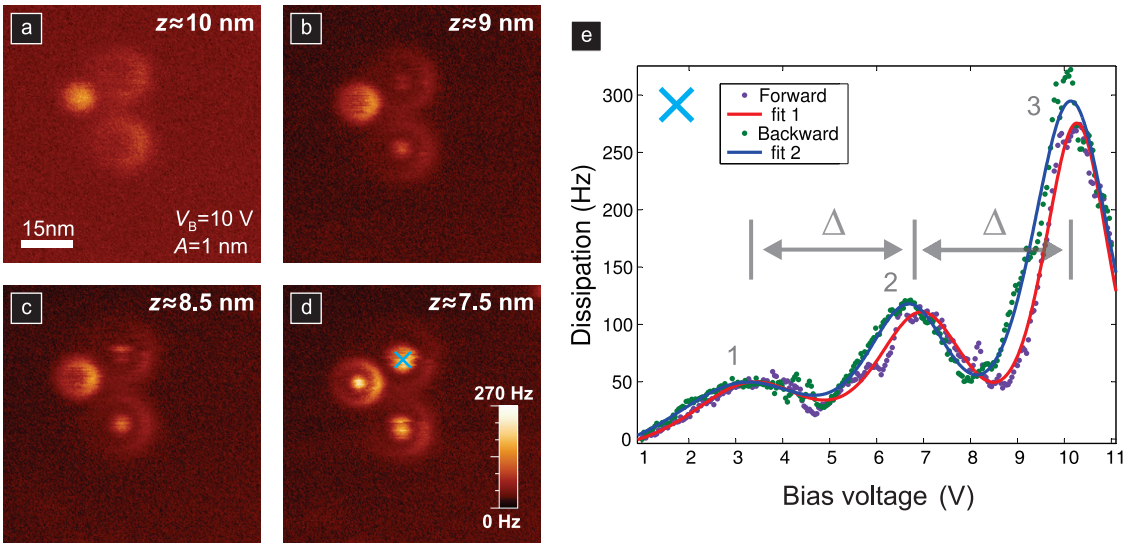

Figure 8.4: (a)-(d) Dissipation images showing sequential unloading of electrons from Au nanoparticles through decreasing the tip height, and thus increasing α. (e) γ-V_{B} spectrum taken at room temperature over the upper nanoparticle with oscillation amplitude $A = 1.0$ nm and tip height $z = 7.5$ nm. Similarly to panel (a), where after entering each ring the number of electrons on the nanoparticle reduces by one, the electrons are sequentially unloaded after increasing V_{B} and passing each peak in the γ-V_{B} spectrum in panel (e). The level arm, α, is determined by a simultaneous fit describing all three peaks using Equation 8.3. The energy difference between the consecutive peaks, Δ, is given by $E_{\mathrm{add}}/e\alpha$, allowing calculation of nanoparticle addition energy.

Parameter	Forward	Backward
α_1	0.030	0.025
α_2	0.039	0.042
α_3	0.054	0.045
γ_1^0 (Hz)	61	68
γ_2^0 (Hz)	119	127
γ_3^0 (Hz)	285	312
V_1^0 (V)	3.35	3.19
V_2^0 (V)	6.97	6.70
V_3^0 (V)	10.27	10.14
Δ_{12} (V)	3.62	3.30
Δ_{23} (V)	3.53	3.44
Offset (Hz)	-12	-20

Table 8.1: Parameters γ_i^0, V_i^0, and α_i obtained during a simultaneous fit of $\sum_{i=1}^{3} \Delta\gamma_i \left(\gamma_i^0, V_i^0, \alpha_i\right)$ to the dissipation data shown in Figure 8.4e.

from 10.0 nm and ending at 7.5 nm, while V_B is fixed at 10 V and the cantilever oscillation amplitude is maintained at 1 nm. Each ring emerges first as a disk above the nanoparticle center and next grows in diameter with decreasing tip height. As the ring diameter gets larger, the intensity of the ring decreases due to the weaker electrostatic damping force at larger tip-nanoparticle distances.

8.3.2 Measurement of electron addition energy

Figure 8.4e shows an electron addition spectrum for the upper nanoparticle imaged in Figure 8.1c (the tip position is also marked with a cross in Figure 8.4d). The γ-V_B spectrum reveals three distinct peaks which correspond to the concentric rings imaged in Coulomb blockade images in Figures 8.3-8.4. The dissipation signal is recorded for positive values of V_B, where single electrons sequentially tunnel out of the nanoparticle with increasing V_B (see Figure 8.1e). If the modulation of $e\alpha V_B$ caused by the cantilever oscillation is smaller than the thermal energy, a condition which is easily met at room temperature, the changes in $\Delta\omega$ and $\Delta\gamma$ are described by a linear response [70, 74, 75]. In this case the shape of the Coulomb

blockade peak is given by [1]:

$$\Delta\gamma(V_{\mathrm{B}}) = \gamma^0 f(\Delta E)\left[1 - f(\Delta E)\right] = \gamma^0 \cosh^{-2}\frac{e\alpha(V_{\mathrm{B}} - V^0)}{2k_{\mathrm{B}}T}, \tag{8.3}$$

where $f(\Delta E)$ is the Fermi function evaluated at the point of charge degeneracy, V^0, and γ^0 is a constant determined by the measurement temperature, parameters of the cantilever and the coupling strength between the tip and the nanoparticle [70]. In the *e*-EFM method Equation 8.3 can be used to extract the α parameter without any knowledge about the tip and sample. The solid fitted lines in Figure 8.4e were obtained by a simultaneous optimization of $\sum_{i=1}^{3}\Delta\gamma_i\left(\gamma_i^0, V_i^0, \alpha_i\right)$, yielding the parameters shown in Table 8.1. On average $\alpha = 0.040$ and E_{add} can be obtained from the separation of consecutive peaks in the γ-V_{B} spectrum being $E_{\mathrm{add}} = e\alpha\Delta_{i,i+1} = e\alpha\left(V_{i+1}^0 - V_i^0\right)$. The addition energy is derived using averaged pairs of α parameters, for example for peaks 1 and 2 E_{add} is calculated as follows:

$$E_{\mathrm{add}} = e\frac{\alpha_1 + \alpha_2}{2}\Delta_{12}. \tag{8.4}$$

This gives four E_{add} values within 110-164 meV recorded for two peaks and both scan directions (forward and backward), which for the nanoparticle under characterization is represented by $E_{\mathrm{add}} = (137 \pm 27)$ meV, confirming that the $E_{\mathrm{add}} \gg k_{\mathrm{B}}T$ requirement is met.

8.3.3 Measurement of tunneling rates

Although in this work we focus on the dissipation signal, a similar addition spectrum was also recorded using the frequency shift, allowing for extraction of tunneling rates. In *e*-EFM the ratio of the two signals, i.e. $\Delta\omega$ and $\Delta\gamma$, is related to

1. The formula is valid for a single-level quantum dot. However, for a many-level quantum dot in the classical limit ($E_{\mathrm{C}} \gg k_{\mathrm{B}}T \gg \Delta E_{\mathrm{level}}$) each Coulomb peak involves many levels in the nanoparticle. Compared to the single-level case, the peak shape is slightly changed and can be still described by a linear response theory. The change is strongest when the tunneling rate is much faster than any other scale, i.e. $\omega \to 0$. In this case, $\Delta\gamma(V_{\mathrm{B}}) \propto \frac{1}{x\coth x}\cosh^{-2} x$, where $x = \frac{e\alpha(V_{\mathrm{B}} - V^0)}{2k_{\mathrm{B}}T}$ [145]. This modification does not significantly change the width of the peak and in the considered case leads to a value of α that is reduced by $\approx 5\%$.

the tunneling rate, Γ [73]:

$$\Gamma = -2\omega\frac{\Delta\omega}{\Delta\gamma}. \tag{8.5}$$

Figure 8.5 shows the frequency shift Δf versus the bias voltage V_{B} measured over the upper nanoparticle simultaneously with the dissipation $\Delta\gamma$ shown in Figure 8.4e (backward direction). To show frequency shift features originating from the tunneling process, a large parabolic background arising from the capacitive force between the tip and the sample has been subtracted. Compared to $\Delta\gamma$, the Δf signal is noisier because of the noise in the background signal. Nevertheless, it is possible to identify three peaks coinciding with the dissipation features observed in Figure 8.4e. Peaks 1-3 have amplitudes of approximately: $\Delta f = 22$, 27, and 200 Hz, respectively. The solid line represents expected theoretical shape of the peaks given by the parameters obtained from the γ-V_{B} spectrum and using a formula equivalent to Equation 8.3 for frequency shift instead of dissipation. Using Equation 8.5 and the parameters γ_i^0 from Table 8.1 we can estimate the tunneling rates $\frac{\Gamma}{2\pi} = 1163$, 764, and 2304 kHz, which are within one order of magnitude of the resonance frequency of the cantilever (approximately 286 kHz).

8.3.4 Finite element electrostatic simulation

Equivalent circuit diagram

Before we can relate the measurement of the addition energy to the capacitance of the nanoparticle and draw an equivalent circuit diagram, we perform electrostatic FEM modeling of the studied system using commercially available COMSOL Multiphysics software (version 4.3a). The considered geometry is depicted in Figure 8.6a, where the nanoparticle is supported on a 6 ML thick NaCl film and its shape is approximated as a solid hemisphere with a radius of 3.5 nm. Above the nanoparticle, at a distance of 8 nm from the NaCl film, there is a metallic tip with a curvature radius of 10 nm (at room temperature heavily doped Si can be approximated by a metal). In total, there are four electrodes: (1) the nanoparticle, (2) the back electrode, (3) the tip, and (4) the system boundary. To calculate the charge distribution and capacitances in COMSOL a built-in physics-controlled mesh generator is used to partition a 2D axisymmetric model. The mesh is fur-

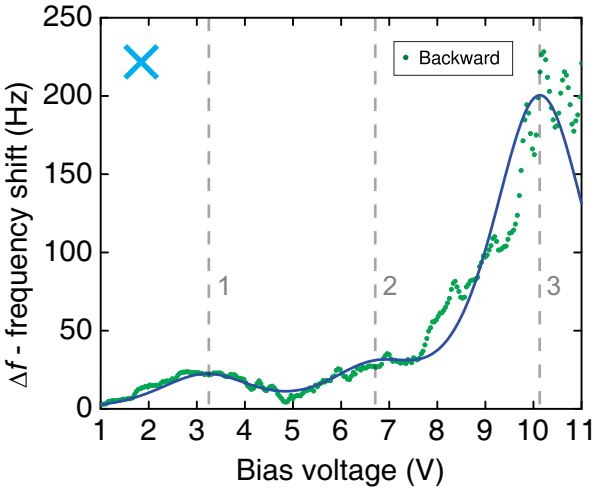

Figure 8.5: The frequency shift Δf versus the bias voltage V_B measured over the upper nanoparticle simultaneously with the dissipation $\Delta\gamma$ that is shown in Figure 8.4e (backward direction). A large parabolic background arising from the capacitive force between the tip and the sample has been subtracted. The dashed lines indicate the position of peaks in the γ-V_B spectrum. The solid line represents expected theoretical shape of the peaks given by the parameters obtained from the γ-V_B spectrum and using a formula equivalent to Equation 8.3 for frequency shift instead of dissipation.

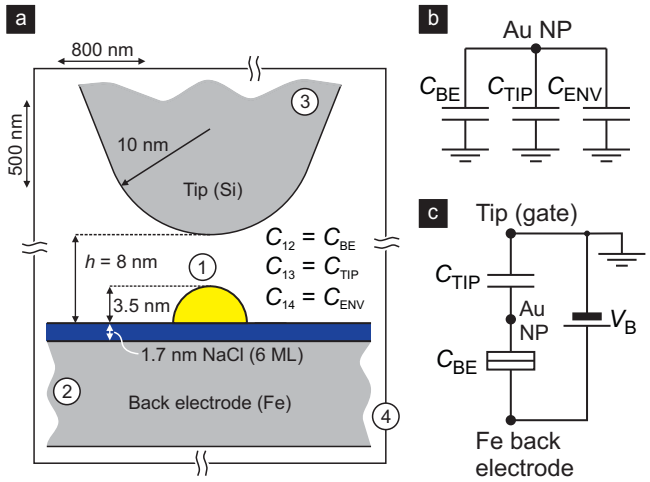

Figure 8.6: (a) FEM geometry for calculating the capacitance components of the nanoparticle (1). (b) Relevant capacitances to the three electrodes: back electrode (2), tip (3), and system boundary (4). (c) Equivalent circuit diagram for an individual nanoparticle.

Tip-sample distance (nm)	C_Σ (aF)	C_{BE} (aF)	C_{TIP} (aF)	C_{ENV} (aF)	α
6	2.15666	2.00342	0.153162	0.000076	0.071018
7	2.14272	2.01670	0.125921	0.000107	0.058767
8	2.13489	2.02785	0.106897	0.000141	0.050071
9	2.12999	2.03710	0.092715	0.000180	0.043528
10	2.12682	2.04491	0.081686	0.000222	0.038408

Table 8.2: Capacitances C_Σ, C_{BE}, C_{TIP} and C_{ENV} for different tip-sample separation in the geometry shown in Figure 8.6a. To show the variation in C_{ENV} the values are presented with more figures following the decimal point than may be significant.

ther refined by increasing the distribution of elements near the nanoparticle and the tip apex. In this way the local element size varies from 0.35 to 2 nm with the highest density around the nanoparticle. All experiments are assumed to occur in vacuum and the relative dielectric constant of NaCl is taken to be 5.9. Figure 8.6b shows three relevant mutual capacitances in this system. We obtain the following calculated capacitances: $C_{12} = C_{\text{BE}} = 2.028$ aF, $C_{13} = C_{\text{TIP}} = 0.107$ aF, $C_{14} = C_{\text{ENV}} < 0.0002$ aF, and the total capacitance of the hemispherical nanoparticle $C_\Sigma = C_{\text{BE}} + C_{\text{TIP}} + C_{\text{ENV}} = 2.135$ aF. The capacitance between the nanoparticle and the system boundary, i.e. the environment, C_{ENV}, which represents the capacitance with respect to a grounded plane at infinity (often called "self-capacitance"), is negligible. Consequently, the circuit diagram can be reduced to a single-electron box, as shown in Figure 8.6c. In this case, $\alpha = C_{\text{TIP}}/C_\Sigma$ with $C_\Sigma = C_{\text{TIP}} + C_{\text{BE}}$ being the total capacitance of the nanoparticle, where the C_{ENV} component is neglected. The calculated values of the capacitances C_{TIP} and C_{BE} yields $\alpha \approx 0.050$, which is in very good agreement with the value obtained experimentally, although the actual nanoparticle and tip shapes may be different. The geometry shown in Figure 8.6a can also be used to calculate the α parameter by applying a voltage bias, e.g. 1 V, to the tip, grounding the back electrode and keeping the nanoparticle charge-neutral at a floating voltage. Still assuming a hemispherical shape, the calculated voltage at the nanoparticle gives in this situation an indistinguishable value from the previously calculated result using the ratio of capacitances.

Numerical simulation of the hemispherical nanoparticle suggests a very

dominant role of C_{BE}, i.e. the mutual capacitance between the nanoparticle and the back electrode in the total capacitance. Most importantly, calculations performed for different tip-sample distances indicate that C_{BE} does not depend strongly on the exact position of the tip that is used in the experiment. Table 8.2 shows the values of capacitances C_{Σ}, C_{BE}, C_{TIP} and C_{ENV} calculated for different tip-sample distances in the geometry shown in Figure 8.6a. Even with a large range of the change in the tip-sample distance, the major contribution to the total capacitance C_{Σ} originates from the mutual capacitance to the back electrode C_{BE}. This capacitance increases only $\approx 2\%$ when the distance is reduced from 10 nm to 6 nm.

A FEM simulation of the capacitance performed for this nanoparticle shape but without the tip leads to a comparable total capacitance of $C_{\Sigma} = C_{\mathrm{BE}} + C_{\mathrm{ENV}} = 2.118$ aF. In this case, the capacitance component due to the system boundary is increased, but is still very small, $C_{\mathrm{ENV}} < 0.007$ aF $\ll C_{\Sigma}$. We found also that C_{ENV} depends weakly on the size of the system in the 100-1000 nm range used in the FEM modeling. C_{BE} can still be accurately calculated in a geometry that is further simplified by neglecting the tip and assuming $C_{\Sigma} \approx C_{\mathrm{BE}}$. The discrepancy is on the order of C_{TIP}, and since $\alpha = C_{\mathrm{BE}}/C_{\Sigma}$ the percentage discrepancy is approximately equal to α, which in this experiment is about 5%.

Modeling the nanoparticle shape

Given the equivalent circuit diagram of a single-electron box, the total capacitance of the nanoparticle can be simply obtained from the experimental value of E_{add} using the relation $E_{\mathrm{add}} = e^2/C_{\Sigma}$, which leads to an experimental (EXP) total capacitance value of $C_{\Sigma}^{\mathrm{EXP}} = (1.16 \pm 0.26)$ aF with $C_{\mathrm{TIP}}^{\mathrm{EXP}} = (0.046 \pm 0.015)$ aF and $C_{\mathrm{BE}}^{\mathrm{EXP}} = (1.11 \pm 0.26)$ aF. Clearly, this is much smaller than $C_{\mathrm{BE}}^{\mathrm{FEM}} \approx 2.14$ aF, i.e. the capacitance calculated for a hemispherical nanoparticle used in the initial approximation above. Increasing the NaCl film thickness from 6 to 7 ML reduces $C_{\mathrm{BE}}^{\mathrm{FEM}}$ only to 1.95 aF, which does not account for the discrepancy between the experimental and calculated capacitances. What turns out to be highly relevant, however, is the contact area between the nanoparticle and the back electrode. Because the height of the nanoparticle is precisely known from the experiment (contrary to the lateral size, which is overestimated by an unknown amount), we can estimate $C_{\mathrm{BE}}^{\mathrm{FEM}}$ for nanoparticles with different contact areas. We assume a truncated sphere as the

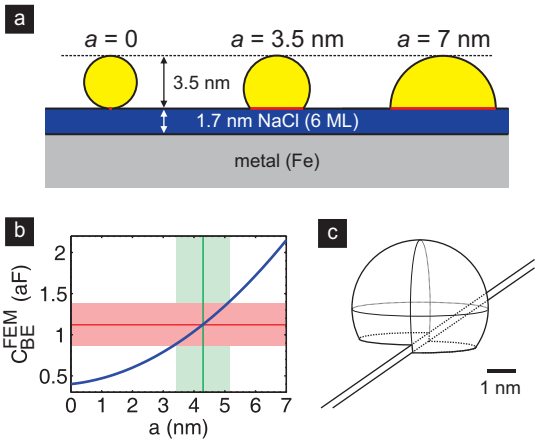

Figure 8.7: (a) Variously shaped nanoparticles supported on a 6 ML thick NaCl film used in capacitance calculations based on FEM. The shape of truncated spheres of constant height (3.5 nm) is parametrized by a describing the diameter of the circular contact area (marked schematically in red). (b) Change in the total capacitance for different a parameters showing that the characterized nanoparticle can be best modeled by a truncated sphere with $a = 4.2$ nm leading to $C_{\mathrm{BE}}^{\mathrm{FEM}} = 1.11$ aF. (c) For a similarly shaped nanoparticle anchored symmetrically above an NaCl step edge (between the 6th and 7th ML) the capacitance is only slightly altered ($C_{\mathrm{BE}}^{\mathrm{FEM}} = 1.13$ aF).

shape of the nanoparticles and calculate $C_{\mathrm{BE}}^{\mathrm{FEM}}$ for different contact areas keeping the same height as shown in Figure 8.7a. The exact shape is parametrized by only one parameter, a, describing the diameter of the circular contact area between the nanoparticle and the NaCl film. The a parameter can take values from 0 to 7 nm and describe intermediate shapes spanning from a sphere to a hemisphere. The values calculated from the FEM modeling are shown in Figure 8.7b and indicate a specific shape of the nanoparticle that correctly describes the experimental results. Compared to the hemispherical nanoparticle, the computationally determined truncated sphere has both a smaller radius, $r = (2.4 \pm 0.3)$ nm, and a smaller contact area with a diameter of $a = (4.2 \pm 0.9)$ nm. In order to take into account the preferential formation of the Au nanoparticles on the step edges on the NaCl film, a corresponding geometry is also modeled (see Figure 8.7c). For a nanoparticle anchored symmetrically above an NaCl step edge, $C_{\mathrm{BE}}^{\mathrm{FEM}}$ is only slightly altered and takes a value of 1.13 aF (the radius is fixed at $r = 2.4$ nm). The determined morphology of the nanoparticle corresponds to a volume of 49 nm^3 containing $\approx$2900 atoms, and is very similar to the equilibrium shape of Au nano- and microstructures on a weakly interacting graphite surface [146, 147]. Interestingly, it also resembles the shape of Au nanoparticles on a more complex, rutile TiO_2(110) surface, which has been characterized by atomic-resolution scanning transmission electron microscopy [10] and grazing incidence x-ray scattering [148].

Calculation of α in 3D

In Figures 8.3 and 8.4, the Coulomb blockade images show rings that correspond to positions of the tip, where α is constant and $e\alpha V_{\mathrm{B}}$ is equal to one of the electrochemical potential levels of the nanoparticle. The spatial function of $\alpha(x, y, z)$ can be obtained from the finite element electrostatic simulation. However, this type of calculation has to be performed incorporating both the the nanoparticle and the tip, which means that the model has to be defined in 3D. This significantly increases the computation burden, setting a limit on the system size. Below we present results from simulations that were performed using a system similar to that in Figure 8.6a that was closed within a cylindrical boundary with a height of of 100 nm, and a diameter of 140 nm (see also Figure 8.8d). We start the analysis from the hemispherical nanoparticle. First, the tip (with an apex radius $r_{\mathrm{T}} = 5$

nm, and a cone semi-angle $\beta = 20°$) is positioned exactly above the nanoparticle, allowing for comparing the 3D model with the 2D axisymmetric model. The α parameter is calculated by applying a voltage bias, e.g. 1 V, to the tip, grounding the back electrode and keeping the nanoparticle charge-neutral at a floating voltage. Figure 8.8a demonstrates that the two models are characterized by a very small discrepancy. Figures 8.8b and c show the dependence of α on the tip distance from the axis of the nanoparticle for various tip structures and tip-sample distances. Using $r_{\mathrm{T}} = 5$ nm and $\beta = 20°$ as representative parameters of the tip, we calculate α vs. the off-axis distance when the tip-sample distance, h, is 8 nm. This corresponds to the separation at which the Coulomb blockade images shown in Figure 8.3 were recorded. If we assume that the electrochemical potential levels of the nanoparticle, which are separated by E_{add}, are also symmetrically positioned with respect to $V_{\mathrm{B}} = 0$ V in the electron addition spectra, then the condition for $e\alpha V_{\mathrm{B}}$ to be equal to one of the electrochemical potential levels can be written as:

$$e\alpha V_{\mathrm{B}} = \left(n + \frac{1}{2}\right) E_{\mathrm{add}}, \tag{8.6}$$

with n being an integer number describing consecutive Coulomb oscillations. This can be rewritten as:

$$\frac{\alpha}{2n+1} = \frac{E_{\mathrm{add}}}{2eV_{\mathrm{B}}}. \tag{8.7}$$

Figure 8.8e shows $\alpha/(2n+1)$ calculated for $n = 0$, 1, 2 and 3. The position of the bold blue line is determined by the value of the right-hand side of Equation 8.7. The intersection between the blue line and the $\alpha/(2n+1)$ lines corresponds to formation of rings in the Coulomb blockade images. By comparing Figure 8.8e to Figure 8.3c recorded at $V_{\mathrm{B}} = 13$ V, where three rings are visible (the weakest ring is still clearly visible in Figure 8.3b), we can draw the bold blue line at a particular height. This gives a rough estimation of $E_{\mathrm{add}}/(2eV_{\mathrm{B}}) \approx 0.009$, and $E_{\mathrm{add}} \approx 234$ meV.

In Figure 8.9 a similar calculation of α for a truncated sphere in the 3D geometry is shown. Compared to the case of the hemispherical nanoparticle, the capacitance between the nanoparticle and the back electrode is reduced, leading to higher values of α. Figure 8.9e shows that the rough estimation of $E_{\mathrm{add}}/(2eV_{\mathrm{B}})$ for a truncated sphere is ≈ 0.012, which leads to $E_{\mathrm{add}} \approx 312$ meV. This is relatively

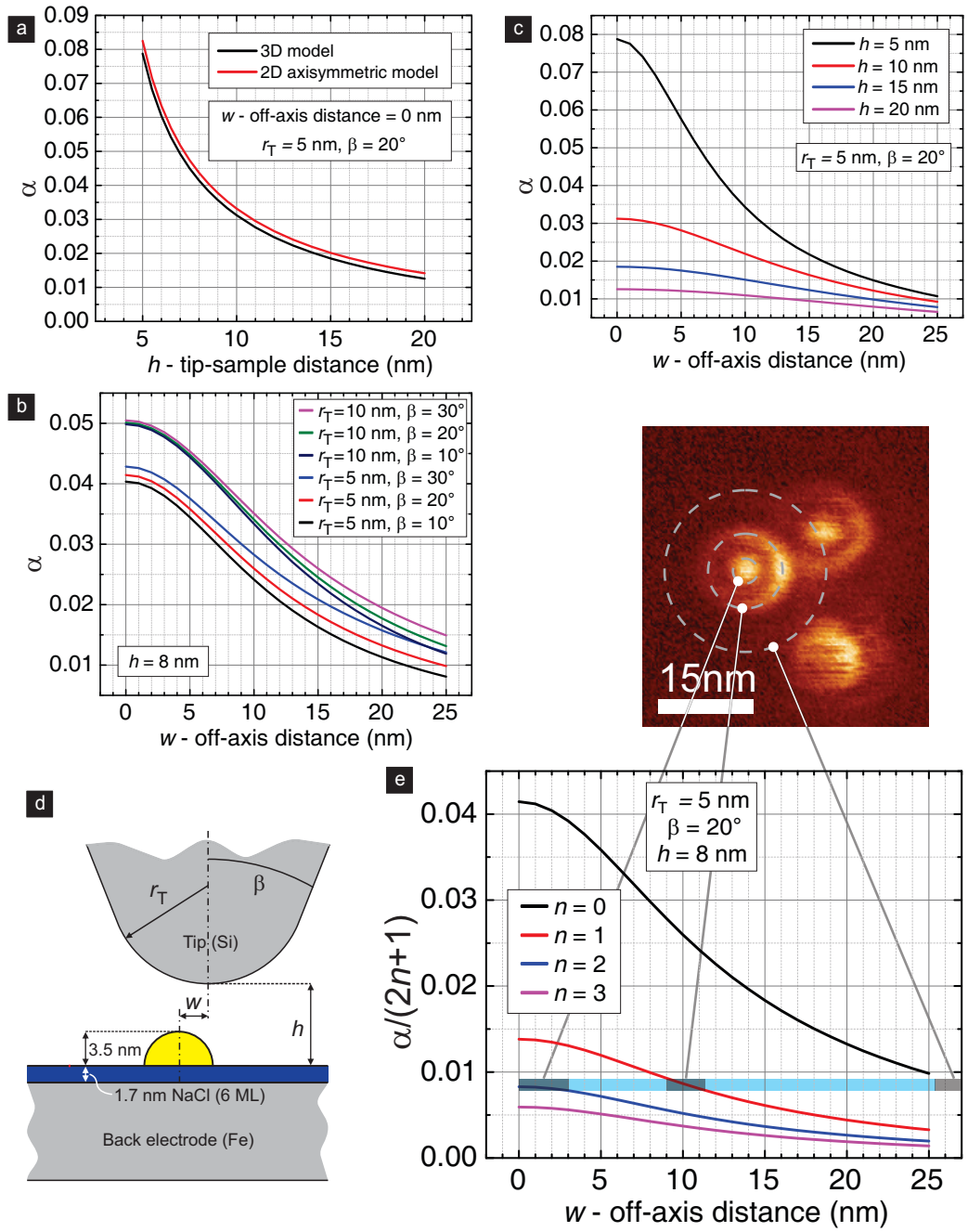

Figure 8.8: Calculation of α for a hemispherical nanoparticle in the 3D geometry shown in (d). (a) Comparison of the 3D and 2D axisymmetric models (with $w = 0$ nm). (b) and (c) Dependence of α on the tip distance from the axis of the nanoparticle for various tip structures (r_T – radius, β – cone semi-angle) and tip-sample distances. (e) Graphical visualization of the condition, when $\alpha/(2n+1) = E_{add}/(2eV_B)$ and the Coulomb blockade is lifted. The intersection between the blue line and the $\alpha/(2n+1)$ lines corresponds to formation of rings in the dissipation images. Comparison to Figure 8.3c (shown in the inset) allows the bold blue line to be drawn at a particular height and E_{add} to be determined.

close to the value extracted directly from the electron addition spectra, and the discrepancy can be accounted for by several factors. First, the assumed height and shape of the tip can differ from the real case. According to Figure 8.9a, the tip height should be ≈ 11 nm in order to model the experimental value of $\alpha = 0.040$, but the calculation in Figure 8.9e was performed for $h = 8$ nm. Second, the electrochemical potential levels of the nanoparticle most likely are not symmetrically positioned with respect to $V_{\mathrm{B}} = 0$ V in the electron addition spectra. The third uncertainty is related to the determination of n for each of the Coulomb oscillations. If the intensity of the first ring is very weak it can be counted incorrectly, leading to wrong evaluation of $E_{\mathrm{add}}/(2eV_{\mathrm{B}})$.

Self-capacitance

The relatively large number of atoms in the nanoparticle justifies the validity of the classical electrodynamics equations used in the FEM calculation, as the number of electrons on the nanoparticle is large enough to consider a continuous distribution of the electrical charge. Similarly, the electron energy level spacing is much smaller than the thermal energy at room temperature, thus corresponding to the classical regime of the Coulomb blockade. In this situation, E_{add} is mostly due to the charging energy of the nanoparticle that is determined by the total capacitance. It is worth mentioning that the self-capacitance of a solid hemisphere with $r = 3.5$ nm in free space calculated analytically [149] is 0.329 aF. This value is significantly larger than the C_{ENV} component ($C_{\mathrm{ENV}} < 0.0002$ aF) calculated above where the hemispherical nanoparticle is supported on an NaCl film. This clearly suggests that the concept of self-capacitance defined as the capacitance with reference to a grounded plane at infinity cannot be used to estimate the total capacitance of the system with nanoparticles coupled to nearby electrodes.

Figure 8.10 illustrates a simple example, where a metal cylinder with a height of 3.5 nm and a diameter of 7 nm is closed within a grounded boundary. In one case, the cylinder is separated from the boundary by a 1.7 nm (6 ML) thick NaCl film (see Figure 8.10a), and in the other is placed centrally without any dielectrics present (see Figure 8.10c). Figure 8.10b shows the capacitance to the boundary calculated as a function of the system size in both situations. When the metal cylinder is placed near the system boundary, as soon as the system size

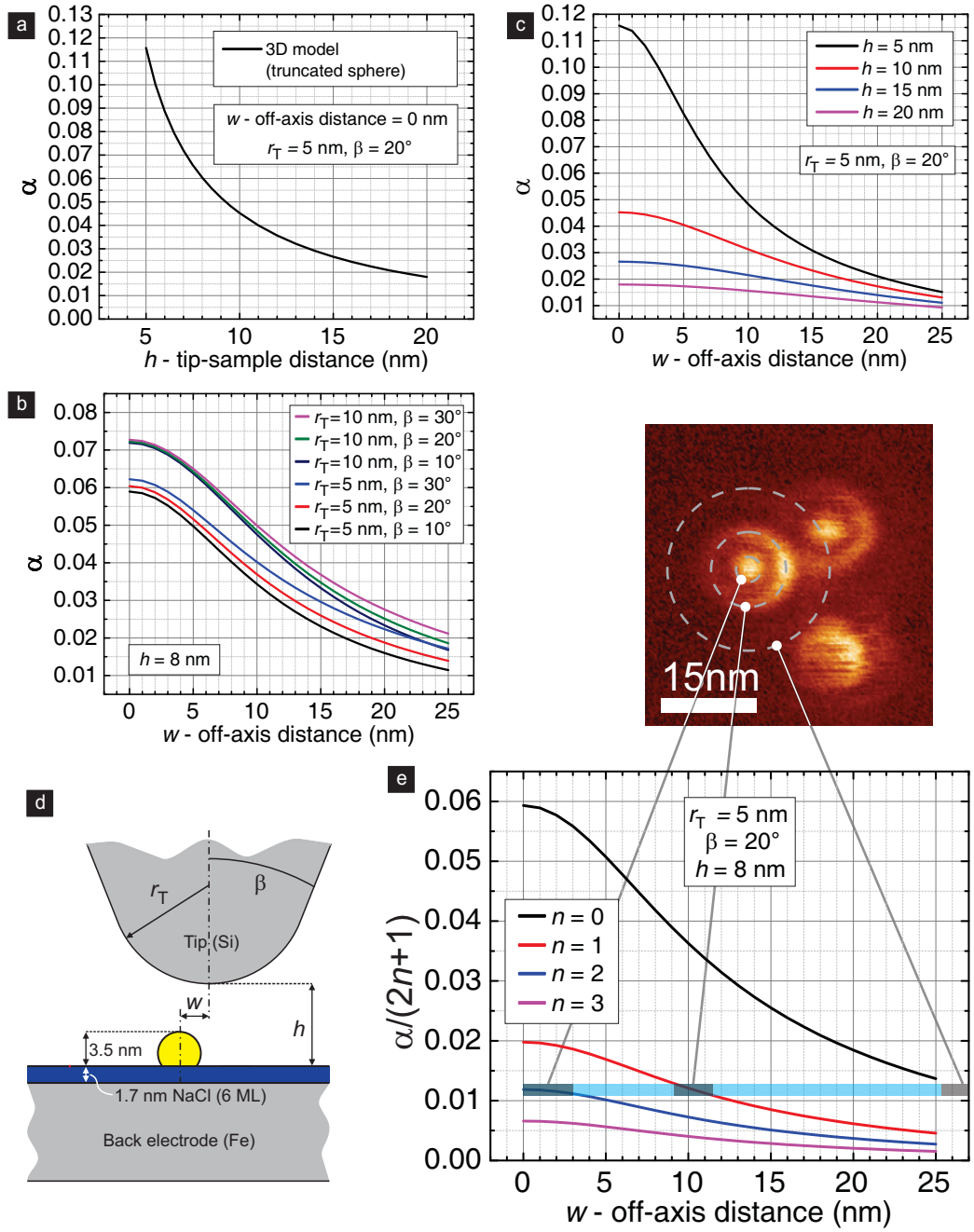

Figure 8.9: Calculation of α for a truncated sphere in the 3D geometry shown in (d) (compare with Figure 8.8). (a) Dependence of α on the tip height (3D model with $w = 0$ nm). (b) and (c) Dependence of α on the tip distance from the axis of the nanoparticle for various tip structures (r_T – radius, β – cone semi-angle) and tip-sample distances. (e) Graphical visualization of the condition, when $\alpha/(2n+1) = E_{add}/(2eV_B)$ and the Coulomb blockade is lifted. Figure 8.3c is shown in the inset for comparison.

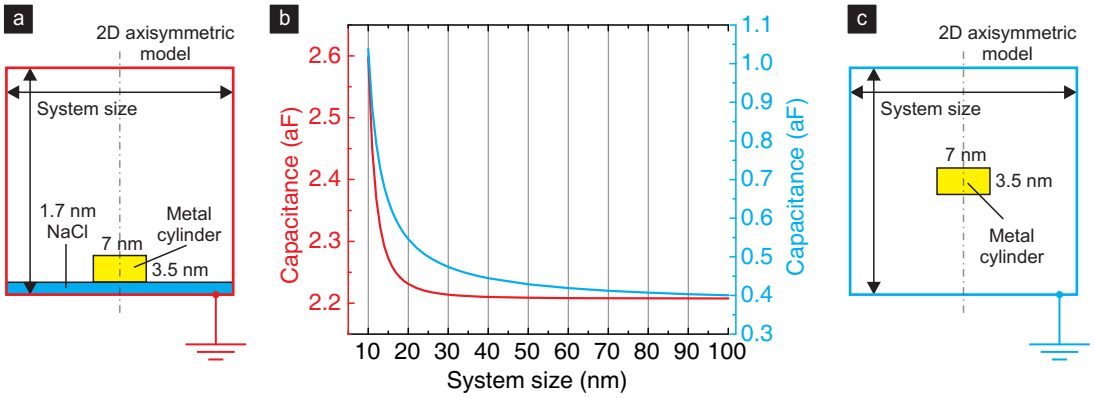

Figure 8.10: A metal cylinder with a height of 3.5 nm and a diameter of 7 nm is closed within a grounded boundary. In (a) the cylinder is separated from the boundary by a 1.7 nm (6 ML) thick NaCl film, and in (c) is placed centrally without any dielectrics present. (b) The capacitance to the boundary calculated as a function of the system size in the two situations.

is larger than 30 nm the capacitance does not change. This is different from the second case, without any dielectric and the cylinder placed centrally, which corresponds to a textbook example for determining self-capacitance of a cylinder (see Section 2.2.2). In this situation, the capacitance to the boundary decays much more slowly and only stabilizes when the system is ≈ 100 nm in size.

It should be noted that the effect of the self-capacitance on single-electron charging has not been sufficiently emphasized in the literature, and its subtle aspects were only discussed by Ohgi *et al.* [150]. In particular, we found that the total capacitance cannot be divided into a fixed self-capacitance component, which is given by the shape of the nanoparticle, and mutual capacitances to the electrodes. These capacitances can still be defined conceptually, but are not additive and do not sum up to the total capacitance of the nanoparticle. This observation has a fundamental impact on the design of nanoelectronic circuits, where the components have to meet desired requirements for capacitances that determine coupling and charging effects [7]. For instance, in our study the total capacitance of the nanoparticle is dominated by the mutual capacitance to the back electrode, which can be primarily controlled by adjusting the contact area between the nanoparticle and the dielectric film.

8.3.5 The *e*-EFM technique and other research areas

Given the fabrication flexibility and the fact that all measurements were performed *in-situ* on samples prepared under ultra-clean conditions, the presented method can be easily extended to other areas of research. The well defined morphology makes the system accessible to various theoretical methods, including density functional theory and molecular dynamics. A variety of nanoscale processes on alkali halide surfaces have been well characterized, such as the self-assembly of metal clusters and large organic molecules [32]. Such detailed understanding makes the fabricated system attractive for further studies. For instance, organic molecules can be used to interconnect two Au nanoparticles [151, 152] and control their mutual capacitance and quantum mechanical interactions. In this way, coherent tunneling in coupled quantum dots [153] could be systematically studied *in-situ*. Our approach is also applicable to studies of model catalysis on various insulating oxide films at temperatures as high as room temperature, as there is a close analogy with the widely-studied system of Au nanoparticles supported on MgO films [6]. Au nanoparticles are known to be a very efficient catalyst that can be active over a wide range of temperatures [154]. The chemical functionality of such metal nanostructures depends crucially on their size and shape, as well as the charge state [155], which can be characterized by *e*-EFM. The size of nanoparticles used in this study is very close to the regime in which Au reveals maximal chemical activity [155]. By shortening the evaporation time this size can be reduced leading to enhanced electronic quantum size effects that play a significant role in oxidation of CO molecules by Au nanoclusters [156]. The *e*-EFM method could be used not only to sense the charge state of individual Au clusters, but also to resolve electronic quantum energy levels and observe changes in frontier orbitals upon interaction with reactants.

8.4 Conclusions

We have demonstrated that by exercising precise control over sample design and growth the *e*-EFM technique can be used to characterize single-electron charging at room temperature. The electron addition energy of a 3.5 nm tall Au nano-

particle supported on a 6 ML thick NaCl film is measured as $E_{\text{add}} = (137 \pm 27)$ meV, which substantially exceeds the thermal energy and allows for observation of Coulomb blockading at room temperature. Electrostatic FEM calculations indicate that the total nanoparticle capacitance is dominated by the mutual capacitance to the back electrode. The modeled nanoparticle shape that best matched our experimental data was a truncated sphere, in which the mutual capacitance to the substrate can be reduced. Flexible *in-situ* fabrication based on well-characterized UHV processing techniques of alkali halide surfaces can extend the *e*-EFM technique to room temperature characterization of other systems on ultra-thin insulating films. In particular, this approach can be used to study quantum mechanically coupled quantum dots and the catalytic activity of Au nanoclusters at room temperature.

9

Conclusions and outlook

9.1 Conclusions

Progress in growth of insulating ultra-thin films

One of the main objectives of this thesis was to grow atomically-perfect tunnel barriers. Considerable progress was made in the growth of epitaxial MgO and NaCl films on Fe(001) surfaces. In the first case, we demonstrated that the quality of MgO films can be improved by using reactive deposition method, which gives control over the gaseous species that reach the sample. We developed a protocol that prevents excessive interfacial reaction between oxygen and the Fe(001) surface, and subsequently provides a sufficient amount of oxygen in order to grow a stoichiometric MgO film. This is done either by reducing the O_2 pressure at the beginning of the growth for a duration needed to grow the 1st MgO ML or depositing a submonolayer coverage of Mg prior to the reactive growth of MgO. The effect of post-annealing and an increased substrate temperature during the growth was studied. In particular, post-annealing of MgO films induces changes in the structure of misfit dislocations and flattening of the interface. Using NC-AFM we demonstrated that the reactive deposition method can produce terraces that have an average size of 10 nm, which is a significant improvement compared to other preparation methods, such as thermal or electron beam evaporation of MgO.

In the second case, the Fe(001)-p(1×1)O surface was used as a substrate to grow high-quality NaCl films, which represent a unique epitaxial system of an alkali halide on a pure metallic substrate. Here, we used the fact that covering the Fe(001) substrate with a monolayer of chemisorbed oxygen changes its properties so as to promote layer-by-layer growth of NaCl films. We have found that at a

submonolayer coverage and temperatures below 145°C NaCl grows as islands of monoatomic-thickness on terraces, while at temperatures above 175°C islands of biatomic-thickness are also formed at substrate step edges. Both types of islands have the same Fe(001)-O[100]||NaCl(001)[110] orientation, leading to a (4×4) superstructure, where the NaCl unit cell is oriented at 45° with respect to the substrate. Interestingly, no c(2×2) superstructure with the NaCl unit cell oriented at 0° has been observed. We account for the preferred structure of the NaCl film by the fact that during formation of the first monolayer, the lattice parameter of the 2D NaCl film is reduced compared to the bulk value and in the (4×4) configuration matches perfectly the Fe(001)-p(1×1)O lattice. The sample temperature during the growth can be used to control and reduce the extended growth of bilayer islands at substrate step edges. Similarly to the MgO case, post-annealing improves the crystallinity of the film. Samples prepared using this procedure, which includes post-annealing at temperatures of about 160 °C reveal atomically flat films with 40-60 nm wide terraces at coverages ranging from 0.75 to 12 ML. They have quality much higher than MgO films grown on Fe(001) surfaces.

Room-temperature single-electron charging detected by *e*-EFM

The reduced number of defects and the layer-by-layer mode of growth of NaCl films have been used to obtain precise control over sample design to fabricate a nanoscale system exhibiting Coulomb blockade at room temperature. This system was characterized by the *e*-EFM technique. The NaCl film acted as a tunnel barrier that can be easily adjusted by modifying the film thickness, and metal nanoparticles, formed by thermally evaporating Au onto the NaCl surface, were used as electron-confining nanostructures. The tunnel barrier could be carefully tuned relative to the cantilever response to achieve maximum sensitivity in the *e*-EFM method. As a result, the electron addition energy of a 3.5 nm tall Au nanoparticle supported on a 6 ML thick NaCl film was determined. The addition energy was measured as $E_{\text{add}} = (137 \pm 27)$ mV, which substantially exceeds the thermal energy and allowed for observation of the Coulomb blockade at room temperature. Using *e*-EFM the tunneling rates were also extracted and found to lie within one order of magnitude of the resonance frequency of the cantilever (≈260 kHz), corresponding to a current of ~ 100 fA.

Capacitance of nanoparticles supported on a dielectric film

Given the simple design of the studied single-electron system, we used finite element electrostatic simulation to examine the relevant contributions to the total nanoparticle capacitance. We found that the capacitance between the nanoparticle and the system boundary, which represents the capacitance with reference to a grounded plane at infinity (often called "self-capacitance"), is negligible. Consequently, the single-electron system is equivalent to a single-electron box and the total capacitance of the nanoparticle can be simply obtained from the experimental value of addition energy, which leads to $C = (1.16 \pm 0.26)$ aF. The FEM results show that the total capacitance is dominated by the mutual capacitance between the nanoparticle and the back electrode. A comparison of the experimentally determined capacitance with numerical simulations indicates that the nanoparticle should be modeled as a truncated sphere. In this geometry the characterized nanoparticle has a radius of $r = (2.4 \pm 0.3)$ nm. The height of the nanoparticle is fixed at 3.5 nm, which was measured using AFM. The determined morphology of the nanoparticle corresponds to a volume of 49 nm^3 containing ≈2900 atoms.

The FEM electrostatic simulations clearly show that the concept of self-capacitance defined as the capacitance with respect to a grounded plane at infinity should be used with caution. Especially, it cannot be used to estimate the total capacitance of the system with nanoparticles coupled to nearby electrodes. We found that the total capacitance cannot be divided into a fixed self-capacitance component, which is given by the shape of the nanoparticle, and mutual capacitances to the electrodes. This result is very important in the design of nanoelectronic circuits, where the components have to meet desired requirements for capacitances that determine coupling and charging effects.

9.2 Outlook

The flexible *in-situ* fabrication based on well-characterized UHV processing techniques of alkali halide surfaces, such as self-assembly of metal clusters and large organic molecules [32] can be used to extend the fabricated nanoscale system to other research areas. Below we discuss some of the future experiments that can

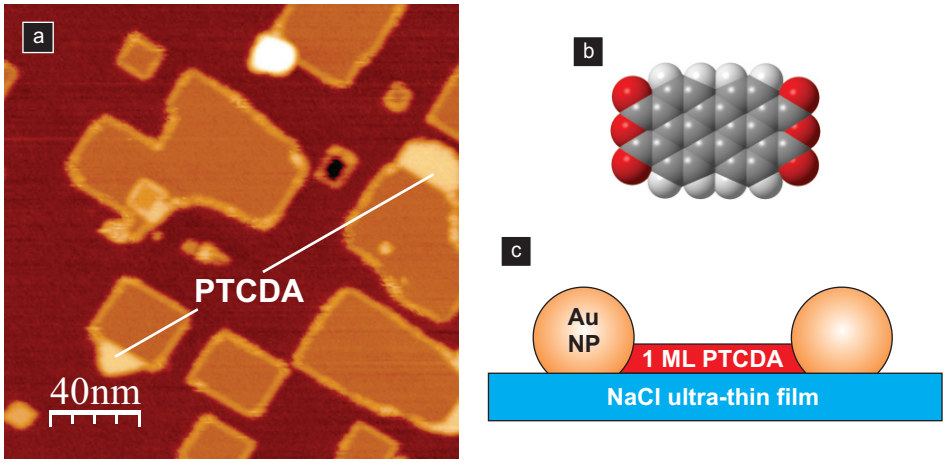

Figure 9.1: (a) An 8 ML thick NaCl film with a submonolayer coverage of PTCDA molecules. (b) A PTCDA molecule. (c) PTCDA molecules can interconnect two Au nanoparticles, which can be used to control the capacitance coupling and quantum mechanical interaction between the nanoparticles.

benefit from the geometry based on an ultra-thin NaCl film.

9.2.1 Controlling the coupling between quantum dots

The *e*-EFM technique can characterize other electronic systems that can be placed on an ultra-thin insulating film. In particular, the demonstrated approach can be used to study coupled Au nanoparticles and nanoclusters. There is a detailed literature of self-assembly of large organic molecules on alkali halide surfaces [32, 152], which can be used to select suitable candidates in order to interconnect the nanoparticles on an ultra-thin NaCl film. As an example, Figure 9.1a shows an 8 ML thick NaCl film with a submonolayer coverage of 3,4,9,10-perylene tetracarboxylic dianhydride (PTCDA) molecules (a PTCDA molecule is shown in Figure 9.1b). In an STM study on partially covered Cu(111) surface with an NaCl film Karacuban *et al.* have shown that PTCDA adsorbs at the step edges of the film in a flat-lying geometry [157]. As schematically presented in Figure 9.1c, in this way the molecules can interconnect two Au nanoparticles and change the mutual capacitance and quantum mechanical interaction between the nanoparticles. A recent theoretical work by Gardner *et al.* has explored the case of an AFM tip ca-

pacitively coupled to a double quantum dot [153]. Compared to a single structure, the system consisting of two coupled nanoparticles or clusters involves significant new physical phenomena. Such a system will respond to the oscillating cantilever not only with oscillation in the total charge, but also with changes in the distribution of a single-electron between the nanoparticles. In particular, surprising new phenomena can arise due to coherent tunneling between the nanoparticles. It has been suggested that the *e*-EFM method could detect coherent interdot tunneling, and extract the value of the intrinsic double quantum dot response time. Using the system fabricated in this thesis and coupling the neighboring Au nanoparticles with organic molecules one could systematically study *in-situ* coherent tunneling in coupled quantum dots both at room and cryogenic temperatures.

9.2.2 A model system for studying catalysis

As mentioned in Section 2.1.4, Au nanoparticles and clusters supported on ultra-thin MgO films reveal exotic charging phenomena [6]. In general, Au nanoparticles are known to be a very efficient catalyst that can be active over a wide range of temperatures [154]. The chemical functionality of such metal nanostructures depends crucially on their size and shape, as well as the charge state [155]. The progress made in this thesis in growing insulating ultra-thin films, which includes NaCl and MgO film, makes the *e*-EFM technique useful for studying catalytic processes relying on supported Au nanoparticles. The size of nanoparticles used in this study is very close to the dimensions at which Au reveals maximal chemical activity [155]. By shortening the evaporation time this size can be reduced leading to enhanced electronic quantum size effects that play a significant role in oxidation of CO molecules by Au nanoclusters [156]. This thesis uses NaCl films due to better quality and reduced complexity of their growth compared to MgO overlayers, but with a larger experimental effort the *e*-EFM characterization can be performed also on MgO films. One could imagine an experiment on individual Au clusters, where the *e*-EFM method can resolve electronic quantum energy levels of a cluster (at room or a cryogenic temperature). After this measurement is obtained, a small amount of CO gas can be introduced into the UHV chamber, which will lead to adsorption of CO molecules on the Au clusters. The

e-EFM method could be used not only to sense the charge state of an individual Au cluster, but also to resolve electronic quantum energy levels and observe changes in frontier orbitals upon interaction with reactants.

As shown in this thesis, a combination of the *e*-EFM technique with electrostatic simulations based on FEM can be used for revealing both electronic and morphological properties of individual Au nanoparticles. In the case of Au on an NaCl ultra-thin film, the approximate shape of an individual nanoparticle is given by a truncated sphere. This information is highly valuable for catalytic studies, where steric effects and presence of facets commonly play very important roles in catalyzing chemical reactions.

9.2.3 Field induced deposition from AFM tips

In this thesis, the electron-confining nanostructures consisted of nanoparticles formed by thermally evaporating Au onto the NaCl surface in UHV. As a result, the Au nanoparticles were, to a large extent, positioned randomly on the surface. It has been demonstrated that NC-AFM with metallic or metal-coated tips can be used for controlled field induced deposition of Au nanodots, which offers an alternative approach to assemble metallic nanoparticles or clusters on the surface of an insulating film. Hosaka *et al.* demonstrated experimentally that Au nanoparticles of 15 nm diameter can be formed on an SiO_2/Si substrate using voltage pulses applied to an AFM cantilever with a threshold of around 10 V [158]. Similarly, Pumarol *et al.* used NC-AFM for reliable deposition of Au dots onto an InP heterostructure (InP/InGaAs/InP) with a two-dimensional electron gas formed in the InGaAs quantum well as the back electrode [159]. Those systems cannot be regarded as atomically-defined, as they either are non-crystalline or are prepared *ex-situ*. Recently, our group has demonstrated that the deposition of Au over bulk monocrystalline insulators prepared in UHV, such as NaCl or KBr, can be feasible through the use of nearby metallic films as a deliberate counter electrode [160].

The system consisting of an ultra-thin NaCl film provides both an atomically-defined interface, and also a back electrode located in the proximity of the AFM tip. In this system the fields are less complicated, compared to the geo-

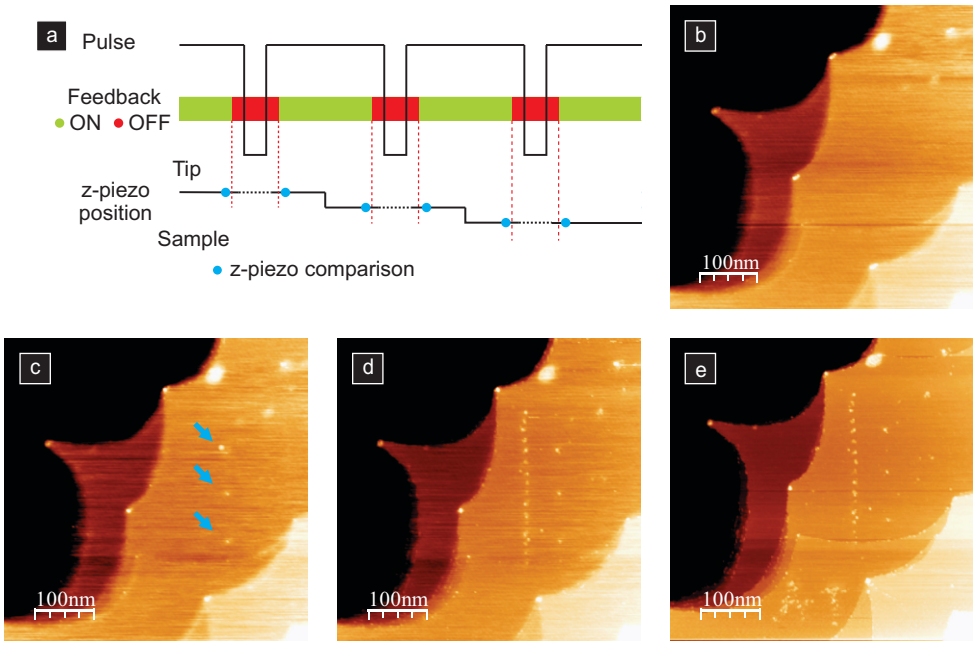

Figure 9.2: (a) Conceptual schematic of the deposition process. Initially the AFM tip is lifted above the substrate by ∼10 nm. Before the pulse is applied, the z-piezo position is measured, and the feedback system is turned off. After the pulse, the feedback is reactivated and the z-piezo position is measured again. If there is no change in the z-piezo position, the tip is brought closer to the substrate, e.g. by 0.5 nm, and the pulse is applied again. This sequence is repeated until optimal conditions for deposition are identified. (b) The Fe(001)-p(1×1)O surface before the deposition. (c) Three deposition attempts are made and after each pulse a protrusion is formed (indicated with arrows). (d) Multiple pulses are applied along a vertical line. (e) The surface is signed with the initials of the author (AT).

metry above a bulk insulator with a side electrode. More importantly, the geometry based on an ultra-thin film helps to achieve higher electric fields at the tip apex, which should make the field induced deposition more reliable.

Initial experiments involving field induced deposition from AFM tips coated with 2 nm of Ti and 100 nm of Au were carried out on the Fe(001) and Fe(001)-p(1×1)O substrates. The idea of the deposition process is depicted in Figure 9.2a. The AFM tip is self-oscillated at a constant amplitude, and is lifted above the substrate by ∼10 nm. The deposition can take place if a pulse with a -10 or $+10$ V bias voltage is applied to the tip. The duration of the pulse is chosen in such a way that the oscillation of the cantilever remains stable. For both SPM controllers used in this work (see Section 4.2) pulses as long as 100 μs did not disturb the cantilever oscillation. Before the pulse is applied, the z-piezo position is measured, and the feedback system is turned off. After the pulse, the feedback is reactivated and the z-piezo position is measured again. If there is no change in the z-piezo position, which suggests no deposition, the tip is brought closer to the substrate, e.g. by 0.5 nm, and the pulse is applied again. This sequence is repeated until optimal conditions for deposition are identified (i.e. the maximum z-height at which deposition can be obtained).

Figures 9.2b-e show modifications of the Fe(001)-p(1×1)O surface after a sequence of pulses with a bias voltage of 11.8 V applied to the tip. Figure 9.2b shows the sample before the deposition. Initially, three voltage pulses were applied over three different sample areas, and Figure 9.2c indicates that after each pulse a protrusion is formed. Next, multiple pulses were applied along a vertical line, which is visible in Figure 9.2d. Ultimately, in Figure 9.2e the surface is signed with the initials of the author (AT). The exact result of applied voltage pulses requires further investigation to prove that the material has been indeed deposited from the tip onto the surface, and exclude e.g. the desorption of oxygen, which can be induced by the pulse and appear as a protrusion in the NC-AFM image due to a variation in LCPD.

Appendix C discusses a clear deposition of Au above the clean Fe(001) surface. Instead of well-defined protrusions, spread-out islands of $\leq$2 ML thickness are formed, which most likely is related to the difference in surface energies of the Fe(001) and Fe(001)-p(1×1)O surfaces. The SEM images of the tip before and

after the deposition show structural changes in the outermost grain involved in the deposition. This points to the importance of preparation of the tips from which the material is deposited. Appendix C also describes an alternative preparation method characterized by higher rigidity of the tip where Au wires of 25 μm diameter are attached to AFM cantilevers and electrochemically etched [161].

9.2.4 Double-electrode AFM probe

Considering the initial results discussed above, it is clear that the deposition of Au from AFM tips over ultra-thin NaCl films could offer a potential path to fabricate conductive nanowires formed by overlapping Au nanodots on the NaCl film. Pumarol *et al.* demonstrated fabrication of such wires on an InP heterostructure that are as long as 55 μm [159]. This method is of potential importance for establishing an interconnection between nanostructures and micrometer-scale electrodes, which is motivated by the needs of future nanoelectronics experiments.

In the first step, a pattern that is several nanometers thick consisting of metallic electrodes separated by a gap can be transfered onto the NaCl film in UHV using stencil masking techniques. This method has been demonstrated by our group using bulk KBr crystals [160, 162]. Next, nanodots from AFM tips could be deposited into the pre-existing gap to form simple nanoscale devices. In order to ultimately connect the structure formed on the surface to an external interface, a double electrical probe can be used. This idea is shown in Figure 9.3a, where a commercially available AFM probe [1] is modified to produce a double-electrode probe. The original AFM probe consisted of a triangular SiN_4 cantilever. Its beam was separated by milling with a focused ion beam (FIB), which is shown in Figures 9.3b and c. The cantilevers were initially coated with Au to avoid charging. One can see that the milling process is difficult, as it creates poorly defined edges and damages the Au coating in the nearby areas. We have also used a surgical scalpel installed on a micromanipulator to cut the triangular SiN_4 cantilevers and quickly separate its beams (see Figure 9.3d). SEM images indicate that this approach can provide results that are comparable with the FIB method. In the final

1. PNP-TR-TL-Au manufactured by Nanoworld with a triangular SiN_4 cantilever that has a very low force constant. The cantilever is supported on an insulating chip made of Pyrex glass. The AFM probes have been provided by Nanoworld without any coating.

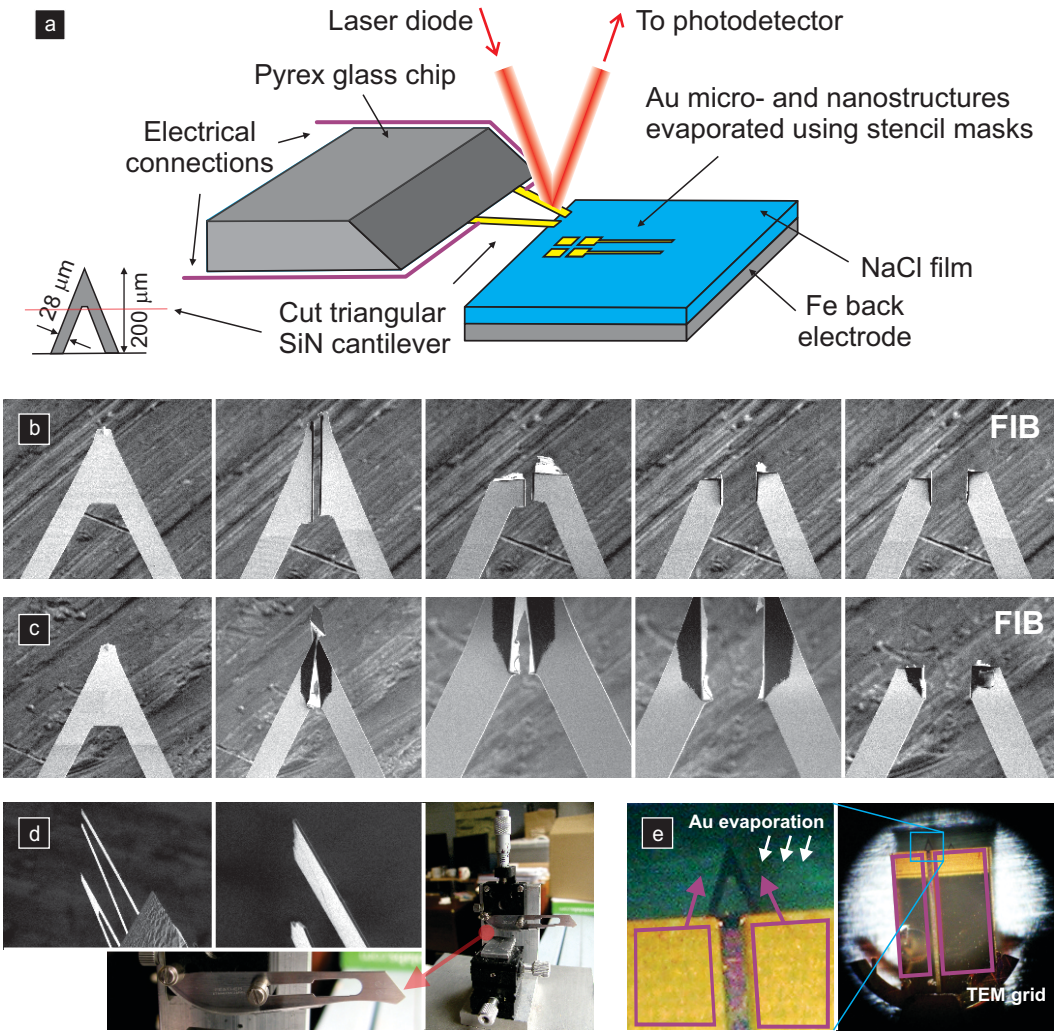

Figure 9.3: (a) A double-electrode AFM probe, which is made of a modified commercial cantilever, can be used to connect the structure formed on the surface to an external interface. A pattern consisting of metallic electrodes separated by a gap can be transfered onto the NaCl film in UHV using stencil masking techniques. This configuration allows for both electronic measurements and detection of the cantilever bending (used to control the amount of pressure applied to the NaCl film). (b) and (c) A triangular SiN_4 cantilever is milled with FIB to separate its beams. The cantilevers were initially coated with Au to avoid charging. The milling process is difficult, as it creates poorly defined edges and damages the Au coating in the nearby areas. (d) A surgical scalpel installed on a micromanipulator is used to cut the triangular SiN_4 cantilever and quickly separate its beams. (e) AFM chip before pattering with Au by thermal evaporation. A cut TEM grid is used as a shadow mask to maintain an open circuit between the beams.

preparation step, the AFM chip has to be patterned with Au in order to provide electrical connection to each of the SiN_4 beams, while maintaining an open circuit between them. As indicated in Figure 9.3e, this can be obtained by using a cut TEM grid as a shadow mask and coating the chip with Au. Such a modified AFM probe can be installed on the JEOL cantilever holder (see Figure 4.4) and microscopic wires can be attached to both electrodes. As shown in Figure 9.3a, this configuration would allow for both electronic measurements and detection of the cantilever bending. The latter could be used to control the amount of pressure applied to the NaCl film.

A

Effect of self-capacitance on single-electron box

In this analysis the self-capacitance, C_{SELF}, is defined as a capacitance with respect to an infinitely distant grounded plane. In the case of a single-electron box the α parameter will depend on the point from which the voltage is referenced, i.e. how the system is grounded. C_{SELF} can be effectively added to the capacitance of either the tunnel barrier (see Figure A.1a) or the gate (see Figure A.1b) by deciding where the ground is connected. We can use the results of the free energy analysis for the single-electron transistor (SET, see Figure A.1c) to understand the impact that the self-capacitance has on the single-electron box. Such derivations can be found in many textbooks, however one has to distinguish two situations: a symmetrically biased SET, and asymmetrically biased SET. In the latter case $V_{\text{S}} = 0$ using the notation shown in Figure A.1c and the conditions to maintain the electron number at n can be expressed as [163]:

$$\left(ne - \frac{e}{2} - C_{\text{G}}V_{\text{G}}\right)\frac{1}{C_{\text{D}}} < V_{\text{D}} < \left(ne + \frac{e}{2} - C_{\text{G}}V_{\text{G}}\right)\frac{1}{C_{\text{D}}}, \tag{A.1}$$

$$\left(-ne + \frac{e}{2} + C_{\text{G}}V_{\text{G}}\right)\frac{1}{C_{\text{S}} + C_{\text{G}}} > V_{\text{D}} > \left(-ne - \frac{e}{2} + C_{\text{G}}V_{\text{G}}\right)\frac{1}{C_{\text{S}} + C_{\text{G}}}. \tag{A.2}$$

Where Inequalities A.1 and A.2 describe Coulomb blockade across the lower and the upper tunnel barrier in Figure A.1c, respectively. If we now substitute:

$$C_{\text{G}}^{\text{SET}} \rightarrow C_{\text{SELF}}^{\text{BOX}},$$

$$C_{\text{D}}^{\text{SET}} \rightarrow C_{\text{G}}^{\text{BOX}},$$

$$C_{\text{S}}^{\text{SET}} \rightarrow C_{\text{T}}^{\text{BOX}},$$

$$V_{\text{D}}^{\text{SET}} \rightarrow V_{\text{B}}^{\text{BOX}},$$

we can describe the single-electron box with the self-capacitance using Inequalities A.1. We can focus only on the tunneling across the lower tunnel barrier, as the gate is only capacitively coupled in the single-electron box and does not allow for tunneling of electrons. In the first case shown in Figure A.1a, when C_{SELF} is added to the capacitance of the tunnel barrier, $V_{\mathrm{G}} = 0$, and the tunneling across the lower tunnel barrier in Figure A.1c is blockaded when:

$$\left(ne - \frac{e}{2}\right)\frac{1}{C_{\mathrm{G}}^{\mathrm{BOX}}} < V_{\mathrm{B}}^{\mathrm{BOX}} < \left(ne + \frac{e}{2}\right)\frac{1}{C_{\mathrm{G}}^{\mathrm{BOX}}}. \tag{A.3}$$

In the second case shown in Figure A.1b, when C_{SELF} is added to the capacitance of the gate, $V_{\mathrm{G}} = V_{\mathrm{D}}$. The tunneling is blockaded when:

$$\left(ne - \frac{e}{2}\right)\frac{1}{C_{\mathrm{G}}^{\mathrm{BOX}} + C_{\mathrm{SELF}}^{\mathrm{BOX}}} < V_{\mathrm{B}}^{\mathrm{BOX}} < \left(ne + \frac{e}{2}\right)\frac{1}{C_{\mathrm{G}}^{\mathrm{BOX}} + C_{\mathrm{SELF}}^{\mathrm{BOX}}}. \tag{A.4}$$

When C_{SELF} is added to the capacitance of the tunnel barrier, in a charge-neutral state the voltage across the tunnel barrier in Figure A.1a is $V_{\mathrm{T}} = V_{\mathrm{B}}^{\mathrm{BOX}} C_{\mathrm{G}}^{\mathrm{BOX}} / (C_{\mathrm{T}}^{\mathrm{BOX}} + C_{\mathrm{G}}^{\mathrm{BOX}} + C_{\mathrm{SELF}}^{\mathrm{BOX}})$. The α parameter expresses the ratio between the voltage across the tunnel barrier and $V_{\mathrm{B}}^{\mathrm{BOX}}$, thus:

$$\alpha = \frac{C_{\mathrm{G}}^{\mathrm{BOX}}}{C_{\mathrm{T}}^{\mathrm{BOX}} + C_{\mathrm{G}}^{\mathrm{BOX}} + C_{\mathrm{SELF}}^{\mathrm{BOX}}} = \frac{C_{\mathrm{G}}^{\mathrm{BOX}}}{C_{\Sigma}^{\mathrm{BOX}}}. \tag{A.5}$$

However, for the situation in Figure A.1b, α understood as the ratio between the voltage across the tunnel barrier and V_{B} is:

$$\alpha = \frac{C_{\mathrm{G}}^{\mathrm{BOX}} + C_{\mathrm{SELF}}^{\mathrm{BOX}}}{C_{\mathrm{T}}^{\mathrm{BOX}} + C_{\mathrm{G}}^{\mathrm{BOX}} + C_{\mathrm{SELF}}^{\mathrm{BOX}}} = \frac{C_{\mathrm{G}}^{\mathrm{BOX}} + C_{\mathrm{SELF}}^{\mathrm{BOX}}}{C_{\Sigma}^{\mathrm{BOX}}}. \tag{A.6}$$

We can rewrite the conditions for the Coulomb blockade in the following way. When C_{SELF} is added to the capacitance of the tunnel barrier:

$$\left(ne - \frac{e}{2}\right)\frac{1}{\alpha C_{\Sigma}^{\mathrm{BOX}}} < V_{\mathrm{B}}^{\mathrm{BOX}} < \left(ne + \frac{e}{2}\right)\frac{1}{\alpha C_{\Sigma}^{\mathrm{BOX}}}. \tag{A.7}$$

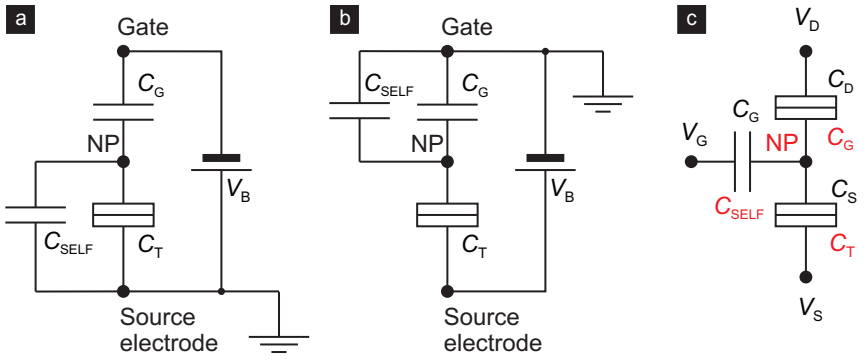

Figure A.1: Concept of the self-capacitance in a single-electron box. The α parameter will depend on the point from which the voltage is referenced, i.e. how the system is grounded. (a) The self-capacitance, C_{SELF}, is added to the capacitance of the tunnel barrier. (b) C_{SELF} is added to the capacitance of the gate. (c) Circuit of a single-electron transistor that can be used to calculate the effect of the self-capacitance on the single-electron box. Corresponding capacitances from panels (a) and (b) are shown in red.

And when C_{SELF} is added to the capacitance of the gate:

$$\left(ne - \frac{e}{2}\right)\frac{1}{\alpha C_{\Sigma}^{\mathrm{BOX}}} < V_{\mathrm{B}}^{\mathrm{BOX}} < \left(ne + \frac{e}{2}\right)\frac{1}{\alpha C_{\Sigma}^{\mathrm{BOX}}}, \tag{A.8}$$

which leads to the same result. In other words, regardless of how the system is grounded, the self-capacitance contributes to the total capacitance of the nanoparticle, $C_{\Sigma}^{\mathrm{BOX}}$, and the Coulomb oscillations are always separated by $\Delta = e/\alpha C_{\Sigma}^{\mathrm{BOX}}$, where α expresses the ratio between the voltage across the tunnel barrier and $V_{\mathrm{B}}^{\mathrm{BOX}}$.

B

Repair of LEED optics (Specs ErLEED)

Figure B.1a shows the condition of LEED optics after extensive contamination with evaporated metals during previous research projects in the JEOL system. The well-defined shape originates from a directional evaporation from the e-beam evaporator, which was partially shadowed by the electron gun of the LEED system (shown in the inset picture in Figure B.1a). In addition, the owned device version was equipped with a faulty retraction mechanism. The manufacturer used linear ball bearings, shown in Figure B.1b, that could not work long under UHV conditions and would cold weld sporadically due to poor lubrication. This design was improved by the manufacturer in later versions, but the cost of upgrading the old device was rather expensive in the range of 4,000 Euro.

As an alternative solution, we decided to replace the linear ball bearings with bearings that can reliably work in UHV. Application of tungsten disulfide coatings as a dry lubricant is a proven technology and bearings coated with such a lubricant are available commercially (MDC Vacuum ALMB-1). Unfortunately, there is a limited choice of linear ball bearings, which are available only for $1/4$" diameter shafts (with $1/2$" outer diameter). Those dimensions differed from the original design (9 mm shaft diameter and 16 mm outer diameter), which required some modifications shown in Figure B.1, panel c and d. The old shafts were removed and replaced with new custom machined shafts that could be mounted in the same way as the old components. Special adapters were also machined to hold the new bearings of a narrower diameter and a shorter height [1].

A new fluorescent screen of correct dimensions (see Figure B.1e) was purchased from Lexel Imaging Systems and exchanged under clean room conditions to avoid any dust particles adhering to the grids of the LEED optics. In order to

1. Machined by Pascal Bourseguin and Francois Poirier.

protect the device from similar contamination in the future, a special shield was installed above the e-beam evaporator, which is shown in Figure B.1f. In this way no material can be deposited onto the LEED device directly from the evaporator. Figure B.1g shows a diffraction pattern recorded on a polycrystalline graphite surface (HOPG) after the repair.

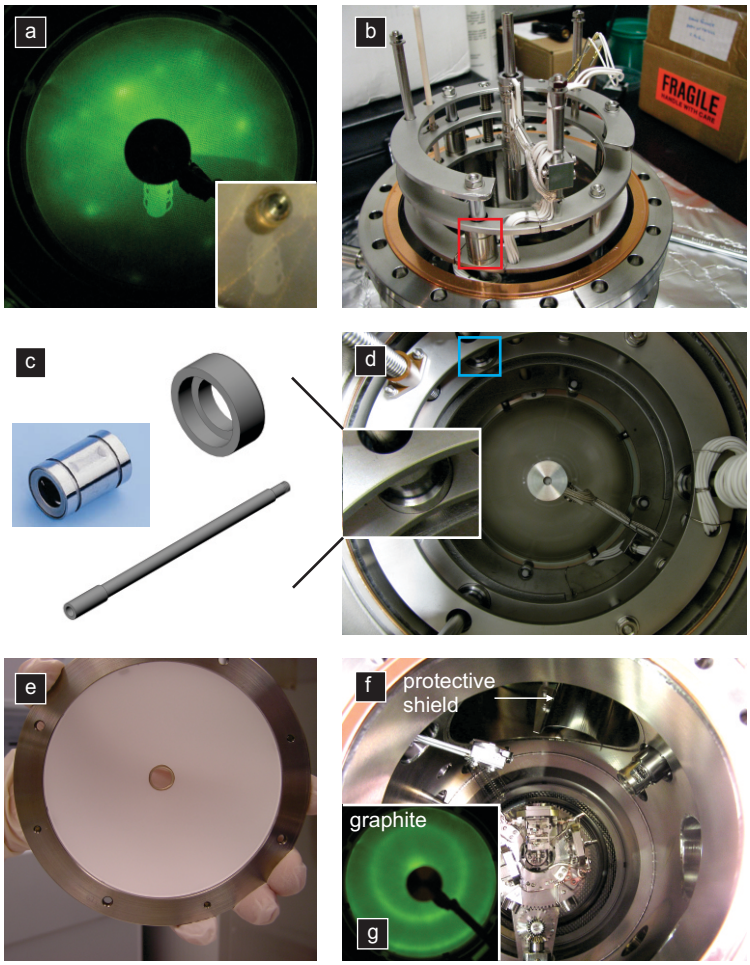

Figure B.1: (a) LEED optics extensively contaminated with evaporated metals. (b) The original retraction mechanism. (c) and (d) New linear ball bearings that required modifications due to smaller dimensions before they could be used in the old design. (e) A new new fluorescent screen before installation in a clean room. (f) A protective shield installed above the e-beam evaporator to protect the LEED optics. (g) A diffraction pattern recorded on a polycrystalline graphite surface (HOPG) after the repair.

C

Field induced deposition from AFM cantilevers

C.1 Deposition onto a clean Fe(001) surface

Figures C.1a-f illustrate field induced deposition from an AFM tip coated with Au onto a clean Fe(001) surface. The circles in Figures C.1b, d and f indicate the position of the AFM tip where a pulse (-10 V, 100μs long) has been previously applied to the tip. As a result, spread-out islands of $\leq$2 ML thickness are formed, which are different from the well-defined protrusions observed on the Fe(001)-p(1$\times$1)O surface. Most likely this change is related to the difference in surface energies of the Fe(001) and Fe(001)-p(1$\times$1)O surfaces. Comparing consecutive images, such as panels b and c, as well as d and e, one can observe spontaneous transfer of Au from the tip that takes place without applying any pulses. The wetting of the Fe(001) surface is caused only by scanning the tip with an oscillating cantilever (in NC-AFM mode). The SEM images of the probe that was used to deposit Au before and after the deposition are shown in Figures C.1g-i and indicate a change in the orientation of the outermost grain that was involved in the deposition.

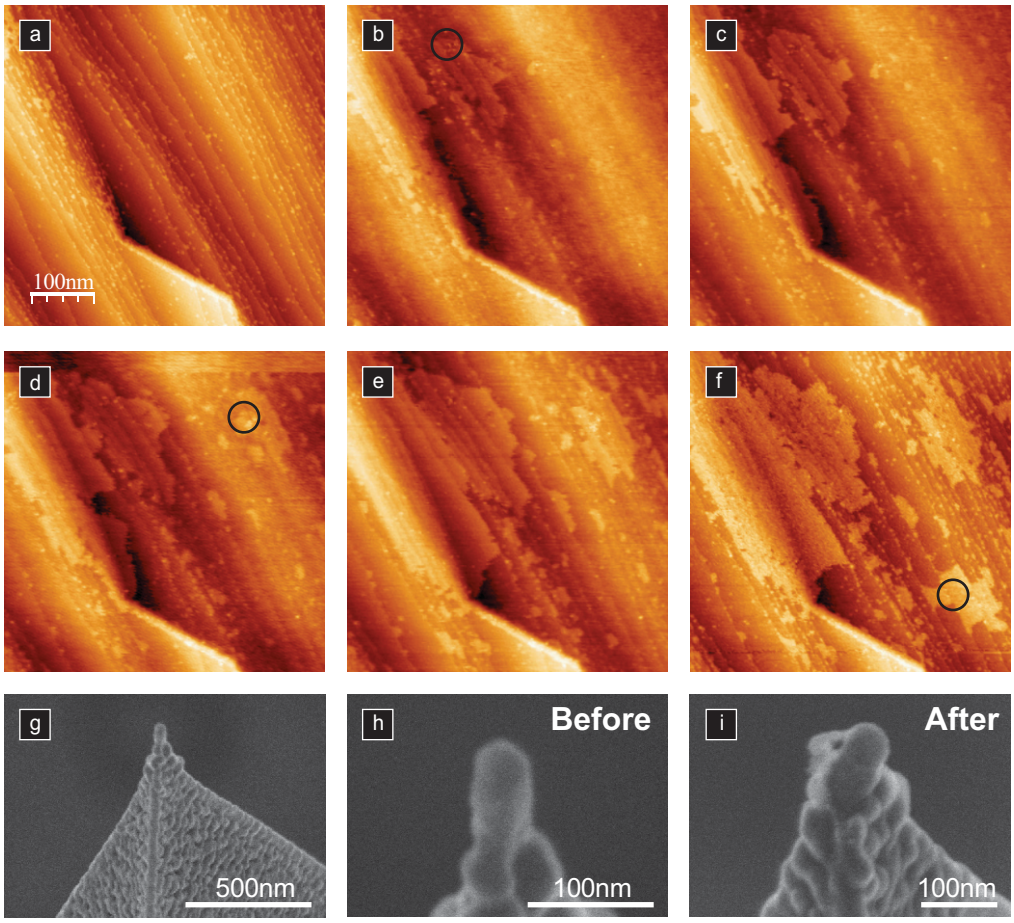

Figure C.1: (a)-(f) Field induced deposition from an AFM tip coated with Au onto a clean Fe(001) surface. The circles in (b), (d) and (f) indicate the position of the AFM tip where a pulse (-10 V, 100μs long applied to the tip) has been previously applied. As a result, spread-out islands of $\leq$2 ML thickness are formed. Comparing consecutive images, such as panels (b) and (c), as well as (d) and (e), one can observe spontaneous transfer of Au from the tip that takes place without applying any pulses. (g)-(i) SEM images of the probe that was used to deposit Au before and after the deposition.

C.2 Cantilevers with metallic tips

Coating commercial AFM cantilevers with 2 nm of Ti and 100 nm of Au by thermal evaporation is a convenient way of preparing tips for the field induced deposition process. However, there is a trade off between the curvature of the apex given usually by the size of the outermost grain, and the rigidity of the tip (Figure C.2d). Small tip radii are important for obtaining electrical field enhancement at the tip, but on the other hand the grain can be weakly bound to the tip. An alternative preparation method characterized by higher rigidity of the tip is shown in Figure C.2a where Au wires of 25 μm diameter are attached to AFM cantilevers and electrochemically etched [161]. The details of this approach have been described by Fostner [164]. The Au wires are cut using a razor blade, and glued to a cantilever using a heat curable epoxy (Epotek H20E). The apex of the cantilever is first dipped into the epoxy using a micromanipulator. Next, the cantilever is approached to the wire positioned over the edge of a glass slide. The success of this method relies on an efficient way of heating the cantilevers. To achieve this, a special cantilever heater was designed that uses a 6.4 mm $\times$ 6.4 mm Kepton insulated flexible heater (MINCO HK5565R10.0L12A) and is shown in Figures C.2a and b. The cantilever chip is installed in an alignment socket (Nanosensors ALIGN) glued to a copper element that is in direct contact with the heater. This setups allows for fast installation and removal of cantilevers, reduces the risk of damaging the probes, and can heat cantilevers to a temperature of 150 °C, at which the epoxy cures within 5-10 minutes.

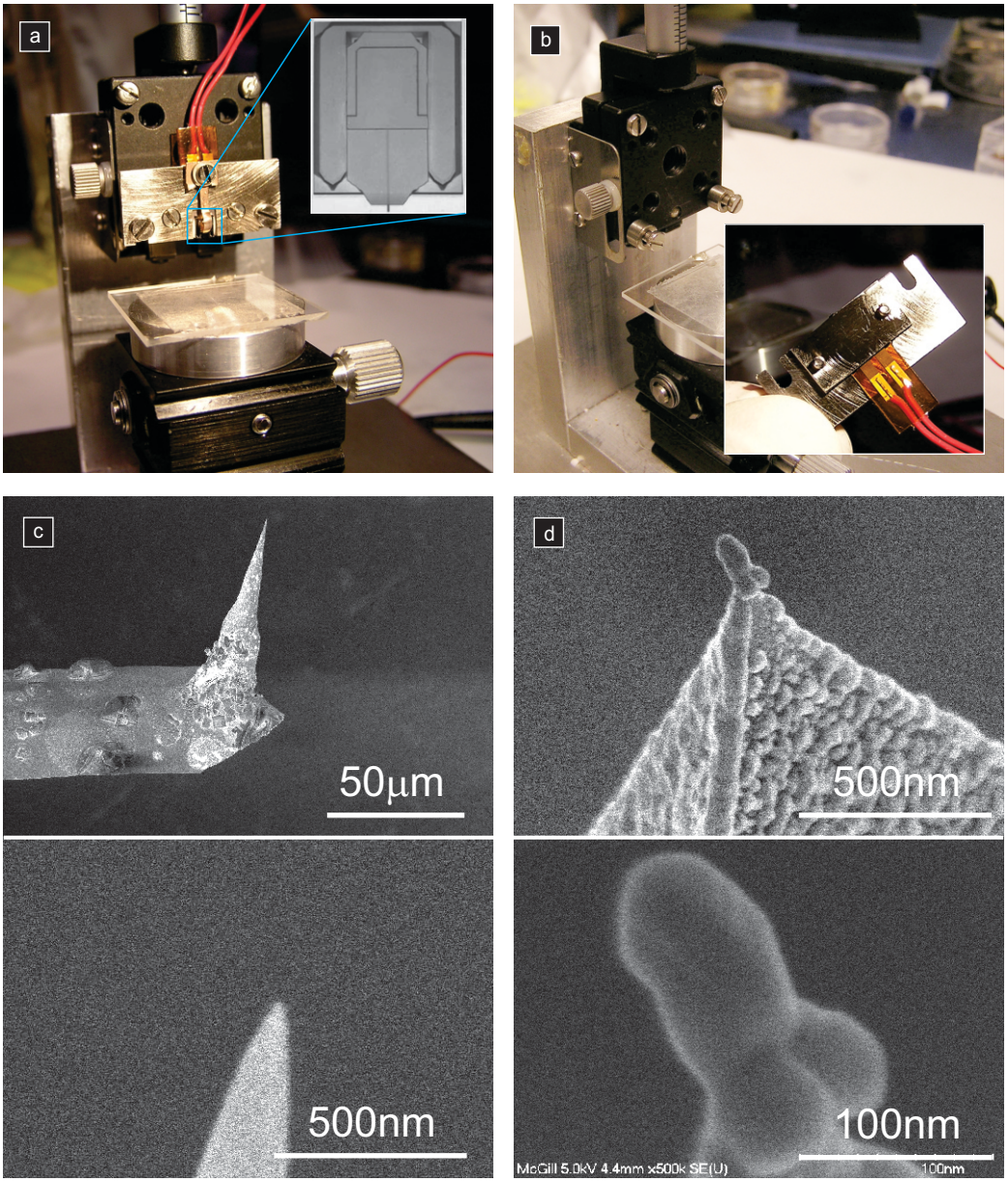

Figure C.2: (a) and (b) A micromanipulator used for attaching and gluing Au wires of 25 μm diameter to commercial AFM cantilevers. The cantilever chip is installed in an alignment socket (Nanosensors ALIGN, shown in the inset) glued to a copper element that is in direct contact with a Kepton insulated flexible heater (MINCO HK5565R10.0L12A). This setups allows for fast installation and removal of cantilevers, which reduces the risk of damaging the probes. (c) Etched Au wire attached to a commercial AFM cantilever using H20E epoxy. (d) A commercial cantilever coated with 2 nm of Ti and 100 nm of Au by thermal evaporation shown for comparison, illustrating that fully metallic tips are characterized by higher rigidity and a higher aspect ratio.

Bibliography

[1] Grünberg, P.; Schreiber, R.; Pang, Y. Layered Magnetic Structures: Evidence for Antiferromagnetic Coupling of Fe Layers across Cr Interlayers. *Physical Review Letters* **1986**, *57*, 2442–2445.

[2] Baibich, M. N.; Broto, J. M.; Fert, A.; Van Dau, F. N.; Petroff, F. Giant Magnetoresistance of (001)Fe/(001)Cr Magnetic Superlattices. *Physical Review Letters* **1988**, *61*, 2472–2475.

[3] Binasch, G.; Grünberg, P.; Saurenbach, F.; Zinn, W. Enhanced magnetoresistance in layered magnetic structures with antiferromagnetic interlayer exchange. *Physical Review B* **1989**, *39*, 4828–4830.

[4] Zhu, J.; Park, C. Magnetic tunnel junctions. *Materials Today* **2006**, *9*, 36–45.

[5] Yuasa, S.; Djayaprawira, D. D. Giant tunnel magnetoresistance in magnetic tunnel junctions with a crystalline MgO(001) barrier. *Journal of Physics D: Applied Physics* **2007**, *40*, R337–R354.

[6] Pacchioni, G., Valeri, S., Eds. *Oxide Ultrathin Films*; Wiley-VCH Verlag GmbH & Co. KGaA: Weinheim, Germany, 2011.

[7] Likharev, K. Single-Electron Devices and their Applications. *Proc. IEEE* **1999**, *87*, 606–632.

[8] Durrani, Z. *Single-electron devices and circuits in silicon*; Imperial College Press: London, UK, 2010.

[9] Ray, V.; Subramanian, R.; Bhadrachalam, P.; Ma, L.-C.; Kim, C.-U.; Koh, S. J. CMOS-Compatible Fabrication of Room-Temperature Single-Electron Devices. *Nature Nanotechnology* **2008**, *3*, 603–608.

[10] Sivaramakrishnan, S.; Wen, J.; Scarpelli, M.; Pierce, B.; Zuo, J.-M. Equilibrium Shapes and Triple Line Energy of Epitaxial Gold Nanocrystals Supported on TiO_2(110). *Physical Review B* **2010**, *82*, 195421.

[11] Barth, J. V. Molecular architectonic on metal surfaces. *Annual Review of Physical Chemistry* **2007**, *58*, 375–407.

[12] Gao, D. Z.; Watkins, M. B.; Shluger, A. L. Transient Mobility Mechanisms of Deposited Metal Atoms on Insulating Surfaces: Pd on MgO (100). *Journal of Physical Chemistry C* **2012**, *116*, 14471–14479.

[13] Lorenzi, G. D.; Ehrlich, G. Energy transfer in atom condensation. *Surface Science Letters* **1993**, *293*, L900–L907.

[14] Venables, J. A. *Introduction to Surface and Thin Film Processes*; Cambridge University Press: Cambridge, 2000.

[15] Barth, J. V.; Costantini, G.; Kern, K. Engineering atomic and molecular nanostructures at surfaces. *Nature* **2005**, *437*, 671–9.

[16] Ehrlich, G. Atomic View of Surface Self-Diffusion: Tungsten on Tungsten. *Journal of Chemical Physics* **1966**, *44*, 1039.

[17] Schwoebel, R. L. Step Motion on Crystal Surfaces. *Journal of Applied Physics* **1966**, *37*, 3682.

[18] Frank, F. C.; van der Merwe, J. H. One-Dimensional Dislocations. I. Static Theory. *Proceedings of the Royal Society A: Mathematical, Physical and Engineering Sciences* **1949**, *198*, 205–216.

[19] Volmer, M.; Weber, A. *Zeitschrift für physikalische Chemie, Stöchiometrie und Verwandtschaftslehre* **1925**, *119*, 277.

[20] Stranski, I.; Krastanov, L. *Abhandlungen der Mathematisch-Naturwissenschaftlichen Klasse. Akademie der Wissenschaften und der Literatur in Mainz* **1939**, *146*, 797.

[21] Bauer, E. Phänomenologische Theorie der Kristallabscheidung an Oberflächen. I. *Zeitschrift für Kristallographie* **1958**, *110*, 372–394.

[22] Diebold, U. The surface science of titanium dioxide. *Surface Science Reports* **2003**, *48*, 53–229.

[23] Barth, C.; Claeys, C.; Henry, C. R. Surface preparation of hard ionic crystals by ultrahigh vacuum cleavage. *Review of Scientific Instruments* **2005**, *76*, 083907.

[24] Wollschläger, J.; Erdös, D.; Schröder, K.-M. The formation of mosaics during the reactive growth of MgO films on Ag(100). *Surface Science* **1998**, *402-404*, 272–276.

[25] Wollschläger, J.; Erdös, D.; Goldbach, H.; Höpken, R.; Schröder, K. Growth of NiO and MgO Films on Ag(100). *Thin Solid Films* **2001**, *400*, 1–8.

[26] Schintke, S.; Messerli, S.; Pivetta, M.; Patthey, F.; Libioulle, L.; Stengel, M.; De Vita, A.; Schneider, W.-D. Insulator at the Ultrathin Limit: MgO on Ag(001). *Physical Review Letters* **2001**, *87*, 276801.

[27] Benedetti, S.; Torelli, P.; Valeri, S.; Benia, H.; Nilius, N.; Renaud, G. Structure and morphology of thin MgO films on Mo(001). *Physical Review B* **2008**, *78*, 1–8.

[28] Dynna, M.; Vassent, J. L.; Marty, A.; Gilles, B. A low-energy electron diffraction investigation of the surface deformation induced by misfit dislocations in thin MgO films grown on Fe(001). *Journal of Applied Physics* **1996**, *80*, 2650.

[29] Klaua, M.; Ullmann, D.; Barthel, J.; Wulfhekel, W.; Kirschner, J.; Urban, R.; Monchesky, T.; Enders, A.; Cochran, J.; Heinrich, B. Growth, structure, electronic, and magnetic properties of MgO/Fe(001) bilayers and Fe/MgO/Fe(001) trilayers. *Physical Review B* **2001**, *64*, 134411.

[30] Parkin, S. S. P.; Kaiser, C.; Panchula, A.; Rice, P. M.; Hughes, B.; Samant, M.; Yang, S.-H. Giant tunnelling magnetoresistance at room temperature with MgO (100) tunnel barriers. *Nature Materials* **2004**, *3*, 862–7.

[31] Vassent, J.; Marty, A.; Gilles, B.; Chatillon, C. Thermodynamic analysis of molecular beam epitaxy of MgO(s) II. Epitaxial growth of MgO layers on Fe(001) substrates. *Journal of Crystal Growth* **2000**, *219*, 444–450.

[32] Gnecco, E.; Szymonski, M. *Nanoscale Processes on Insulating Surfaces*; World Scientific Publishing Co. Pte. Ltd.: Singapore, 2009.

[33] Kolodziej, J.; Such, B.; Czuba, P.; Krok, F.; Piatkowski, P.; Szymonski, M. Scanning-tunneling/atomic-force microscopy study of the growth of KBr films on InSb(001). *Surface Science* **2002**, *506*, 12–22.

[34] Berkowitz, J.; Chupka, W. A. Polymeric Gaseous Molecules in the Vaporization of Alkali Halides. *Journal of Chemical Physics* **1958**, *29*, 653.

[35] Lester, J. E. Studies of the Evaporation Mechanism of Sodium Chloride Single Crystals. *Journal of Chemical Physics* **1968**, *49*, 2940.

[36] Butman, M. F.; Smirnov, A. A.; Kudin, L. S.; Munir, Z. A. Mass Spectrometric Study of the Vaporization Kinetics of Potassium Bromide Single Crystals. *Journal of Materials Synthesis and Processing* **2000**, *8*, 55.

[37] Hebenstreit, W.; Redinger, J.; Horozova, Z.; Schmid, M.; Podloucky, R.; Varga, P. Atomic resolution by STM on ultra-thin films of alkali halides: experiment and local density calculations. *Surface Science* **1999**, *424*, L321–L328.

[38] Bennewitz, R.; Foster, A.; Kantorovich, L.; Bammerlin, M.; Loppacher, C.; Schär, S.; Guggisberg, M.; Meyer, E.; Shluger, A. Atomically resolved edges and kinks of NaCl islands on Cu(111): Experiment and theory. *Physical Review B* **2000**, *62*, 2074–2084.

[39] Repp, J.; Meyer, G.; Rieder, K.-H. Snells Law for Surface Electrons: Refraction of an Electron Gas Imaged in Real Space. *Physical Review Letters* **2004**, *92*, 036803.

[40] Matthaei, F.; Heidorn, S.; Boom, K.; Bertram, C.; Safiei, A.; Henzl, J.; Morgenstern, K. Coulomb attraction during the carpet growth mode of NaCl. *Journal of Physics: Condensed Matter* **2012**, *24*, 354006.

[41] Loppacher, C.; Zerweck, U.; Eng, L. M. Kelvin probe force microscopy of alkali chloride thin films on Au(111). *Nanotechnology* **2004**, *15*, S9–S13.

[42] Pivetta, M.; Patthey, F.; Stengel, M.; Baldereschi, A.; Schneider, W.-D. Local work function Moiré pattern on ultrathin ionic films: NaCl on Ag(100). *Physical Review B* **2005**, *72*, 235423.

[43] Cabailh, G.; Henry, C. R.; Barth, C. Thin NaCl films on silver (001): island growth and work function. *New Journal of Physics* **2012**, *14*, 103037.

[44] Meyer, G.; Gross, L.; Mohn, F.; Repp, J. Scanning probe microscopy of atoms and molecules on insulating films: from imaging to molecular manipulation. *Chimia* **2012**, *66*, 10–5.

[45] Filleter, T.; Paul, W.; Bennewitz, R. Atomic structure and friction of ultrathin films of KBr on Cu(100). *Physical Review B* **2008**, *77*, 1–8.

[46] Le Moal, E.; Müller, M.; Bauer, O.; Sokolowski, M. Misfit driven azimuthal orientation of NaCl domains on Ag(100). *Surface Science* **2009**, *603*, 2434–2444.

[47] Avouris, P.; Wolkow, R. Scanning tunneling microscopy of insulators: CaF_2 epitaxy on Si (111). *Applied Physics Letters* **1989**, *55*, 1074.

[48] Klust, A.; Ohta, T.; Bostwick, A.; Yu, Q.; Ohuchi, F.; Olmstead, M. Atomically resolved imaging of a CaF bilayer on Si(111): Subsurface atoms and the image contrast in scanning force microscopy. *Physical Review B* **2004**, *69*, 035405.

[49] Glöckler, K.; Sokolowski, M.; Soukopp, A.; Umbach, E. Initial growth of insulating overlayers of NaCl on Ge(100) observed by scanning tunneling microscopy with atomic resolution. *Physical Review B* **1996**, *54*, 7705–7708.

[50] Simic-Milosevic, V.; Heyde, M.; Lin, X.; König, T.; Rust, H.-P.; Sterrer, M.; Risse, T.; Nilius, N.; Freund, H.-J.; Giordano, L.; Pacchioni, G. Charge-induced formation of linear Au clusters on thin MgO films: Scanning tunneling microscopy and density-functional theory study. *Physical Review B* **2008**, *78*, 235429.

[51] Yulikov, M.; Sterrer, M.; Heyde, M.; Rust, H.-P.; Risse, T.; Freund, H.-J.; Pacchioni, G.; Scagnelli, A. Binding of Single Gold Atoms on Thin MgO(001) Films. *Physical Review Letters* **2006**, *96*, 146804.

[52] Lin, X.; Yang, B.; Benia, H.-M.; Myrach, P.; Yulikov, M.; Aumer, A.; Brown, M. A.; Sterrer, M.; Bondarchuk, O.; Kieseritzky, E.; Rocker, J.; Risse, T.; Gao, H.-J.; Nilius, N.; Freund, H.-J. Charge-mediated adsorption behavior of CO on MgO-supported Au clusters. *Journal of the American Chemical Society* **2010**, *132*, 7745–9.

[53] Giordano, L.; Cinquini, F.; Pacchioni, G. Tuning the surface metal work function by deposition of ultrathin oxide films: Density functional calculations. *Physical Review B* **2006**, *73*, 045414.

[54] Goniakowski, J.; Noguera, C. Electronic States and Schottky Barrier Height at Metal/MgO(100) Interfaces. *Interface Science* **2004**, *12*, 93–103.

[55] Prada, S.; Martinez, U.; Pacchioni, G. Work function changes induced by deposition of ultrathin dielectric films on metals: A theoretical analysis. *Physical Review B* **2008**, *78*, 235423.

[56] Yuasa, S.; Nagahama, T.; Fukushima, A.; Suzuki, Y.; Ando, K. Giant room-temperature magnetoresistance in single-crystal Fe/MgO/Fe magnetic tunnel junctions. *Nature Materials* **2004**, *3*, 868–71.

[57] Nilius, N.; Kulawik, M.; Rust, H.-P.; Freund, H.-J. Quantization of electronic states in individual oxide-supported silver particles. *Surface Science* **2004**, *572*, 347–354.

[58] Gross, L.; Mohn, F.; Liljeroth, P.; Repp, J.; Giessibl, F. J.; Meyer, G. Measuring the charge state of an adatom with noncontact atomic force microscopy. *Science* **2009**, *324*, 1428–31.

[59] Loth, S.; Baumann, S.; Lutz, C. P.; Eigler, D. M.; Heinrich, A. J. Bistability in atomic-scale antiferromagnets. *Science* **2012**, *335*, 196–9.

[60] Ashcroft, N. *Solid State Physics*; Holt Rinehart and Winston: New York, 1976.

[61] Kulik, I.; Shekhter, R. Kinetic phenomena and charge discreteness effects in granulated media. *Soviet Journal of Experimental and Theoretical Physics* **1975**, *41*, 308–316.

[62] Purcell, E. *Electricity and Magnetism*, 2nd ed.; McGraw-Hill: New York, 1985.

[63] *COMSOL Multiphysics User's Guide ver. 4.3*; 2012.

[64] *COMSOL Multiphysics Reference Guide ver. 4.3*; 2012.

[65] Giessibl, F. J. A direct method to calculate tipsample forces from frequency shifts in frequency-modulation atomic force microscopy. *Applied Physics Letters* **2001**, *78*, 123.

[66] Giessibl, F. J. Advances in atomic force microscopy. *Reviews of Modern Physics* **2003**, *75*, 949–983.

[67] Hudlet, S.; Saint Jean, M.; Guthmann, C.; Berger, J. Evaluation of the capacitive force between an atomic force microscopy tip and a metallic surface. *The European Physical Journal B* **1998**, *2*, 5–10.

[68] Giessibl, F. J.; Hembacher, S.; Herz, M.; Schiller, C.; Mannhart, J. Stability considerations and implementation of cantilevers allowing dynamic force microscopy with optimal resolution: the qPlus sensor. *Nanotechnology* **2004**, *15*, S79–S86.

[69] Sadewasser, S. *Kelvin probe force microscopy measuring and compensating electrostatic forces*; Springer-Verlag: Berlin/Heidelberg/New York, 2012.

[70] Cockins, L.; Miyahara, Y.; Bennett, S. D.; Clerk, A. A.; Studenikin, S.; Poole, P.; Sachrajda, A.; Grutter, P. Energy Levels of Few-Electron Quantum Dots Imaged and Characterized by Atomic Force Microscopy. *Proceedings of the National Academy of Sciences of the United States of America* **2010**, *107*, 9496–9501.

[71] Bennett, S. D.; Cockins, L.; Miyahara, Y.; Grütter, P.; Clerk, A. A. Strong Electromechanical Coupling of an Atomic Force Microscope Cantilever to a Quantum Dot. *Physical Review Letters* **2010**, *104*, 017203.

[72] Sulchek, T.; Hsieh, R.; Adams, J. D.; Yaralioglu, G. G.; Minne, S. C.; Quate, C. F.; Cleveland, J. P.; Atalar, A.; Adderton, D. M. High-Speed Tapping Mode Imaging with Active Q Control for Atomic Force Microscopy. *Applied Physics Letters* **2000**, *76*, 1473–1475.

[73] Zhu, J.; Brink, M.; McEuen, P. L. Single-Electron Force Readout of Nanoparticle Electrometers Attached to Carbon Nanotubes. *Nano Letters* **2008**, *8*, 2399–2404.

[74] Clerk, A. Quantum-Limited Position Detection and Amplification: A Linear Response Perspective. *Physical Review B* **2004**, *70*, 245306.

[75] Clerk, A. A.; Bennett, S. Quantum Nanoelectromechanics with Electrons, Quasi-Particles and Cooper Pairs: Effective Bath Descriptions and Strong Feedback Effects. *New Journal of Physics* **2005**, *7*, 238–238.

[76] Henzler, M. In *Electron Spectroscopy for Surface Analysis*; Ibach, H., Ed.; Topics in Current Physics; Springer Verlag: Berlin/Heidelberg, 1977; Vol. 4; pp 117–149.

[77] Henzler, M. Capabilitties of LEED for defect analysis. *Surface Review and Letters* **1997**, *04*, 489–500.

[78] McMaster, W.; Del Grande, N.; Mallett, J.; Hubbell, J. *Compilation of X-Ray Cross Sections - Lawrence Livermore National Laboratory Report UCRL-50174.*

[79] Kassies, R.; van der Werf, K. O.; Bennink, M. L.; Otto, C. Removing interference and optical feedback artifacts in atomic force microscopy measurements by application of high frequency laser current modulation. *Review of Scientific Instruments* **2004**, *75*, 689.

[80] Fukuma, T.; Kimura, M.; Kobayashi, K.; Matsushige, K.; Yamada, H. Development of low noise cantilever deflection sensor for multienvironment frequency-modulation atomic force microscopy. *Review of Scientific Instruments* **2005**, *76*, 053704.

[81] Chipman, J. Thermodynamics and phase diagram of the Fe-C system. *Metallurgical Transactions* **1972**, *3*, 55–64.

[82] Kirschner, J. Polarized electron diffraction from clean and adsorbate covered Fe (110). *Surface Science* **1984**, *138*.

[83] Parihar, S. S.; Meyerheim, H. L.; Mohseni, K.; Ostanin, S.; Ernst, A.; Jedrecy, N.; Felici, R.; Kirschner, J. Structure of O/Fe(001)-p(1×1) studied by surface x-ray diffraction. *Physical Review B* **2010**, *81*, 075428.

[84] Hejnal, T.; Kadecková, S.; Novak, V.; Šesták, B. Purification of iron to low carbon and nitrogen contents by annealing. *Czechoslovak Journal of Physics B* **1977**, *27*, 1263.

[85] Jordan, S. M.; Lawler, J. F.; Schad, R.; van Kempen, H. Growth temperature dependence of the magnetic and structural properties of epitaxial Fe layers on MgO(001). *Journal of Applied Physics* **1998**, *84*, 1499.

[86] Prinz, G. A. Molecular beam epitaxial growth of single-crystal Fe films on GaAs. *Applied Physics Letters* **1981**, *39*, 397.

[87] Brenner, S. S. Tensile Strength of Whiskers. *Journal of Applied Physics* **1956**, *27*, 1484.

[88] Bhadeshia, H. K. D. H. Bulk nanocrystalline steel. *Ironmaking & Steelmaking* **2005**, *32*, 405–410.

[89] Gardner, R. Controlled growth of α-Fe single crystal whiskers. *Journal of Crystal Growth* **1978**, *43*, 425–432.

[90] Wayman, C. M. Observations on the Growth of α-Iron Single Crystals by Halogen Reduction. *Journal of Applied Physics* **1961**, *32*, 1844.

[91] Weast, R. C., Ed. *CRC Handbook of Chemistry and Physics*, 56th ed.; CRC Press: Cleveland, OH, 1975.

[92] Sears, G. A growth mechanism for mercury whiskers. *Acta Metallurgica* **1955**, *3*, 361.

[93] Gorsuch, P. D. On the Crystal Perfection of Iron Whiskers. *Journal of Applied Physics* **1959**, *30*, 837.

[94] Wagner, R. S.; Ellis, W. C. Vapor-Liquid-Solid Mechanism of Single Crystal Growth. *Applied Physics Letters* **1964**, *4*, 89.

[95] Webb, W. W.; Riebling, E. F. On the Growth of Metal Whiskers by Hydrogen Reduction of Halides. *Journal of Chemical Physics* **1958**, *28*, 1242.

[96] Tange, A.; Gao, C. L.; Yavorsky, B. Y.; Maznichenko, I. V.; Etz, C.; Ernst, A.; Hergert, W.; Mertig, I.; Wulfhekel, W.; Kirschner, J. Electronic structure and spin polarization of the Fe(001)-p(1$\times$1)O surface. *Physical Review B* **2010**, *81*, 1–6.

[97] Cattoni, A.; Petti, D.; Brivio, S.; Cantoni, M.; Bertacco, R.; Ciccacci, F. MgO/Fe(001) and MgO/Fe(001)-p(1$\times$1)O interfaces for magnetic tunnel junctions: A comparative study. *Physical Review B* **2009**, *80*, 104437.

[98] Butler, W.; Zhang, X.-G.; Schulthess, T.; MacLaren, J. Spin-dependent tunneling conductance of Fe—MgO—Fe sandwiches. *Physical Review B* **2001**, *63*, 054416.

[99] Mathon, J.; Umerski, A. Theory of tunneling magnetoresistance of an epitaxial Fe/MgO/Fe(001) junction. *Physical Review B* **2001**, *63*, 220403(R).

[100] Mizuguchi, M.; Suzuki, Y.; Nagahama, T.; Yuasa, S. Microscopic structures of MgO barrier layers in single-crystal Fe/MgO/Fe magnetic tunnel junctions showing giant tunneling magnetoresistance. *Applied Physics Letters* **2006**, *88*, 251901.

[101] Tegenkamp, C.; Michailov, M.; Wollschläger, J.; Pfnür, H. Growth and surface alloy formation of Mg on Ag(100). *Applied Surface Science* **1999**, *151*, 40–48.

[102] Zhang, X.-G.; Butler, W.; Bandyopadhyay, A. Effects of the iron-oxide layer in Fe-FeO-MgO-Fe tunneling junctions. *Physical Review B* **2003**, *68*, 092402.

[103] Bose, P.; Ernst, A.; Mertig, I.; Henk, J. Large reduction of the magnetoresistance in Fe/MgO/Fe tunnel junctions due to small oxygen concentrations at a single FeO interface layer: A first-principles study. *Physical Review B* **2008**, *78*, 092403.

[104] Blonski, P.; Kiejna, A.; Hafner, J. Dissociative adsorption of O_2 molecules on O-precovered Fe(110) and Fe(100): Density-functional calculations. *Physical Review B* **2008**, *77*, 1–8.

[105] Bonell, F.; Andrieu, S.; Bataille, A.; Tiusan, C.; Lengaigne, G. Consequences of interfacial Fe-O bonding and disorder in epitaxial Fe/MgO/Fe(001) magnetic tunnel junctions. *Physical Review B* **2009**, *79*, 1–10.

[106] Wilson, I. Magnesium oxide as a high-temperature insulant. *IEE Proceedings A Physical Science, Measurement and Instrumentation, Management and Education, Reviews* **1981**, *128*, 159.

[107] Oh, H.; Lee, S. B.; Seo, J.; Min, H. G.; Kim, J.-S. Chemical structure of the interface between MgO films and Fe(001). *Applied Physics Letters* **2003**, *82*, 361.

[108] Müller, M.; Matthes, F.; Schneider, C. M. Spin polarization at ferromagnet-insulator interfaces: The important role of stoichiometry in MgO/Fe(001). *Europhysics Letters (EPL)* **2007**, *80*, 17007.

[109] Müller, M.; Matthes, F.; Schneider, C. M. Photoemission study of the Fe(001)/MgO interface for varying oxidation conditions of magnesium oxide. *Journal of Applied Physics* **2007**, *101*, 09G519.

[110] Dugerjav, O.; Kim, H.; Seo, J. M. Growth of a crystalline and ultrathin MgO film on Fe(001). *AIP Advances* **2011**, *1*, 032156.

[111] Colera, I.; Soria, E.; de Segovia, J.; Román, E.; González, R. Characterization of the MgO(100) surface by electron stimulated desorption. *Vacuum* **1997**, *48*, 647–649.

[112] Urban, R. Electron tunneling and spin dynamics and transport in crystalline magnetic multilayers. Ph.D. thesis, Simon Fraser University, Burnaby, B.C., Canada, 2003.

[113] Han, W.; Zhou, Y.; Wang, Y.; Li, Y.; Wong, J.; Pi, K.; Swartz, A.; McCreary, K.; Xiu, F.; Wang, K. L.; Zou, J.; Kawakami, R. Growth of single-crystalline, atomically smooth MgO films on Ge(001) by molecular beam epitaxy. *Journal of Crystal Growth* **2009**, *312*, 44–47.

[114] Jeon, K.-R.; Park, C.-Y.; Shin, S.-C. Epitaxial Growth of MgO and CoFe/MgO on Ge(001) Substrates by Molecular Beam Epitaxy. *Crystal Growth & Design* **2010**, *10*, 1346–1350.

[115] Tusche, C.; Meyerheim, H.; Jedrecy, N.; Renaud, G.; Kirschner, J. Growth sequence and interface formation in the Fe/MgO/Fe(001) tunnel junction analyzed by surface x-ray diffraction. *Physical Review B* **2006**, *74*, 195422.

[116] Nilius, N. Properties of oxide thin films and their adsorption behavior studied by scanning tunneling microscopy and conductance spectroscopy. *Surface Science Reports* **2009**, *64*, 595–659.

[117] Vassent, J. L.; Marty, A.; Gilles, B.; Chatillon, C. Thermodynamic analysis of molecular beam epitaxy of MgO(s) I. MgO vaporization by electron bombardment. *Journal of Crystal Growth* **2000**, *219*, 434–443.

[118] Rothberg, G. M.; Eisenstadt, M.; Kusch, P. Free Evaporation of Alkali Halide Crystals. *Journal of Chemical Physics* **1959**, *30*, 517.

[119] Eisenstadt, M.; Rothberg, G. M.; Kusch, P. Molecular Composition of Alkali Fluoride Vapors. *Journal of Chemical Physics* **1958**, *29*, 797.

[120] Vlaic, P. Calculated magnetic and transport properties of Fe/NaCl/Fe (001) magnetic tunnel junction. *Journal of Magnetism and Magnetic Materials* **2010**, *322*, 1438–1442.

[121] Nakazumi, M.; Yoshioka, D.; Yanagihara, H.; Kita, E.; Koyano, T. Fabrication of Magnetic Tunneling Junctions with NaCl Barriers. *Japanese Journal of Applied Physics* **2007**, *46*, 6618–6620.

[122] Sadewasser, S.; Lux-Steiner, M. Correct Height Measurement in Noncontact Atomic Force Microscopy. *Physical Review Letters* **2003**, *91*, 266101.

[123] Kittel, C. *Introduction to Solid State Physics*, 7th ed.; Wiley: New York, 1996; p 66.

[124] Finch, S. R. *Mathematical Constants*; Cambridge University Press: Cambridge, 2003; p 76.

[125] Chang, C.-Y.; Li, H.-D.; Tsay, S.-F.; Chang, S.-H.; Lin, D.-S. Atomic and Electronic Processes during the Formation of an Ionic NaCl Monolayer on a Covalent Si(100) Surface. *Journal of Physical Chemistry C* **2012**, *116*, 11526–11538.

[126] Olsson, F.; Persson, M. A density functional study of adsorption of sodium-chloride overlayers on a stepped and a flat copper surface. *Surface Science* **2003**, *540*, 172–184.

[127] Maier, S.; Pfeiffer, O.; Glatzel, T.; Meyer, E.; Filleter, T.; Bennewitz, R. Asymmetry in the reciprocal epitaxy of NaCl and KBr. *Physical Review B* **2007**, *75*, 1–7.

[128] Calloni, A.; Picone, A.; Brambilla, A.; Finazzi, M.; Duò, L.; Ciccacci, F. Effects of temperature on the oxygen aided Cr growth on Fe(001). *Surface Science* **2011**, *605*, 2092–2096.

[129] Dai, D. J. Induced infrared absorption of oxygen physisorbed on NaCl films. *Journal of Chemical Physics* **1996**, *104*, 6338.

[130] Blonski, P.; Kiejna, A.; Hafner, J. Theoretical study of oxygen adsorption at the Fe(110) and (100) surfaces. *Surface Science* **2005**, *590*, 88–100.

[131] Hino, S.; Lambert, R. M. Chlorine chemisorption and surface chloride formation on iron: adsorption/desorption and photoelectron spectroscopy. *Langmuir* **1986**, *2*, 147–150.

[132] Ke, Y.; Xia, K.; Guo, H. Oxygen-Vacancy-Induced Diffusive Scattering in Fe/MgO/Fe Magnetic Tunnel Junctions. *Physical Review Letters* **2010**, *105*, 236801.

[133] Mather, P.; Read, J.; Buhrman, R. Disorder, defects, and band gaps in ultrathin (001) MgO tunnel barrier layers. *Physical Review B* **2006**, *73*, 1–5.

[134] Woodside, M. T.; McEuen, P. L. Scanned Probe Imaging of Single-Electron Charge States in Nanotube Quantum Dots. *Science* **2002**, *296*, 1098–1101.

[135] Zhu, J.; Brink, M.; McEuen, P. L. Frequency Shift Imaging of Quantum Dots with Single-Electron Resolution. *Applied Physics Letters* **2005**, *87*, 242102.

[136] Stomp, R.; Miyahara, Y.; Schaer, S.; Sun, Q.; Guo, H.; Grutter, P.; Studenikin, S.; Poole, P.; Sachrajda, A. Detection of Single-Electron Charging in an Individual InAs Quantum Dot by Noncontact Atomic-Force Microscopy. *Physical Review Letters* **2005**, *94*, 056802.

[137] Cockins, L.; Miyahara, Y.; Bennett, S. D.; Clerk, A. A.; Grutter, P. Excited-State Spectroscopy on an Individual Quantum Dot Using Atomic Force Microscopy. *Nano Letters* **2012**, *12*, 709–713.

[138] Hattori, S.; Kano, S.; Azuma, Y.; Tanaka, D.; Sakamoto, M.; Teranishi, T.; Majima, Y. Coulomb Blockade Behaviors in Individual Au Nanoparticles as Observed Through Noncontact Atomic Force Spectroscopy at Room Temperature. *Nanotechnology* **2012**, *23*, 185704.

[139] Tekiel, A.; Topple, J.; Miyahara, Y.; Grütter, P. Layer-by-Layer Growth of Sodium Chloride Overlayers on an Fe(001)-p(1×1)O Surface. *Nanotechnology* **2012**, *23*, 505602.

[140] Barth, C.; Henry, C. R. High-Resolution Imaging of Gold Clusters on KBr(001) Surfaces Investigated by Dynamic Scanning Force Microscopy. *Nanotechnology* **2004**, *15*, 1264–1272.

[141] Pakarinen, O.; Barth, C.; Foster, A.; Nieminen, R.; Henry, C. High-Resolution Scanning Force Microscopy of Gold Nanoclusters on the KBr(001) Surface. *Physical Review B* **2006**, *73*, 235428.

[142] Barth, C.; Henry, C. R. Gold Nanoclusters on Alkali Halide Surfaces: Charging and Tunneling. *Applied Physics Letters* **2006**, *89*, 252119.

[143] Barth, C.; Pakarinen, O. H.; Foster, A. S.; Henry, C. R. Imaging Nanoclusters in the Constant Height Mode of the Dynamic SFM. *Nanotechnology* **2006**, *17*, S128–S136.

[144] Abe, M.; Sugimoto, Y.; Namikawa, T.; Morita, K.; Oyabu, N.; Morita, S. Drift-Compensated Data Acquisition Performed at Room Temperature with Frequency Modulation Atomic Force Microscopy. *Applied Physics Letters* **2007**, *90*, 203103.

[145] Clerk, A. *Simple model for damping from a quantum dot*; unpublished: McGill University, Montreal, 2009.

[146] Heyraud, J.; Métois, J. Establishment of the Equilibrium Shape of Metal Crystallites on a Foreign Substrate: Gold on Graphite. *Journal of Crystal Growth* **1980**, *50*, 571–574.

[147] Guerra, R.; Tartaglino, U.; Vanossi, A.; Tosatti, E. Ballistic Nanofriction. *Nature Materials* **2010**, *9*, 634–637.

[148] Lazzari, R.; Renaud, G.; Jupille, J.; Leroy, F. Self-Similarity During Growth of the $Au/TiO_2(110)$ Model Catalyst as Seen by the Scattering of X-Rays at Grazing-Angle Incidence. *Physical Review B* **2007**, *76*, 125412.

[149] Lebedev, N. N.; Skalskaya, I. P.; Uflyand, Y. S. *Worked Problems in Applied Mathematics*; Dover Publications: New York, 1979.

[150] Ohgi, T.; Fujita, D. Consistent Size Dependency of Core-Level Binding Energy Shifts and Single-Electron Tunneling Effects in Supported Gold Nanoclusters. *Physical Review B* **2002**, *66*, 115410.

[151] Mativetsky, J. M.; Burke, S. A.; Fostner, S.; Grutter, P. Nanoscale Pits as Templates for Building a Molecular Device. *Small* **2007**, *3*, 818–821.

[152] Topple, J. M.; Burke, S. A.; Ji, W.; Fostner, S.; Tekiel, A.; Grutter, P. Tailoring the Morphology and Dewetting of an Organic Thin Film. *Journal of Physical Chemistry C* **2011**, *115*, 217–224.

[153] Gardner, J.; Bennett, S. D.; Clerk, A. A. Mechanically Probing Coherent Tunneling in a Double Quantum Dot. *Physical Review B* **2011**, *84*, 205316.

[154] Daniel, M.-C.; Astruc, D. Gold Nanoparticles: Assembly, Supramolecular Chemistry, Quantum-Size-Related Properties, and Applications toward Biology, Catalysis, and Nanotechnology. *Chemical Reviews* **2004**, *104*, 293–346.

[155] Choudhary, T.; Goodman, D. Catalytically Active Gold: The Role of Cluster Morphology. *Applied Catalysis A* **2005**, *291*, 32–36.

[156] Lopez-Acevedo, O.; Kacprzak, K. A.; Akola, J.; Häkkinen, H. Quantum Size Effects in Ambient CO Oxidation Catalysed by Ligand-Protected Gold Clusters. *Nature Chemistry* **2010**, *2*, 329–334.

[157] Karacuban, H.; Koch, S.; Fendrich, M.; Wagner, T.; Möller, R. PTCDA on Cu(111) partially covered with NaCl. *Nanotechnology* **2011**, *22*, 295305.

[158] Hosaka, S.; Koyanagi, H. Field evaporation of metal atoms onto insulator/conducting substrate using atomic force microscope. *Japanese Journal of Applied Physics* **1994**, *33*, 1358–1361.

[159] Pumarol, M. E.; Miyahara, Y.; Gagnon, R.; Grütter, P. Controlled deposition of gold nanodots using non-contact atomic force microscopy. *Nanotechnology* **2005**, *16*, 1083–1088.

[160] Fostner, S.; Tekiel, A.; Topple, J. M.; Miyahara, Y.; Grütter, P. Field deposition from metallic tips onto insulating substrates. *Nanotechnology* **2011**, *22*, 465301.

[161] Gingery, D.; Bühlmann, P. Single-step electrochemical method for producing very sharp Au scanning tunneling microscopy tips. *The Review of Scientific Instruments* **2007**, *78*, 113703.

[162] Fostner, S.; Burke, S. A.; Topple, J.; Mativetsky, J. M.; Beerens, J.; Grutter, P. Silicon nanostencils with integrated support structures. *Microelectronic Engineering* **2010**, *87*, 652–657.

[163] Waser, R., Ed. *Nanoelectronics and Information Technology*, 3rd ed.; Wiley-VCH: Berlin, 2012.

[164] Fostner, S. Ultra high vacuum fabrication of metallic contacts for molecular devices on an insulating surface. Ph.D. thesis, McGill University, Montreal, QC, Canada, 2010.